NON-CARTESIAN MAGNETIC RESONANCE IMAGING STRATEGIES: IMPROVEMENTS IN ACCELERATED CARDIAC MAGNETIC RESONANCE IMAGING AND TECHNICAL CONSIDERATIONS

by
Ozan Sayin

A dissertation submitted to Johns Hopkins University in conformity with the requirements for the degree of Doctor of Philosophy

Baltimore, Maryland
November, 2017

ABSTRACT

Magnetic Resonance Imaging (MRI) is a medical imaging modality that is essential for the imaging of heart because of its unparalleled soft tissue contrast and lack of ionizing radiation. However, the dynamic nature of the heart, together with the motion introduced by respiration, make it a challenging task to generate MRI images without motion-induced artifacts. Traditional approaches deal with physiological motion by acquiring the necessary information to create an image in segments over many heartbeats via electrocardiogram (ECG) gating. Nevertheless, advancements in MRI scanner hardware and image reconstruction techniques, over the past decade, have led to the emergence of real-time MRI acquisitions of cardiac scans where the MRI signal used in reconstructing one image is collected in a single shot. The temporal window during which data is collected from the MRI scanner is extremely short (<50ms) for adequately imaging the heart, and such "real-time" accelerated imaging entails the recovery of image information from severely undersampled data.

Existing techniques that address the problem of reconstructing images from highly undersampled MRI data come with costs, either in the form of additional MRI scans a priori or aggressive assumptions on the underlying spatiotemporal properties of the object being imaged. In this work, a thorough investigation of one such method that requires a lengthy calibration pre-scan is performed, and novel techniques, which leverages the insights gained from this investigation and incorporates other unprecedented ways of tackling the problem, that facilitate the real-time monitoring of cardiac function, without the inconvenience of a separate calibration scan and assumptions on the statistical properties of the heart's motion, were developed and evaluated in animal and human subject studies, producing images with comparable quality to existing cardiac MRI techniques. The developed techniques have significant potential of improving the patient's experience in the clinic, while preserving diagnostic power. They also have the potential to enhance other real-time MRI scenarios such as MRI-guided procedures where a priori calibration scans are infeasible.

Advisor and First Reader:

Daniel A. Herzka, PhD

Assistant Professor, Biomedical Engineering

Johns Hopkins University School of Medicine

Second Reader:

Aravindan Kolandaivelu, MD

Assistant Professor, Cardiology

Johns Hopkins University School of Medicine

ACKNOWLEDGEMENTS

I would like to thank Professor Daniel Herzka for mentoring me throughout my doctoral studies. I am especially grateful for his effort, early on, in introducing me to the field of magnetic resonance imaging that entails solid understanding in various disciplines. He has constantly pushed me to grow myself both intellectually and emotionally, always being supportive and reassuring his confidence in me along the way. I learned a lot from my personal interactions with Prof. Herzka, yet, he has also granted me the intellectual independence to learn on my own, which I am very grateful for. I would also like to thank Professor Elliot McVeigh for his assistance and valuable guidance in my research directions. The exposure to his vast, pioneering experience and knowledge in the field of magnetic resonance imaging has been a fantastic experience.

I am grateful for my time at such a stupendous institution as Johns Hopkins. One of the uncountably many remarkable experiences I had at Hopkins was working with Aravindan Kolandaivelu, M.D. without a doubt. I learned a lot from Dr. Kolandaivelu, from cardiac MRI, to electrophysiology procedures, but, more importantly, he has set a great example to me by his curiosity and perseverant pursuit in his research to better the lives of patients, while doing it all on top of his clinician duties. It was further astonishing to witness his aptitude in MRI physics and computer programming, which he is better at than many engineers I have come across. I would also like to thank my former lab mates, Drs. Liheng Guo, Amir Pourmorteza, Farhad Pashakhanloo, Tri Ngo for a very pleasant environment in which many great ideas were exchanged. I feel blessed to have spent my graduate school years around them, as I know that it would not have been so great an experience if not for their kindness and support. I also thank Dr. Haris Saybasili for providing valuable collaboration in my research projects.

I have grown tremendously as a person in Baltimore, during when I met and built strong relationships with many people. I now call them my friends and am extremely grateful for their

company during this journey. Graduate school is often a stressful, demanding experience, and therefore, I would like to thank, in no particular order, Recep Özgün, Mustafa Köten, Arcan Ertürk, Joanna Lobl, Tutkun Şen, Okay Kayaoğlu, Yakup Günbatar, Ali Uneri, John Issa, Emre Oğuzöncül, Bora Erdemli, Burak Tekeş, Eva Cunha, Can Ceritoglu, Patrick Conlon and Vlada Usherenko for their joyful company and true friendship. I would also like to thank my best friends from college, Uğur Olgun, Muratcan Alkan, Kutay Pınarcı and Ozgür Şahin – even though we did not see one another for years, their friendship has proven unwavering.

Finally, I am grateful to my parents, Gül and Ali, for their unconditional love, support and sacrifice. Ever since I was a baby, they have dedicated their lives to my education, and this journey would have never happened without them.

TABLE OF CONTENTS

LIST OF FIGURES

LIST OF TABLES

1 INTRODUCTION

1.1 Magnetic Resonance Imaging

Magnetic Resonance Imaging (MRI) is an established medical imaging modality that serves almost all branches of medicine, from neuroscience to cardiology to orthopedics. It is often a favorable choice due to its superior soft-tissue contrast, flexibility of the imaging plane or volume, high spatial resolution and the lack of ionizing radiation. As it constitutes a crucial component of medical imaging, an extensive amount of research has been conducted for advancing MRI technologies, spanning a wide range of research areas such as data acquisition, image reconstruction, hardware engineering and clinical applications. Since the work in this dissertation lies within the scope of data acquisition and image reconstruction techniques, background in signal acquisition and image formation is presented in this chapter.

1.1.1 Signal and Contrast Formation

The hydrogen atom (^{1}H) is the primary source of signal in MRI due to its abundance in biological specimens and it possesses a spin magnetic moment as any other atom with an odd number of nuclei. When placed in a static magnetic field $\overrightarrow{B_0}$, the spin moments from an ensemble of hydrogen nuclei collectively align with $\overrightarrow{B_0}$, yielding a net magnetization of $\overrightarrow{M_0}$. A radiofrequency (RF) pulse, circularly polarized around the axis of the static magnetic field (the z-axis), is then utilized to excite the spin moments, causing the net magnetization $\overrightarrow{M_0}$ to tip away from the z-axis at an angle α (*tip angle* or *flip angle*) and precesses about the z-axis. The precession frequency is equal to the frequency of the RF pulse, which is denoted as the *Larmor Frequency:*

$$w_0 = - \gamma B_0, \qquad 1\text{-}1$$

where γ is the gyromagnetic ratio (radians/second/tesla), a unique physical constant for every atom. For ^{1}H, $\gamma/2\pi$ is equal to 42.58 MHz/Tesla, resulting in a Larmor Frequency of 63.87 MHz for a typical main MRI magnetic field of 1.5T. When the net magnetization $\overrightarrow{M_0}$ is tipped from the z-axis, it has a component M_{xy} perpendicular to the z-axis called the *transverse magnetization.* This component, in fact, is the magnetization that rotates in the transverse plane about the z-axis at the Larmor frequency, and, by Faraday's law of induction, it can generate an electromagnetic signal, proportional in magnitude, in an induction receiver coil. As a result, the MRI signal is the mapping of the magnetization $\overrightarrow{M_{xy}}(\vec{r})$, which arises from the hydrogen nuclei at a particular spatial location $\vec{r}$ (2D pixel or 3D voxel) within the imaged tissue.

As M_0 varies among tissue types, $M_{xy}(\vec{r})$ takes different values, and this results in discrepancies between the MRI signals acquired from different anatomical locations, yielding tissue contrast. Furthermore, following the RF excitation, the tipped magnetization starts to recover towards the initial $\overrightarrow{M_0}$, with M_z (magnetization along the z-axis) and M_{xy} decaying exponentially with time constants T_1 and T_2, respectively. As the values of T_1 and T_2 vary between different tissue types, tissue contrast can also be generated by manipulating the magnetization in a way to yield desired discrepancies in $M_{xy}(\vec{r})$ over tissues at the time of signal acquisition. Careful design of RF excitation pulses in conjunction with timing between these pulses and the signal sampling instants, robust control of tissue contrasts can be realized.

1.1.2 The k-Space and Image Formation

Denoting the magnetization of the underlying tissue of interest as $s(\vec{r})$, the measurement of the signal in the receiver coil directly under the main magnetic field $\overrightarrow{B_0}$ would result in the integrated sum of $s(\vec{r})$ over the entire 2D slice or 3D volume that is excited by the RF pulse. However, image formation entails the spatial localization of $s(\vec{r})$ since it is a function of space. In other words, the spatial coordinate of the magnetization needs to be encoded in the MRI signal that is captured in the receiver coil.

In order to explain how this spatial encoding works, let us express $\vec{s}(\vec{r})$ in phasor notation as $\vec{s}(\vec{r}) = s(\vec{r})\exp(i\phi(\vec{r}))$, where $\phi(\vec{r})$ is the rotational phase in a frame of reference that is rotating about the z-axis with frequency (in radians) equal to $w_0 = -\gamma B_0$. As a result, $\phi(\vec{r}) = 0$ for a magnetization that only experiences the main magnetic field, but this rotational phase can be controlled by superimposing a magnetic field on top of $\overrightarrow{B_0}$ in the same direction. If a field at strength ΔB is superimposed for T seconds, the magnetization will accrue a phase equal to:

$$\Delta\phi = -\gamma \Delta B T \tag{1-2}$$

Employing a ΔB that varies as a linear function of space, spatial location can be encoded in the accrued phase as below (assuming the variation is in 1D along the x-axis):

$$\Delta\phi(x) = -\gamma x G_x T \tag{1-3}$$

where G_x (tesla/meter) is the x-gradient of the magnetic field such that $\Delta B = G_x x$. In practice, the gradients are generated by physical magnetic gradient coils and are functions of time. The phase accrual can then be expressed as:

$$\Delta\phi(x,t) = -\gamma x \int_0^t G_x(\tau)d\tau \tag{1-4}$$

Accordingly, the magnetization becomes:

$$\vec{s}(x,t) = \vec{s}(x)\exp\left(-i\gamma x \int_0^t G_x(\tau)d\tau\right) \tag{1-5}$$

The receiver coil measures the signal of such magnetization from a range of spatial locations, thus, the signal expression, $S(t)$, can be obtained by integrating Equation 1-5 over the range of x values where the coil is sensitive to the magnetization (assuming uniform coil sensitivity) as below:

$$S(t) = \int \vec{s}(x)\exp\left(-i\gamma x \int_0^t G_x(\tau)d\tau\right)dx \tag{1-6}$$

Defining the quantity:

$$k_x = \frac{\gamma}{2\pi}\int_0^t G_x(\tau)d\tau$$

1-7

Equation 1-6 can be rewritten as:

$$S(k_x(t)) = \int \vec{s}(x)\exp\left(-i2\pi x k_x\right)dx$$

1-8

which is a complex-valued Fourier transform from the physical domain x to the spatial frequency domain k_x. This spatial frequency domain is also known as the *k-space.*

As can be deduced from Equation 1-8, the MRI signal is the measurement of the spatial frequency information content of the underlying imaged object (tissue), where the spatial frequency value is given by the position in the k-space at the time of signal sampling. Samples at high $k_x$values represent the component of the image that contains significant oscillations in the physical domain x, thus, fine details, whereas samples near the center of the k-space correspond to smooth changes in the image. When enough measurements are performed in a way to yield adequate sampling of the k-space, the image can be reconstructed via an inverse Fourier transform.

This formalism can be extended to 2D and 3D without loss of generality by considering k-space as a vector space such that $\vec{k} = \begin{bmatrix} k_x \\ k_y \\ k_z \end{bmatrix}$. In this case, Equation 1-8 can be generalized to a 2D or a 3D Fourier transform, where the imaged slice or the volume can be reconstructed via an inverse 2D or 3D Fourier transform, respectively.

1.1.3 Sampling in k-Space

Signal in MRI is discrete in nature because data collected by receiver coils needs to be sampled at finite number of measurements and digitized in the scanner's computer. In other words, the k-space is "sampled" in a finite (band-limited) manner and images are reconstructed from these samples. To be more specific, any activity in the magnetic gradient coils translate to a change in k-space, as can be deduced by Equation 1-7, and the most straightforward method to sample the k-space is by applying field gradients from one or more of the gradient coils at constant levels for a certain time duration, resulting in a k-space path in the form of a straight line that is traversed with a constant velocity. While the k-space is traversed along this line, data can be collected at equal time intervals and such a line in k-space is known as a "readout". Conventional 2D MRI is performed via the acquisition of successive readouts where each readout is sampled on a unique and constant value of k_y [1], sampling only along the k_x direction (i.e. only applying the x-gradient G_x). N_y readouts are acquired, where the k_y values are incremented by a constant Δk_y between readouts, ranging from $(-N_y/2)\Delta k_y$ to $(N_y/2\ -1)\Delta k_y.$ Similarly, during the time of a readout (TR), signal is sampled at N_x equidistant k-space points, starting from $(-N_x/2)\Delta k_x$ and ending at $(N_x/2\ -1)\Delta k_x$ where Δk_x is the distance between successive samples, resulting in a rectilinear (Cartesian) grid of k-space samples.

Such finite and discrete sampling in the spatial frequency domain leads to a band-limited and periodic signal in the image domain [2]. Sampling the continuous 2D spatial frequency space $S(k_x, k_y)$ at discrete points $\mathrm{S}[u, v] = S(u\Delta k_x, v\Delta k_y)$, where u and v are integers in $[-N_x/2, N_x/2\ -1)$ and $[-N_y/2, N_y/2\ -1)$ respectively, the continuous Fourier Transform in Equation 1-8 can be expressed as a Discrete Fourier Transform:

$$\mathrm{S}[u, v] = \sum_m \sum_n s[m, n] \exp\left(-\mathrm{j}2\pi\left[m\Delta x\ u\Delta k_x + n\Delta y\ v\Delta k_y\right]\right) \tag{1-9}$$

resulting in the recovery of the continuous 2D image at discrete x-y coordinates as $\mathrm{s}[u, v] = \mathrm{s}(m\varDelta x, n\varDelta y)$. The values $\varDelta x$ and $\varDelta y$ designates the size of an image pixel in physical space, or otherwise referred to as the in-plane *resolution* in either direction. The image signal is retained only at a finite extent, known as the *Field of View* (FoV), in the ranges $[-FoV_x/2, FoV_x/2]$ and $[-FoV_y/2, FoV_y/2]$, where $FOV_x = N_x\varDelta x$ and $FOV_y = N_y\varDelta y$. Typical 2D Cartesian sampling utilizes matrix sizes of N_x(=N_y) =128 or N_x=N_y=256 and the reconstruction of an image from k-space samples is performed via a Fast Fourier Transform (FFT) [3].

1.1.4 Radial Imaging

In addition to the conventional Cartesian k-space trajectory, another popular choice for sampling the spatial frequency information is radial k-space sampling [4]. In radial MRI, k-space is still sampled line by line in successive readouts similar to Cartesian sampling, but each straight line is a radial "spoke" that goes through the center of k-space. The azimuthal angles of the readout lines, also referred to as "profiles" in radial MRI, are equally spaced in the range [0, π). Therefore, the signal in k-space is sampled in polar coordinates as follows:

$$\mathrm{S}_{\mathrm{radial}}[r, p] = S(r\varDelta k_r \cos(p\varDelta\varTheta), r\varDelta k_r \sin(p\varDelta\varTheta)) \qquad 1\text{-}10$$

where $\varDelta k_r$is the distance between samples in a readout, $\varDelta\varTheta$ is the azimuthal angle increment between each profile, and r and p are integer indices on the radial-polar angle grid in the ranges [-N_r/2, N_r/2 -1) and [0, P-1] respectively, with $N_r$denoting the number of samples in one readout and P = π/ΔΘ denoting the number of total radial profiles.

Sampling the k-space in a polar coordinate in this manner, it is not possible to reconstruct images directly via a FFT as in Cartesian MRI. One approach for reconstructing images from polar-sampled data is filtered back projection [5], which was developed for fan-beam CT and was also the method of choice in early MRI reconstructions. A more popular and widely accepted strategy, however, is mapping the k-space samples on the polar grid to points on the standard Cartesian grid and then performing the FFT to generate images. The mapping is performed by interpolating the k-space samples with a convolution operation and is generally referred to as *convolution gridding* [6–8], where the convolution functions typically use a cosine-windowed sinc or a Kaiser-Bessel kernel with a small width for computational considerations. Additionally, a method that reconstructs images directly from data sampled on a non-Cartesian grid using a non-uniform FFT was recently proposed and gained popularity [9].

Radial k-space coverage has numerous advantages. Undersampling in the azimuthal direction results in less coherent artifacts (streaks) compared to artifacts due to undersampling in Cartesian MRI (e.g. folding, ghosting) [10,11]. The center of k-space, which contains a large fraction of the overall signal power, is acquired in every readout, enabling reconstructions from fewer readouts. This makes radial imaging very suitable for dynamic MRI applications that require shorter temporal windows where data is to be collected. Moreover, based on the central slice theorem [12], every radial readout in k-space is equivalent to the projection of the image onto a line with the same angular orientation in the physical space, when converted back to a 1D line in image space via an inverse Fourier transform. Therefore, motion information is acquired very frequently in radial MRI, enabling the navigation of motion, a valuable component in certain MRI applications [13–15].

1.2 Cardiac MRI

1.2.1 Overview of Clinical Applications

MRI is a favorable imaging modality for imaging the heart, because its superior soft-tissue contrast enhances the joint visualization of myocardium, blood and fat better than other imaging tools, and therefore, cardiac MRI (CMR) has utility in various clinical applications. The imaging of cardiac morphology and function are typically performed via *cine* MRI [16], where a series of image frames displaying the motion of the heart throughout the entire cardiac cycle are generated. Similarly, *phase-contrast* imaging realizes the imaging of blood flow in the heart by encoding velocity in the phase of the complex-valued MRI images [17]. MRI is also effective in the characterization of the cardiac myocytes in various ways. Iron deposition, an early indicator for risk of infarction, which is reversible, can be imaged with T_2 mapping [18,19] whereas ischemic myocardium can be determined via *perfusion* MRI [20]. Finally, viability (infarcted tissue) imaging is performed by *delayed-enhancement* MRI [21,22]. CMR is also valuable in angiography due and can be preferred over CT in children and young adults where risk of cancer due to ionizing radiation is considerable [23].

Nonetheless, the dynamic nature of the heart makes it a challenging organ to image. Respiratory and cardiac motion both needs to be compensated for to avoid image artifacts that can appear in the form of blurring, ghosting etc. In *cine* imaging, cardiac motion is typically addressed by electrocardiogram (ECG) gating whereas respiratory motion is compensated by either scanning the patient while the breath is held or by using a respiratory belt to track the movement. However, more efficient CMR techniques that address cardio-respiratory movement have been developed and are discussed in the subsequent sections.

1.2.2 Segmented Gated CINE Imaging

The temporal resolution (bandwidth) of a cardiac image frame is generally required to be less than 50ms to be considered diagnostic quality [24]. Employing a fast *balanced steady-state free-precession* (bSSFP) [25–28] MRI pulse sequence with a readout duration of ≈3ms, the number of readouts in a single shot of imaging are limited to no greater than 16, which is insufficient to sample the k-space. In conventional segmented cine imaging, this is overcome by sampling only a fraction (segment) of the k-space at a time. Typically, the 2D Cartesian k-space trajectory is adopted and only 8-16 adjacent k-space readouts that constitute a k-space segment are acquired, conforming to the temporal resolution criterion, repeatedly for at least one complete R-R cycle [29]. Each remaining segment of the k-space is then acquired in the same fashion over subsequent cardiac cycles. As an example, for a segment of 12 readouts and a target k-space grid of 192x192, there are 16 k-space segments and this requires scanning during at least 16 cardiac cycles.

In this scheme, the sampling of each k-space segment starts with an R wave, therefore, the cardiac motion needs to be traced. The electrocardiogram (ECG), usually using 3 leads on the subject's chest, is utilized to this end to trigger imaging upon a detected R wave. Although the use of ECG for cardiac gating is widespread in the clinic, it is regardless a nuisance that impairs the clinical experience from the patient's and the MR technologist's perspective. Additionally, the ECG signal can be distorted due to a number of factors including fast-switching magnetic field gradients [30,31] and blood flow [32,33]. Alternatively, a body of work has been developed to estimate the cardiac motion directly from the MRI signal [34–38].

As segmented cine imaging requires the scan to last over multiple (>10) R-R cycles, breath holding is not always a comfortable option, especially for certain patients. Moreover, breath holding can elevate the resting heart rate [39], further complicating the objective of generating an image series sufficient number of cardiac phases. As an alternative, conventional respiratory gating is performed via a respiratory belt [40,41], but this coarse proxy for tracking respiratory movement can fail in many cases. Motion-compensated cine imaging [42–44] that eliminates such need of external respiratory gating has been an active field of research though it has not yet been widely accepted in the clinic.

1.2.3 Real-time Cardiac Imaging

Though segmented cine imaging produces images at high spatial resolution with superior diagnostic quality for the imaging of cardiac function, it depends on the regularity of the cardiac motion, and thus, is suboptimal for imaging of patients with cardiac arrhythmias. Advancements in scanner hardware that accommodate large arrays with multiple receiver coils [45,46] and reconstruction techniques that permit image formation from vastly undersampled k-spaces have enabled the real-time imaging of the heart where images are generated in a single shot from data acquired within 50ms [47,48]. Single-shot imaging of the heart with such temporal resolution eliminates the need to compensate for cardio-respiratory motion, enabling ECG-free imaging of the cardiac motion under free breathing.

Over the past decade, there has been an extensive amount of research conducted for the objective of accelerating MRI to realize real-time cardiac imaging. The phenomena that led to such advancements can be summarized under two main categories: parallel imaging [49–54] and sparse MRI [55,56]. The next chapter explains these concepts in detail, as sound understanding of the fundamentals of accelerated MRI is critical to apprehend the work in this dissertation.

1.3 Accelerated Imaging for Cardiac MRI

1.3.1 Non-Cartesian Parallel Imaging

Parallel imaging (PI) is the phenomenon in MRI where signal is captured in multiple receiver coils, which enables spatial undersampling, thanks to the intrinsic correlations between the sensitivity profiles of these individual receiver coils. Conventional PI in 2D Cartesian MRI is performed by sampling only 1 out of R consecutive phase encoding lines of k-space and utilizing one of the two common PI reconstruction methods to remove the aliasing artifact caused by the R-fold reduced FoV, where R is known as the acceleration factor. Of these two methods, *Sensitivity Encoding* (SENSE) [51] is the reconstruction method that utilizes explicit information of the coil sensitivities to unwrap the aliased image directly on the image domain. On the other hand, *Generalized Autocalibrating Partially Parallel Acquisitions* (GRAPPA) [52] reconstructs artifact-free images by first estimating the missing spatial harmonics on k-space using a fully-sampled central region of k-space as auto-calibration signal, followed by the regular FFT. It has been shown that image reconstruction via either method suffers for acceleration rates greater than 4, which renders parallel imaging with standard Cartesian sampling generally insufficient for real-time cardiac MRI, since, for the evaluation of cardiac function, the acceleration factor generally needs to be at a minimum of 8 in order to generate images of the heart with the desired temporal bandwidth < 50ms at adequate in-plane resolution (i.e. $\approx 2.0\text{x}2.0\text{mm}^2$). Such level of acceleration ($R\approx 8$) using Cartesian k-space trajectories have been reported by extensions of these methods that employ further undersampling jointly in k-space and in time (k-t) [57,58], exploiting correlations of cardiac MRI data in both the spatial frequency and temporal domains, yet, image quality has been sub optimal due to amplified artifacts and noise.

On the contrary, undersampling using non-Cartesian k-space trajectories, two common schemes of which are radial [4,59] or spiral [60–62] k-space sampling, lead to less coherent, more tolerable image artifacts compared to images reconstructed with the same level of undersampling using Cartesian k-space sampling. As an example, 3-fold undersampling in the azimuthal dimension of a radial trajectory can generate images at acceptable quality, with tolerable streaking artifacts, without any post-processing steps [11,63,64]. Additionally, non-Cartesian k-space trajectories are more suitable for parallel imaging because undersampling occurs in both in-plane dimensions, instead of only undersampling along the phase encoding dimension as in Cartesian sampling, which leads to a more efficient use of the correlations among the receiver coil sensitivities. Most non-Cartesian trajectories oversample the SNR-rich center of k-space even under aggressive undersampling, and such efficient sampling of the k-space leads to lesser noise enhancement than that of undersampling in case of the standard 2D Cartesian imaging. Moreover, motion artifacts are reduced under non-Cartesian sampling, which is highly advantageous for cardiac MRI [59,65].

Although several different methods have been proposed to achieve high factors of acceleration with non-Cartesian k-space coverage, three representative techniques that span the range of such methods stand out: *Conjugate-Gradient SENSE* (CG-SENSE) [66], a direct extension of standard Cartesian SENSE that employs an iterative solution, non-Cartesian GRAPPA, extensions of the standard GRAPPA technique to radial [67,68] and spiral trajectories [69,70], and *Iterative Self-Consistent Parallel Imaging Reconstruction* (SPIRIT) [71], an iterative reconstruction method that enforces consistency in both the calibration and the reconstructed data.

1.3.1.1 CG-SENSE

CG-SENSE is an iterative implementation of the SENSE parallel imaging method using the conjugate gradient (CG) algorithm [72]. The SENSE reconstruction method unfolds the aliasing artifacts caused by undersampling the spatial frequency domain by utilizing the explicit information of the coil sensitivity maps. The following system of equations lay out the math of the technique.

$$Ev = m \qquad \text{1-11}$$

$$E_{jp} = \exp\left(ik_K r_p\right)C_l\left(r_p\right) \qquad \text{1-12}$$

where m is the k-space measurements vector of size $n_c n_k$x1, v is the vector of the object to be reconstructed (size N^2x1) and E is the encoding matrix of size $n_c n_k$xN^2 that transform an image to k-space by combining the coil sensitivities with the Fourier encoding into k-space. The constants n_c, n_k and N denote the number of receiver coils, the number of acquired k-space samples and the matrix size of the image. Equation 1-12 describes the construction of the encoding matrix E (i.e. the value in its j-th row and p-th column), where $C_l\left(r_p\right)$ denotes the sensitivity of the receiver coil l at the image pixel r_p ($1 \leq p \leq N^2$) and k_K is the location of the κ-th k-space sample ($1 \leq K \leq n_k$). As there are no restrictions on k_K, SENSE can be directly extended to non-Cartesian trajectories.

The reconstruction of the image v can then be performed as follows:

$$v = Fm \qquad \text{1-13}$$

$$F = (E^H E)^{-1} E^H \qquad \text{1-14}$$

where F is the Moore-Penrose pseudo-inverse of the encoding matrix E, ignoring the noise whitening terms. E^H stands for the Hermitian transpose of E. In the setting of non-Cartesian sampling, the standard SENSE reconstruction that employs the direct inversion of the encoding matrix is infeasible because the Fourier terms vary across two dimensions, unlike Cartesian imaging where only the spatial frequency basis functions along the phase encoding dimension needs to be included, and thus, the size of E is too large. To the end of finding an efficient solution to Equation 1-13 to reconstruction artifact-free images, the iterative optimization algorithm that converges rapidly, based on a conjugate-gradient update rule has been adopted. In addition, pre-conditioning terms that incorporate density compensation (for k-space locations) and intensity compensation, correcting for the sum-of-squares weighting due to variations in coil sensitivities, are introduced to the linear system of equations in Equation 1-13 and Equation 1-14, resulting in the following equation:

$$(IE^{H}DEI)(I^{-1}v) = IE^{H}Dm \qquad 1\text{-}15$$

where D is a diagonal matrix containing the values of the density compensation function and I is a diagonal matrix that contains the inverse square root of the coil weightings, calculated from the sensitivity maps. With this linear system at its core, the CG-SENSE is implemented in an iterative fashion (Figure 1.1) as follows:

i. The right hand side of Equation 1-15 is computed, generating an estimate of the reconstructed image. Gridding the k-space data onto a Cartesian grid is applied before the application of the inverse FFT to image domain (as part of E^{H})

ii. The result of is compared to the current image estimate and via the CG algorithm, a residuum vector is computed. In the first iteration, the current estimate is the initial estimate, typically chosen as the direct reconstruction of the undersampled data.

iii. An updated estimate of $I^{-1}v$ is calculated using the residuum vector and the encoding steps, including the application of intensity correction (I), multiplication by the coil sensitivity profiles, the FFT to Cartesian k-space and convolving with the gridding kernel, are performed. At this point, the original acquired k-space data is inserted back to the k-space for data consistency.

iv. Steps i-iii are repeated till the residuum power is below a pre-determined threshold.

v. When the stopping criterion at step iv. is reached, intensity correction is applied to yield the resulting image.

CG-SENSE has been a popular choice in accelerated MRI, having been successfully applied in many clinical applications, including cardiac MRI [73,74]. The flexibility in the choice of the k-space trajectory for acquisition makes it an appealing technique. Due to the iterative nature of the algorithm, the speed of image reconstruction can be burdensome, depending on the choice of the stopping criterion, however, a GPU-based open-source implementation, known as the Gadgetron, has realized the utility of the technique for real-time image display [75]. The main drawback of the CG-SENSE method is the requirement of the explicit coil sensitivity information because accurate sensitivity map estimation is a challenging task, especially in settings where patient movement may occur.

1.3.1.2 Radial GRAPPA

As CG-SENSE is en extension of the standard SENSE method, GRAPPA can also be adapted to non-Cartesian k-space trajectories. While the most common two k-space trajectories are radial and spiral sampling, since the original work presented in this dissertation builds upon the application of GRAPPA to radially sample k-space data, this section focuses on and explains in detail the radial GRAPPA technique.

To understand the radial GRAPPA method, first, the standard GRAPPA technique, designed for Cartesian k-space sampling, must be explained. For an acceleration factor of R, only every 1 out of R adjacent phase encoding (PE) lines is acquired, and the missing R-1 PE lines in between are estimated from the acquired ones in the neighborhood using GRAPPA [52]. This estimation of missing spatial frequencies is made possible by exploiting the spatial variations of the coil sensitivities in multi-channel receiver arrays that represent a convolution kernel in the Fourier domain applied during acquisition.

For GRAPPA reconstruction, the kernel weights that describes the contribution of the source points (acquired data) to the target point (missing data) needs to be defined. By convention, a B_y x B_x kernel (or block) selects the B_x closest k-space points in the readout direction from the B_y lines closest to the target missing point as source points. The target point is estimated as a weighted combination of $N_B = B_y \cdot B_x$ source points and this process is carried out for every missing k-point. GRAPPA reconstruction for images acquired with a reduction factor of R with a B_y x B_x kernel can be mathematically expressed as:

$$s_i(k_x, k_y n\Delta k_y) = \sum_{j=1}^{N_C} \sum_{b_{yi}=1}^{B_y-1} \sum_{b_{xi}=1}^{B_x-1} W_{i,j}(n, b_{xi}, b_{yi}) \,.\, s_j(k_x + b_x \cdot \Delta k_x, k_y + b_y \cdot \Delta k_y)$$

1-16

where k_x and k_y are k-space coordinates on the Cartesian sampling grid, and Δk_x and Δk_y are the distances in k-space between adjacent points. N_C is the number of coils, $s_i(k_x, k_y)$ is the target k-space point (k_x, k_y) in the i^{th} coil to be estimated, $s_j(k_x, k_y)$ is a source point from the j^{th} coil. The integer $n \epsilon [1,\ R-1]$ represents the index into subsampled PE lines between two closest sampled ones (indexed $n=0$ and $n=R$ *for* $B_y=2$). Indexes b_{xi} and b_{yi} are defined as$\{b_{xi} | b_{xi} \in \mathbb{Z}, 0 \le b_{xi} \le B_x - 1\}$ and $\{b_{yi} \middle| b_{yi} \in \mathbb{Z}, 0 \le b_{yi} \le B_y - 1\}$, respectively, and used with the 3D kernel weights array $W_{i,j}$ of size $(R-1)xB_xxB_y$), which is determined during calibration. $W_{i,j}$ links the target coil i and source coil j. b_x and b_y, defined as $\left\{b_x \middle| b_x = b_{xi} - \left\lfloor \frac{B_x}{2} \right\rfloor\right\}$ and $\left\{b_y \middle| b_y = R \cdot \left(b_{yi} - \left(\frac{B_y}{2} - 1\right)\right)\right\}$, map indexes into k-space coordinates, and assume even B_y and an odd B_x. A typical R=3 GRAPPA reconstruction with a N_B=3x2 kernel yields, $n \epsilon [1,2]$, $b_{xi} \epsilon [0,1,2]$, $b_{yi} \epsilon [0,1]$, $b_x \epsilon [-1,0,1]$, and $b_y \epsilon [0,3]$. A larger kernel with N_B=5x4 yields $n \epsilon [1,2]$ $b_{xi} \epsilon [0,1,2,3,4]$, $b_{yi} \epsilon [0,1,2,3]$, $b_x \epsilon [-2,-1,0,1,2]$, and $b_y \epsilon [-3,0,3,6]$.

For each target point (i.e a single n), the GRAPPA weights set for all coils W can be reorganized in a $(N_C . N_B)\ xN_C$ matrix, Then, Equation 1-16 can be rewritten in matrix form as:

$$\vec{S}_{trg} = \vec{S}_{src} \,.\, W \qquad 1\text{-}17$$

where $\vec{S}_{trg}$ is a $1xN_C$ row vector containing the target point for each coil, and $\vec{S}_{src}$ is a $1x(N_C . N_B)$ row vector containing the source points from each coil. W is determined by acquiring additional PE lines or projections such that multiple occurrences of the kernel with both source and target points known. A region of k-space, typically the center where SNR is highest, is fully sampled to yield this autocalibration signal (ACS). Collecting $\vec{S}_{trg}$ and $\vec{S}_{src}$ for each occurrence of the kernel in the ACS region into rows of the matrices $S_{trg,ACS}$ and $S_{src,ACS}$, yields a linear system:

$$W = \left(S_{src,ACS}\right)^{+} \cdot S_{trg,ACS} \qquad \text{1-18}$$

$$\left(S_{src,ACS}\right)^{+} = \left({S_{src,ACS}}^{H} S_{src,ACS}\right)^{-1} {S_{src,ACS}}^{H} \qquad \text{1-19}$$

where $\left(S_{src,ACS}\right)^{+}$ is the Moore-Penrose pseudo-inverse of $S_{src,ACS}$. The linear system in Equation 1-18 becomes exactly determined with $N_C . N_B$ kernel occurrences in the ACS region, though many more occurrences are needed to determine a stable weights set that can accurately represent the coil sensitivities without much influence from noise. This is relatively easy to achieve with Cartesian sampling, as the relative geometry of the source points with respect to the target point in k-space are identical throughout the entire undersampled k-space. In other words, the GRAPPA kernel is shift-invariant.

On the other hand, in the setting of radial k-space sampling where undersampling is carried out in the azimuthal dimension by sampling every 1 out of *R* consecutive projections, the GRAPPA kernel is no longer shift-invariant as the kernel geometries (i.e. relative positions of the source points to the target points) vary throughout the k-space. Therefore, there is only one "exact" kernel occurrence for a GRAPPA kernel even if the k-space is fully sampled. In the original formulation of radial GRAPPA [67], where the autocalibration data is provided by one fully sampled k-space frame prior to the scan that acquires successive undersampled frames, the process of obtaining kernel occurrences was achieved by dividing the k-space into small segments spanning a number of projections (N_{seg_proj}) and readout points (N_{seg_read}) with the size of a segment $N_{seg}= N_{seg,read}$ x $N_{seg,proj}$. Each segment is treated as a Cartesian k-space with the assumption that kernel geometries for missing points were similar enough within the segment, and thus, a single set of weights was necessary for the estimation of all target points within the segment.

Recently, an improved calibration scheme for radial GRAPPA that entails a calibration scan composed of multiple, not one, fully sampled k-space frames was proposed [68]. With this *through-time radial GRAPPA* calibration scheme, kernel occurrences for calibrating the GRAPPA weights are obtained from repetitions in time, where N_{frames_full} fully sampled frames provided multiple occurrences of calibration data with the exact GRAPPA kernel geometry for every target point. Including kernel occurrences only from temporal repetitions, without any in-k-space repetitions as in the original radial GRAPPA calibration, drastically increased the calibration accuracy resulting in much sharper images at the expense of increased calibration scan time.

Using the natural combination of this through-time calibration method with the original through-k-space approach (Figure 1.2), calibration scan duration was reduced, enhancing the clinical utility of radial GRAPPA. With a calibration scan using N_{frames_full}=80 frames with N_{seg}= 4x1 (minimal through-k-space calibration), 320 kernel occurrences can be obtained, and this is generally more than sufficient for stable calibration of GRAPPA weights when a typical 3x2 GRAPPA block is used. The rank of a matrix that would be constructed by stacking the k-space data from individual receiver coils as vectors would generally not exceed 16, thus, this linear system for weights calibration with 320 observations is usually sufficiently over-determined (320 >> 3x2x16). Realizing minimal kernel approximation using small GRAPPA segments and using calibration data with substantial over-determination for every missing k-space point, through-time radial GRAPPA has achieved robust image reconstruction from highly undersampled data ($R \geq$ 8). The technique has been validated in various clinical settings, including the evaluation of cardiac function [76–80].

1.3.1.3 SPIRIT

SPIRIT, like CG-SENSE, is a parallel imaging method works with arbitrary non-Cartesian trajectories. The reconstruction can be interchangeably carried out using a k-space or image-space domain approach. The SPIRIT technique relies on the two types of consistency measure: calibration consistency and data consistency. With the k-space approach, calibration consistency is expressed by the equation:

$$x = Gx \tag{1-20}$$

where x is a vector that contains the entire Cartesian k-space samples for all receiver coils, and G is the matrix of SPIRIT weights that relate the source points in a neighborhood to a target point, similar to the GRAPPA weights. G is shift-invariant, since it operates on a Cartesian grid, and an important distinction of Equation 1-20 from GRAPPA calibration is that it includes data that are generated during the iterative SPIRIT reconstruction on top of data that was originally acquired. For non-Cartesian trajectories, such as radial or spiral sampling, where the center of k-space is oversampled, the calibration data is typically obtained by interpolating the densely sampled k-space center onto a Cartesian grid.

The other component of SPIRIT, which distinguishes it from non-Cartesian GRAPPA and CG-SENSE, is the notion of data consistency that aims to ensure that the SPIRIT-reconstructed data is in accord with data that was originally acquired on the undersampled k-space. Data consistency is formulated as:

$$y = Dx \tag{1-21}$$

where D is a matrix that transforms the data on the Cartesian grid x, which is updated via SPIRIT, using inverse gridding to data on the undersampled trajectory. For data consistency, that operation should match the data on the undersampled non-Cartesian k-space that was originally acquired from the scanner (y).

Given both the constraints from calibration consistency and data consistency, the SPIRIT reconstruction can be formulated as an optimization problem:

$$\text{minimize } \|(G - I)x\|^2 \text{ such that } \|y - Dx\|^2 < \varepsilon \qquad \text{1-22}$$

This optimization problem can be solved using various methods such as conjugate-gradient descent[72] or projection over convex sets (POCS)[81]. One advantage of SPIRIT is that additional constraints can be included in Equation 1-22 to favor sparse solutions [82,83] and/or to mitigate noise amplification.

1.3.2 Sparsity-Based Techniques

After the initial introduction of *Compressed Sensing* [84] to the image reconstruction problem in MRI[55], reconstruction algorithms that incorporate a sparsity constraint have gained popularity. As the MRI data was demonstrated to be sparse on various domains, from the image domain itself [85–87], to other transform domains such as the Wavelet domain [55,88,89], or simply in the time domain in the case of dynamic imaging, more effective image reconstructions methods that exploited such information sparsity have been developed. Sparse solutions are typically realized by adding an L_1-norm term on whichever domain the sparsity is being enforced.

Cardiac MRI, especially the morphology and function imaging, lands itself well to this paradigm. The motion of the heart is confined to a relatively small region of the entire FoV, that the data is being collected from, with a small number of temporal frequency harmonics, rendering the information to be recovered fairly sparse in the *x-f* or *k-f* domains, where *x, k* and *f* refer to the image, k-space and temporal frequency domains, respectively. Similar to other MRI applications such as brain imaging, sparse recovery for accelerated cardiac imaging can be achieved via a pseudo-random k-space sampling strategy, associated with a more uniform PSF, and directly solving the an L_1-minimization problem in a spatiotemporal domain [90–92]. However, more effective utilization of compressed sensing has been demonstrated by combining it with other established parallel imaging techniques. The iterative nature of certain parallel imaging methods make it possible to include additional constraints in the optimization function - adding sparsity constraints in a spatiotemporal space to these methods have achieved highly robust reconstructions. A number of techniques that exploit this general idea with different variations have been reported [93–95], but for the sake of conciseness, a particular algorithm, known as *iterative Golden-angle Radial Sparse Parallel MRI* (iGRASP)[96], which has reported robust reconstructions in the setting of real-time free-breathing, is discussed in this section.

Effectively, iGRASP combines the concepts of parallel imaging, compressed sensing and golden-angle radial sampling where data are acquired on radial projections with the azimuthal angle continuously incremented by 111.25° per projection [97]. After generating temporal k-space frames by grouping an arbitrary number of successive projections into every frame, an iterative reconstruction is performed for the following optimization problem, in which sparsity in the temporal dimension is enforced in the form of a total variation (TV) constraint on the joint multi-coil image vector.

$$\hat{d} = argmin\{\|FSd - m\|_2^2 + \lambda\|Td\|_1\} \tag{1-23}$$

where d is the vector containing series of multi-coil images (in x-y-t), T is the total variation transform operator in time, m is the multi-coil measurement data in k-space, S is the coil sensitivity operator and F is the Fourier transform operator from k-space to image-space. Coil sensitivities (S) are generated from data containing a sufficient number of consecutive projections that yields streak-free low-temporal resolution images. Since no projection angle is repeated, the golden-angle radial trajectory is a suitable choice for estimating coil sensitivities, sampling the spatial frequency information in the most efficient manner. It also introduces temporal incoherence, which enhances the convergence of Equation 1-23 with the TV constraint term.

Although the exploitation of temporal sparsity in this manner yields high-quality images from highly undersampled k-space data, an inevitable assumption on the properties of the spatio-temporal information content of the underlying object (heart) is made. This can compromise the temporal fidelity of reconstructed image series because content with high-frequency oscillations, possible in patients with extreme arrhythmias, may be missed or suppressed. Additionally, the formulation of image reconstruction that utilizes the series of undersampled frames together in one batch cannot be used for the continuous real-time monitoring of the heart because the reconstruction of a frame is essentially using information from data acquired in subsequent frames.

1.4 Thesis Overview

Having been demonstrated to produce diagnostic-quality images from highly undersampled k-space data without the use of explicit assumptions about the sparseness of information, this work builds upon the non-Cartesian GRAPPA approach, developing novel image reconstruction methodologies for the application of real-time free-breathing cardiac imaging. Radial k-space sampling, which is the most popular choice of k-space trajectory besides the standard 2D Cartesian sampling, was adopted, and images of 2D slices in common cardiac slice orientations (views) were generated in all of the methodologies presented.

Chapter 2 describes the quantitative investigation of the through-time radial GRAPPA calibration method, proposing a metric that estimates the generalization performance of the technique. Limitations of the technique are revealed, in the setting of free breathing cardiac imaging, and actionable insights about the factors driving its performance are unearthed. Chapter 3 describes a novel self-calibration methodology for radial GRAPPA that eliminates the requirement for the additional calibration pre-scan. Real-time imaging with high spatio-temporal resolution is demonstrated with comparable image quality to standard radial GRAPPA reconstructions that utilize explicit calibration data acquired from a lengthy calibration scan preceding the actual accelerated imaging scan. Chapter 4 describes an extension of the self-calibration methodology proposed in Chapter 3 to undersampled radial data with acquired projections on arbitrary azimuthal angles, demonstrating the feasibility of accelerated real-time free breathing cardiac MRI using the golden-angle radial trajectory.

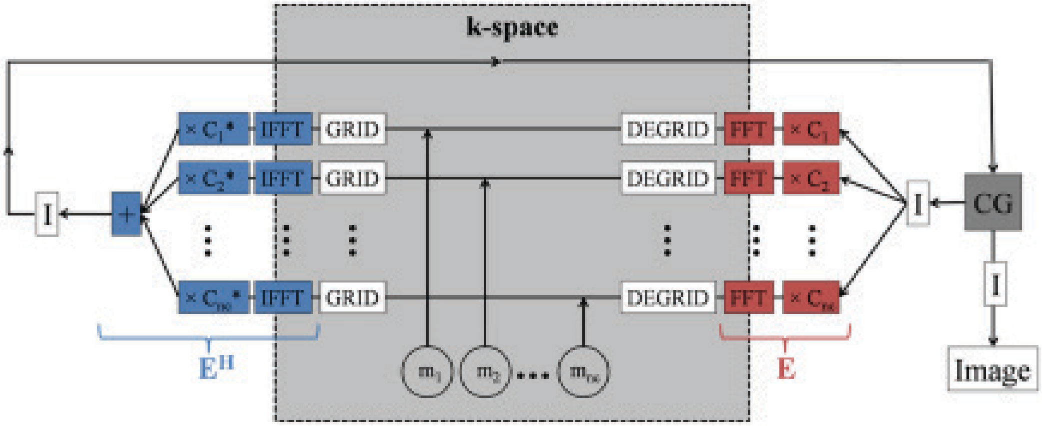

Figure 1.1. A summary of the CG SENSE algorithm, which reconstructs an image from undersampled non-Cartesian data. Undersampled, multi-channel *k*-space data (m_1, m_2,…,m_{nc}) are acquired and fed into the algorithm. These data are density compensated, gridded, the inverse Fourier transform calculated, and the multi-coil images are multiplied by the conjugate of the coil sensitivities. The multi-coil images are summed and intensity corrected to produce a single image, which is fed into the CG algorithm. The CG algorithm finds a new estimate for the reconstructed image. If the reconstruction has not converged, intensity correction is applied, the image is multiplied by the coil sensitivities, the Fourier transform is calculated, the data are degridded, the original data replaced, and the next iteration begins. This process continues until the reconstruction converges and a stopping criterion has been met. Once the stopping criteria are met, intensity correction is applied, and the result is an unaliased image. [Color figure can be viewed in the online issue, which is available at wileyonlinelibrary.com.] Reprinted, with permission, from Wright et al, *Non-Cartesian Parallel Imaging Reconstruction*, Journal of Magnetic Resonance Imaging, Vol. 40, Issue 5, pg. 1022-40 © 2014 Wiley Periodicals, Inc. [98]

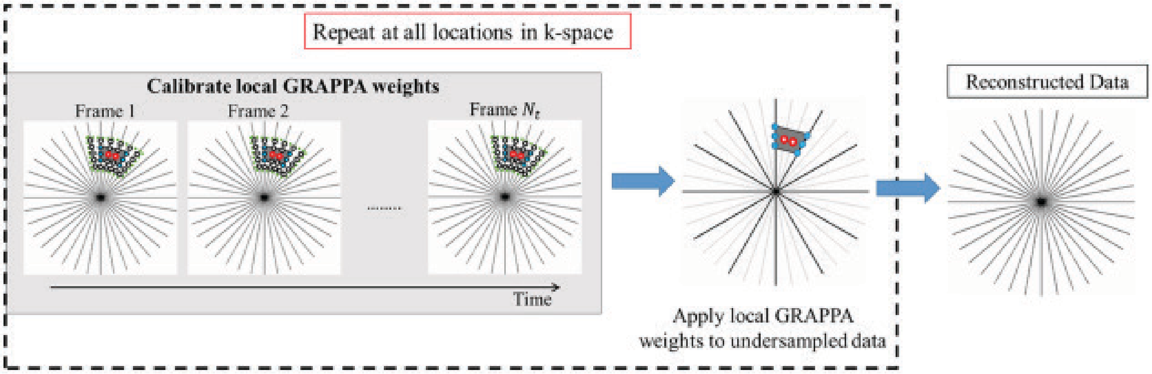

Figure 1.2. A schematic of the non-Cartesian GRAPPA reconstruction. First, one or more fully sampled datasets are acquired for calibration. The weights for each geometry can be determined using either *k*-space segmentation, through-time calibration, or a combination of the two. These weights are applied to the undersampled data at the appropriate location to reconstruct each target point. This process is repeated for each arrangement of source and target points to recover the fully sampled *k*-space. [Color figure can be viewed in the online issue, which is available at wileyonlinelibrary.com.] Reprinted, with permission, from Wright et al, *Non-Cartesian Parallel Imaging Reconstruction*, Journal of Magnetic Resonance Imaging, Vol. 40, Issue 5, pg. 1022-40 © 2014 Wiley Periodicals, Inc. [98]

2 QUANTITATIVE ANALYSIS OF WEIGHTS CALCULATION IN CARDIAC RADIAL GRAPPA

2.1 Introduction

For more than a decade, real-time magnetic resonance imaging (MRI) has been an active field of research and cardiac magnetic resonance (CMR) imaging is one area of clinical focus where such rapid imaging techniques have been explored extensively [42,47,48,99–101]. Due to cardiovascular dynamics, it is critical to create frames with relatively high temporal resolution (<50 ms/frame), and thus, conventional cine imaging segments data acquisition over multiple cardiac cycles, relying on ECG gating and breath-holding [29]. Image quality often depends on the regularity of the cardiac motion and deteriorates in the presence of cardiac arrhythmias. Real-time imaging removes the dependence on breath holds or gating as k-space is sampled in a single shot during a time interval short enough to yield the desired temporal resolution. However, the number of phase encoding lines or radial projections per image is constrained to fewer than 20, which has led to the heavy reliance of parallel imaging (PI) techniques [102,103]. To achieve adequate spatial resolution under these circumstances, acceleration factors > 4 are generally required, and because higher degrees of undersampling have been demonstrated with non-Cartesian k-space trajectories [11,63,104], non-Cartesian PI methods have been subject to interest in the MRI research community.

Though many non-Cartesian PI techniques have been proposed, extensions of the widely accepted PI algorithms, such as SENSE and GRAPPA, have gained interest due to ease in their implementation [66,67,105]. In this work, we focus on the combination of radial k-space sampling and GRAPPA, which has been successfully demonstrated on a variety of CMR applications [68,78,79,101,106], and has been implemented with low-latency real-time reconstruction [107], making it a viable tool for real-time CMR imaging. After incorporating a through-time calibration scheme, radial GRAPPA has achieved acceleration factors ≥ 8 [68,107,108].

Though the reported image quality has been acceptable qualitatively and possessing diagnostic potential [77,79,101], there exists a lack of thorough analysis of the technique. The main error metric that has been used to quantify performance is image-based root-mean-square-error (RMSE), which is problematic. The RMSE is computed from the RMS value over the pixels of an absolute difference image that is created by subtracting the intensities of a *gold-standard* image frame, reconstructed using a calibration scan composed of 400 fully sampled frames without any through-k-space kernel repetition. The RMSE values reported, thus, are fundamentally biased since the gold standard images are essentially subjective, being generated from the technique itself. Other than the use of simulated phantoms, it is impossible to determine ground-truth for moving objects such as the heart due to limits in temporal resolution and scan duration. On the other hand, real-time MRI methods, especially those involving parallel imaging, cannot be appropriately tested on static objects since calibration on stationary objects will inevitably overfit to the static image and the reconstructions will not generalize on the actual accelerated frames. Conversely, for simulations incorporating individual receiver coil data in k-space to be performed in an accurate manner, mathematical equations formulating the convolution of the spatial frequency domain representation of a moving phantom with that of realistic coil sensitivity profiles, ideally calculated from Biot-Savart equations, need to be derived, and though there have been studies aimed at realizing such software [109–113], there is no one tool that is agreed upon and most studies in the field of real-time MRI do not employ accurate simulations of this nature in their methods.

Image-based RMSE is a coarse metric that yields a global measure of error. Even though errors on individual pixels are taken into consideration, there is no direct relation to the accuracy in the estimation of missing k-space points. Through-time radial GRAPPA calibration is a significant improvement over the original radial GRAPPA, simply populating the calibration data with more observations is not sufficient to determine the robustness of the estimation process, especially in a typical but non-ideal setting in which signal-to-noise ratio (SNR) is poor.

Therefore, performance metrics that quantify estimation error directly on k-space are of interest to better understand the accuracy of the radial GRAPPA weights calibration.

Radial GRAPPA is essentially composed of a linear regression model at every target k-space point. Thus, it can naturally be subjected to standard validation methodologies that are commonly used by other machine learning algorithms. One such methodology is cross-validation (CV) [114–116], which is a popular model validation strategy. The goal of cross-validation is to understand how a statistical model will perform on new, unseen data, which is often referred to as generalization performance. Though variable in actual implementation, CV partitions the data set into training and test sets where the model is trained only on the former and cross-validation estimates, or in other words out-of-sample estimates, are obtained by applying the model on the latter. In the setting of real-time accelerated MRI, cross-validation can be used to yield estimates on the accuracy of radial-GRAPPA-reconstructed k-space points on accelerated frames.

In this work, we investigate the fidelity of the through-time radial GRAPPA calibration in real-time cardiac imaging on a set of human subjects, adopting a performance metric based on K-fold cross validation [115,117]. Proposing a methodology for quantifying the generalization accuracy of through-time radial GRAPPA reveals the limitations of this parallel imaging technique in addition to providing a framework for guiding choices of calibration parameters. The CV-based validation metric is shown to be consistent with image quality via comparisons of radial GRAPPA reconstructions with varying degrees of generalization accuracy. Moreover, substantial influence of the underlying signal-to-noise ratio (SNR) on calibration accuracy is discovered, and a mathematical model to estimate the accuracy metric from the SNR is presented.

2.2 Theory

2.2.1 Background: Through-time Radial GRAPPA Calibration

Acceleration in radial imaging is typically achieved by acquiring only every 1 out of R consecutive radial projections, where R is the acceleration factor (Fig. 2.1). With radial GRAPPA, the missing (unsampled) projections are estimated as weighted linear combinations of sampled points on acquired projections in the neighborhood. Using a typical GRAPPA kernel of size $N_B = B_y \mathrm{x} B_x = 2\mathrm{x}3$, a missing point is estimated from B_x=3 points lying on each of B_y=2 acquired projections on either side of the missing projection, where the middle points are chosen to have the same readout location and the others being adjacent to that center point on the same projection (Fig. 2.1). In addition, acquired samples from all receiver coils contribute to the estimation of missing points on any other coil, thus, yielding a linear system with $B_y \mathrm{x} B_x \mathrm{x} N_{coils}$ unknowns, namely the GRAPPA weights. To obtain observations for this linear system, a calibration scan consisting of N_{full} fully-sampled frames is performed. For each missing point, data from a segment of fully-sampled k-space centered around this point, spanning N_{seg_read} and $N_{seg,proj}$ repetitions along the readout and azimuthal dimensions, respectively. In combination this calibration strategy including both through-space and through-time segments yields $N_{full} \mathrm{x} N_{seg\_read} \mathrm{x} N_{seg,proj}$ GRAPPA kernel replicates as observations [68].

2.2.2 K-Fold Cross-Validation

Cross validation requires no assumptions about the underlying statistical properties of the data or the model being trained unlike other model validation methods such as the Akaike Information Criterion [118,119] or the commonly used adjusted R-squared [120,121]. Simple CV is performed by dividing the dataset into a training set and a test set and computing the measure of fit on the test set after the model is fit to the training set. This yields one estimate of the generalization error and to increase the number of estimates exhaustive CV methods such as

Leave-p-out CV (LPOCV) can be used. With LPOCV, p observations are assigned to the validation set and the remaining N-p observations are used to train the model at each round, with all possible $\binom{N}{p}$ splits providing measures of fit, where N is the total number of observations in the dataset. The CV error is then obtained as the average over all error estimates. Though statistically neat, LPOCV is computationally intensive, and thus, is rarely used. Alternatively, K-fold CV reduces the number of training rounds down to a small integer K. The original dataset is partitioned into K nearly equal subsets, and at each round, a single subset is used as the test set and the remaining K–1 partitions as the training set, yielding K estimates of generalization performance. In this work we use K-fold CV and as there is no universal consensus on an optimal choice of K, though typical values range between 5 and 10, we use 6 folds.

The observations in the dataset for radial GRAPPA are essentially populated in two orthogonal dimensions: k-space and time. On aggregate, there are $N_{seg,read}$x$N_{seg,proj}$xN_{full} observations to one's disposal, but it is essential that when observations are used in a validation set, they do not share the same temporal location of any observation included in the training set that generated the model. In other words, generalization performance is relevant only for distinct time windows, and using observations from the same fully-sampled frame that only differ in their k-space positions in a training/validation set pair will unfairly bias the estimates of generalization error. To avoid such "in-time" validation, the CV splits were performed only along the N_{full} calibration frames as depicted in Figure 2.2.

2.2.3 Predicted R-Squared

The magnitude of k-space signal varies significantly from region to region, making RMSE or mean absolute error unsuitable error metrics. A scale invariant error metric, such as RMSE normalized by the range of the magnitude of the signal (nRMSE) could provide a more meaningful metric, yet it still would not explain the performance in terms of the fraction of explained variance. The r^2 coefficient, where r is the coefficient of determination, is closely related to RMSE, and thus, is another popular choice for quantifying the performance of regression models, particularly linear ones [120]. Conventionally, r^2 is calculated on the errors of the training samples, and can thus be improved simply by adding more co-variates to the model. To avoid overfitting the model to the training set, *adjusted* r^2 can be used as it normalizes by the degrees of freedom. Yet, since it is also computed solely on training samples, *adjusted* r^2 is a poor choice for estimating generalization error. In this work, we adopt *predicted* r^2 as the primary evaluation criterion, which is obtained by calculating r^2 on hold-out (validation) partitions of the calibration data. For each k-space point to be estimated with signal $S(\vec{k},t)$:

$$r_{val}^2 = 1 - \frac{\left\| S_{val}(\vec{k},t) - \widehat{S_{val}(\vec{k},t)} \right\|^2}{\left\| S_{val}(\vec{k},t) - \overline{S_{val}(\vec{k},t)} \right\|^2} \tag{2-1}$$

$\widehat{S_{val}(\vec{k},t)}$ denotes the reconstructed target points on a validation fold by applying the GRAPPA weights that are determined from the training folds. r_{val}^2 describes the the r-squared on this particular validation fold, and *predicted* r^2 is computed as the mean of all such r_{val}^2 (from the *K* distinct folds) and reported as the metric for generalization performance (Fig. 2.2). The norms and the mean values as in $\overline{S_{val}(\vec{k},\vec{t})}$ are calculated over the grid defined by the cross product of the k-space segment $(\ \vec{k}\ )$ and the validation-fold frames (t).

One distinction between traditional r^2 and *predicted* r^2 is the range of values. Assuming an intercept term is used, $r^2 \in [0,1]$, where 0 means model has a constant output, equal to the mean of the response variable for any observation, and 1 implies a perfect fit and all values in between reflect the fraction of variance explained by the model. Conversely, *predicted* r^2 is evaluated on observations that are unseen by the model, the mean of the response variable on that set is unknown and it is therefore possible to have models with predictions that result in larger errors than a model simply predicting the outcome with its mean leading to $r^2 \in (-\infty, 1]$.

2.3 Methods

2.3.1 Data Acquisition

In vivo cardiac imaging was performed for human subjects (N=8) under free breathing and no ECG gating with informed consent, having obtained IRB approval. Images were acquired using a balanced steady-state free precession (bSSFP) pulse sequence, with a metronome-like view ordering [68] to prevent eddy currents, on a 1.5T scanner (Avanto, Siemens Medical Solutions, Erlangen, Germany) with the following parameters: Field-of-view(FoV)=250mm^2, slice thickness=8.0mm, flip angle=45°, TR=2.8-3.2 ms (TE=TR/2) and N_{coils} = 15 that were made up of standard chest (2x3=6) and spine (3x3=9) arrays. Two separate matrix sizes of 128x128 and 192x192 were employed in the reconstruction of the images, which were determined by the scan readout length. With double oversampling, 128x128 images were generated from scans with 256 samples per readout projection and 192x192 images were generated from those with 384 samples per readout projection, resulting in spatial resolutions of 1.95x1.95mm^2 and 1.30x1.30mm^2 respectively. The number of projections in a fully sampled calibration frame for each setting was N_ϕ = 144 and N_ϕ = 192, with various acceleration factors in the range R = [6, 12] being used for the accelerated real-time frames.

2.3.2 Image Reconstruction

2.3.2.1 Standard Through-Time Radial GRAPPA

All image reconstruction was performed in MATLAB (R2014a, MathWorks Inc., Natick, MA) on a dual-socket six-core Intel Xeon E5-2620 v2 at 2.10 GHz system. The MATLAB implementation of through-time radial GRAPPA was used for GRAPPA weights calibration and reconstruction of full radial k-space data from undersampled frames, and non-uniform FFT[9] was utilized for reconstructing images from radial k-space data. Radial GRAPPA segment sizes of $N_{seg} = \{1x1, 4x1, 8x2, 16x4\}$ were chosen for radial GRAPPA calibrations with corresponding fully sampled calibration frame numbers of $N_{full} = \{396, 78, 24, 6\}$. As previously mentioned, K-fold CV partitioning is carried out only along the N_{full} dimension, and in order to use the same K, the values of N_{full} for each GRAPPA segment setting had to be divisible by the K of choice. To this end, K was chosen as 6.

2.3.2.2 Alternative Through-Time Radial GRAPPA Reconstructions

Alternatively, two different radial GRAPPA reconstruction methods were developed with slight modifications to the standard TT-rGRAPPA reconstructions. As the *predicted* R-squared (via K-fold CV) are computed for every target k-space location, the missing points on the accelerated frames' k-spaces are imputed if their *predicted* R-squared values are lower than a predefined threshold/cutoff value whereas the ones with *predicted* R-squared over this cutoff are estimated via the GRAPPA weights as in standard TT-rGRAPPA. For the first modified reconstruction, zero imputing was performed, and for the second, the mean value of the target points on the specific k-space location over all the fully sampled calibration frames was assigned to the missing point on the accelerated frames. These modified reconstructions are referred to as TT-rGRAPPA Zero-Fill and TT-rGRAPPA Mean-Fill, respectively, in the remainder of this chapter. Such modifications were introduced as an effort to test the significance of the radial GRAPPA reconstructions for calibrations with low generalization predictive power. Reconstructions with a cut-off value of $r^2_{cut\text{-}off} = 0$ are particularly insightful as zero *predicted* R-squared can be achieved by simply imputing the missing k-space point using a constant which is the mean of the actual/true values over the same frames, without any contribution from the source projections, independent of the cardio-respiratory position. TT-rGRAPPA Mean-Fill reconstructions emulate this phenomenon although the true mean values of the missing points in the accelerated frames are unknown, but the means over the calibration frames provide adequate surrogates.

2.3.3 Investigation of Calibration Accuracy

2.3.3.1 Reference for Computing the Predicted R-squared

As explained in the Theory section and illustrated in Figure 2.2, *predicted* R-squared (*predicted* r^2) values are computed between the target points of the k-space data on a validation fold and the radial GRAPPA predictions of the same points by the weights calculated using the calibration data from the remaining K-1 folds. In this setting, the validation partition includes all the target points inside the radial GRAPPA segment, repeated over all the fully sampled frames that belongs to that particular fold, yielding a total of $N_{seg,read}$ x $N_{seg,proj}$ x (N_{full}/K) data points that get included in the R-squared computation. Since R-squared is computed over the entire radial GRAPPA segment, this particular metric produces prediction accuracy estimates with respect to (w.r.t) the through-time/through-k-space radial GRAPPA technique. To give a concrete example, *predicted* r^2 values computed for N_{seg}=8x2 yield goodness-of-fit measures for the radial GRAPPA calibration using the same segment size N_{seg}=8x2, and thus, do not estimate the accuracy of the radial GRAPPA reconstructions on real-time accelerated frames because using a k-space segment larger than N_{seg}=1x1 itself introduces a certain level of inaccuracy. In order to get accuracy measures on the radial GRAPPA reconstructions of missing points on accelerated frames, we propose an alternative *predicted* r^2 calculation where validation folds only use the center point of the segment (the original k-space position of the missing point) and all 396 frames are used in the process, leaving 66 k-space points on 396/6 = 66 frames on a single validation fold. The GRAPPA weights computation is identical to the original *predicted* r^2 computation scheme as calibration data consists of $N_{seg,read}$ x $N_{seg,proj}$ points from each frame on the training partitions with one exception: instead of using all remaining 396-66 = 330 frames, a subset of N_{full} frames are randomly sampled in constructing weights training data set, where N_{full} is determined by the respective segment size $N_{seg.}$ We denote this metric as "*predicted* r^2 w.r.t Ground Truth" as it emulates the radial GRAPPA reconstruction of missing target points where the validation folds present surrogate samples for the hypothetical scenario of observing the missing points during the accelerated real-time frames. The original *predicted* r^2 metric is referred to as "*predicted* r^2 w.r.t radial GRAPPA" and is also the implied version when the reference (radial GRAPPA vs ground truth) for the R-squared computations is omitted.

2.3.3.2 Predicted R-squared versus Signal-to-Noise Ratio

When *predicted* R-squared values were investigated, the patterns in the k-space closely resembled those of signal power, independent of acceleration factor, azimuthal angle or readout location. This suggested signal-to-noise ratio (SNR) as an important factor in the accuracy of radial GRAPPA calibrations. To further investigate a possible relationship between SNR and calibration accuracy, SNR values for every k-space point on calibration frames were estimated using Matlab's Signal Processing Toolbox. Briefly, the SNR calculation on a time-domain signal is carried out using the periodogram method with a Kaiser window. The periodogram estimates the fundamental frequency, and the central moments of all adjacent spectral components decreasing monotonically away from this maximum [122,123] contribute to the signal power as well as those of higher harmonics that reside at integer multiples of the fundamental frequency. The SNR is then computed in decibels (dB) after estimating the noise power as the median power in the regions of the spectral density containing only noise. Since k-space signal lies in the complex space, SNR values were calculated for both the real and the imaginary parts of the k-space samples.

To check the hypothesis that *predicted* R-squared is a function of SNR, an effort towards developing a generalizable mathematical model, purely based on SNR, that estimates the *predicted* R-squared was deemed worthy. For the sake of building such a generalizable model, a simple linear regression came forth as a natural choice. However, after initial explorations, the distribution of SNR was found to be highly skewed, and thus, SNR values were logarithm transformed prior to fitting the model. The predictor variables in this model mainly consisted of the SNR of the target point and the mean and standard deviations of SNR values across the source points corresponding to the same target point where all such target points on a fully sampled calibration k-space were used as observations in the same model without any segmentation over k-space regions or receiver coils. As through-time radial GRAPPA calibration accuracy, measured in *predicted* R-squared, varies across the choices of grappa segment used, a separate model for every grappa segment was trained.

To demonstrate the generalizability of such SNR-based models, training data were selected from the calibration k-spaces of one or more human subject scans, simply stacking observations regardless of which human scan they resulted from, and *predicted* R-squared of calibrations for other human subjects' scans were predicted via applying the trained models. Out-of-slice predictions were also performed as the training and testing data for the SNR-based models belonged to not only different volunteers, but also different short-axis slices.

2.4 Results

2.4.1 Distributions of Predicted R-squared

Figure 2.3 displays the density distributions of the *predicted* R-squared values on data acquired from a human short-axis slice, estimated via smooth function approximations based on the underlying histograms, for both versions of the metric using the standard radial GRAPPA calibration as well as the ground truth (sans through-k-space component) as the respective reference. The top row displays distributions for both versions of *predicted* R-squared for radial GRAPPA calibrations of R=9 times undersampled data using all 4 radial GRAPPA segment sizes whereas the bottom row shows the distributions of the two for radial GRAPPA calibrations on data at various undersampling factors using a segment of N_{seg}= 4x1. The first of the many insights that stands out from this figure is that each particular density curve is bimodal, having one peak near 1.0 and another one centered in the negative side of the *predicted* r^2 axis, usually around or to the left of the -0.5 mark, with the rest of the density distributed in between in a rather smooth manner. This suggests that there are two distinct underlying populations for the measure of accuracy: one that is associated with missing target points for which the radial GRAPPA calibration is highly accurate and one associated with points for which the calibration is significantly erroneous (*predicted* $r^2 < 0$). The overall density distributionore, appears to be a sum of two normal distributions where the former resembles a truncated normal ($\leq$ 1.0) with a generally much smaller standard deviation (sharp peak) and the latter one with longer tails that seem to constitute a significant portion of the population. Another insight gained from this figure is that the acceleration factor (R) has very little impact on the *predicted* R-squared, and thus, on the accuracy of the calibration process. In a R=12 undersampled k-space, there are over twice the number of missing target points than that of a R=6 undersampled k-space, where the distances of more than half such points to their respective source projections are greater than those of all missing points on the 6-fold undersampled k-space, yet, this substantial increase in source-to-target distances do not appear to have a major effect since the *predicted* R-squared distributions are very similar for radial GRAPPA calibrations from R=6 to R=12. While still minimal, the discrepancy is more distinguishable for *predicted* R-squared values computed w.r.t ground truth. Moreover, on the top left, the effect of the segment size on the accuracy of the radial GRAPPA calibration process is demonstrated. The setting using N_{seg}= 1x1 is equivalent to using the same choice of segment size to estimate the *predicted* r^2 w.r.t ground truth, and is clearly the scenario where the radial GRAPPA calibration process (including points over the entire radial GRAPPA segment in validation) is the most error prone. On the other hand, the graph on the top right demonstrates the opposite where the N_{seg}= 1x1 is the more accurate choice, as expected, from the perspective of estimating the actual missing points on an accelerated k-space frame. This particular result validates previous work[68] that investigated the effect of the segment size in radial GRAPPA using a different error metric. Similar to Figure 2.3, Table 2.1 shows the distributions of the *predicted* r^2 values associated with calibrations for an acceleration factor of R=9 by listing its deciles across data acquired from 8 different volunteers. The values for the 5th and 6th (%50 and %60) deciles are significantly higher for N_{seg}= 4x1, 8x2 and 16x4 than those of N_{seg}= 1x1, suggesting that radial GRAPPA weights have much more difficulty generalizing across time than across k-space.

2.4.2 Standard versus Alternative Radial GRAPPA Reconstructions

Figure 2.4 shows end-systolic and end-diastolic images from a human short-axis slice reconstructed with the standard (TT-rGRAPPA Standard) and alternative (TT-rGRAPPA Zero-Fill and TT-rGRAPPA Mean-Fill) through-time radial GRAPPA methods on data acquired with various undersampling factors (R=6,9,12). The cutoff value of the *predicted* R-squared used in the alternative TT-rGRAPPA methods was chosen as $r^2_{cut\text{-}off}$ = 0 and a radial GRAPPA segment of N_{seg}= 4x1 was used for all reconstructions. It is very clear from this figure that the radial

GRAPPA calibration process for missing points where *predicted* $r^2 < 0$ is pointlessly ineffective as simply imputing such missing points on accelerated frames with zeros (via TT-rGRAPPA Zero-Fill) result in indistinguishably similar images with their standard TT-rGRAPPA counterparts. Such points make up of about the bottom 40% of all missing points estimated via radial GRAPPA across the board (for various R and N_{seg}) as shown in Table 2.1, and therefore, constitute a significant portion of the overall radial GRAPPA process in magnitude. The RMSEs, computed as the mean values of RMSEs with respect to standard TT-rGRAPPA over 200 reconstructed consecutive frames including the respective end-systolic and end-diastolic images displayed, are all around the 0.50% neighborhood and thus, consistent with the striking similarity in the images. Similarly, Figure 2.5 shows end-systolic and end-diastolic images reconstructed with all three TT-rGRAPPA versions (with $r^2_{cut\text{-}off} = 0$) on data from another human short-axis slice acquired with an undersampling factor of R=9. The RMSEs are slightly higher on this human volunteer's data than the one shown in Figure 2.4 when the alternative TT-rGRAPPA reconstructions on the [N_{seg}= 4x1, R=9] setting of each are compared, however, the discrepancies between the standard and alternative reconstructions are near non-existent. Nevertheless, some blurring can be detected if zoomed in around the papillary muscles.

2.4.3 Effect of Predicted R-squared on Image Quality

Figure 2.6 displays end-systolic and end-diastolic images from a human short-axis slice, reconstructed with N_{seg}= 4x1 and varying degrees of *predicted* R-squared cutoff values for the alternative TT-rGRAPPA methods on data that is 9-fold undersampled. RMSEs were computed w.r.t the standard TT-rGRAPPA reconstructions ("Original" as in the left-most column) over 200 reconstructed consecutive frames as in Figures 2.4 and 2.5. This figure is aimed at demonstrating the relationship between the significance of the radial GRAPPA estimation and the *predicted* r^2 associated with it. Up to $r^2_{cut\text{-}off} \leq 0.20$, which constitutes the bottom 47.1% of missing points, there is little-to-no visible image degradation, with a very subtle level of sharpness loss, so one can argue that the radial GRAPPA is insignificant for nearly half of the missing points on an accelerated frame when a segment of N_{seg}= 4x1 is utilized. However, omitting the radial GRAPPA estimation for points with *predicted* r^2 in the (0.40, 0.80] range, which amounts to a 15.7% fraction of all missing points, does appear to have impact as images reconstructed with the alternative methods using $r^2_{cut\text{-}off}$= 0.80 do exhibit substantial blurring. Figure 2.7 demonstrates the relationship between the image RMSEs, computed with respect to the standard TT-rGRAPPA, and the $r^2_{cut\text{-}off}$ values for the TT-rGRAPPA Zero-Fill method. For all radial GRAPPA segment sizes, the image RMSE increases smoothly with $r^2_{cut\text{-}off}$. For all segments, the zero-filled reconstructions using $r^2_{cut\text{-}off} < 0.5$ all guarantee image RMSEs no greater than 1.5%, except for N_{seg}= 1x1 where the increase in image RMSE is more steep.

2.4.4 Predicted R-squared versus Signal-to-Noise Ratio

Table 2.2 display the parameters of the models that estimate the *predicted* R-squared from the underlying SNR characteristics of the radial GRAPPA calibration data and Figure 2.8 shows plots of the SNR-based regression model estimates of the *predicted* R-squared against the actual *predicted* R-squared in order to visualize the accuracy of such SNR-based estimation models.

2.5 Discussion and Conclusion

2.5.1 Limitations of Radial GRAPPA

The proposed framework that utilizes a missing-point-level quantitative measure of accuracy (i.e. *predicted* r^2) exposes the pitfalls of the through-time radial GRAPPA calibration scheme. The investigation of the proposed performance metric, *predicted* R-squared, reveals that the GRAPPA-calibrated weights for a significant fraction (≈40%) of the missing points are less effective than simply estimating the missing points with a constant value equal to the average signal intensity over the extent of the time/k-space calibration segment associated with those points, having *predicted* $r^2 < 0$. Moreover, roughly 55% of the points are associated with GRAPPA weights that explain less than half the variance (*predicted* $r^2 < 0.5$) over the same calibration segments that are used to fit those weights – more detailed investigation of the *predicted* R-squared from a percentile point of view is presented in Table 2.1. Even more staggering, these numbers are associated with data acquired with radial readouts that enable only $1.95\text{x}1.95\text{mm}^2$ in-plane resolution and the *predicted* R-squared values decrease even further for readouts stretching further out in k-space (e.g. $1.30\text{x}1.30\text{mm}^2$ per pixel) as the signal-to-noise ratio generally decreases towards the edges of k-space. This explains why through-time radial GRAPPA has been primarily utilized on applications that accommodate images with low-to-mid spatial resolution.

Similarly, the outcomes of the alternative through-time radial GRAPPA reconstructions, namely TT-rGRAPPA Zero-Fill and TT-rGRAPPA Mean-Fill, shed light on the limitations of the through-time radial GRAPPA on the image level. Using progressive values of $r^2_{cut\text{-}off}$ to replace significant fractions of radial GRAPPA estimations by zero (via TT-rGRAPPA Zero-Fill) lead to very little, if at all, image degradations, mostly in the form of minimal blurring, up to $r^2_{cut\text{-}off} = 0.40$. This essentially validates the metric, namely *predicted* R-squared, proposed in this work to quantify the accuracy of the radial GRAPPA calibration as the use of radial GRAPPA with low values of *predicted* r^2 is shown to have little-to-no impact on the reconstructed image. The reason *predicted* r^2 is a reliable approximation of generalization performance is due to the fact that it is computed on validation folds (via K-fold CV). Based on the discrepancies between images reconstructed with standard TT-rGRAPPA and TT-rGRAPPA Zero-Fill (Figures 2.6, 2.7) from a variety of normal volunteer scans, expected loss in image quality in an arbitrary radial-GRAPPA-reconstructed image can be approximated if one chooses to omit k-space points associated with less than a certain *predicted* r^2 value.

2.5.2 Significance of Signal-to-Noise Ratio

As suggested by Figure 2.8, signal-to-noise ratio (SNR) is the main underlying driver of *predicted* R-squared, and thus, the accuracy of through-time radial GRAPPA calibration. A very simple linear regression model that uses the SNR of the target and source points -- after log transformation -- in a GRAPPA kernel can yield estimates of "*predicted* r^2 w.r.t radial GRAPPA" with r-squared values in the 80-85% range. These r-squared numbers attached to the SNR-based "*predicted* r^2 w.r.t radial GRAPPA" estimation models are also cross validated such that they indicate the percentage of variance in the *predicted* r^2 values for the TT-rGRAPPA-calibrated missing points on volunteer scans that were not used as part of training data for the models, providing realistic, generalizable measures.

The benefit of these SNR-based models (one for each segment size) is two fold: Firstly, one can approximate the *predicted* R-squared for missing points, with a certain degree of accuracy, directly after calculating the SNR (from the repetitions of the k-space points in the fully sampled calibration frames) without having to perform weights calibration and target point reconstruction for K (e.g. 6) times. Essentially, the model can be applied to GRAPPA kernels on the entire k-space at once to generate *predicted* r^2 approximations, revealing the expected accuracy of the radial GRAPPA calibrations, orders of magnitude faster than computing the actual *predicted* r^2 values. Given a minimum value of *predicted* r^2 that can be chosen by the user (clinician / MRI technologist) of the radial GRAPPA reconstructions, below which radial GRAPPA can be considered ineffective, this pre-computed insight about the *predicted* r^2 per point (i.e. GRAPPA kernel) can enable faster GRAPPA calibration and reconstruction times on the fly for the real-time reconstruction setting [107] via bypassing the weights calibration for a substantial fraction of the GRAPPA kernels where the approximated *predicted* r^2 is below that threshold. This would also significantly reduce the amount of RAM required in the GPU(s) on which the GRAPPA weights need to be readily available for on-the-fly image reconstruction. Secondly, a direct mathematical relation between SNR and *predicted* r^2 allows for the determination of the necessary boost in SNR to achieve a certain increase in the *predicted* r^2 that would yield more accurate GRAPPA calibrations. Assuming certain baseline values for the standard deviation of SNR among the source points as well as the condition number, minimum boosts in SNR_{target_real}, SNR_{target_imag}, $SNR_{mean\_source\_real}$ and $SNR_{mean\_source\_imag}$ in the log scale over baseline values (that correspond to the average *predicted* r^2 of ≈0.27) required to achieve a certain *predicted* r^2 could be determined by distributing the Δ*predicted-*r^2 to these four quantities with each required boost being inversely proportional to their respective model coefficients. This can act a guide when adjusting the imaging setting (receiver coil selection / orientation) and/or the scan parameters (TR bandwidth) that may improve the SNR.

2.5.3 Limitations and Future Work

It should be noted that the predictive models that estimate the *predicted* r^2 can be improved in their predictive power (r-squared / rmse) beyond a simple linear regression model with few covariates as there are more than enough observations – with GRAPPA kernels throughout the entire k-space across multiple scans (volunteers) worth of data – to accommodate a much more complex model, with interaction terms and/or the use of decision trees, gradient boosted trees, support vector machines etc., without the risk of overfitting it to the particular data it is trained on. However, a more complicated model also leads to a much less interpretable one, therefore, actionable insights may be less straight forward than the example discussed in the previous paragraph. Moreover, these results are all derived from data acquired from a particular imaging system (1.5T Avanto, chest/spine receiver arrays), and the underlying SNR characteristics of data acquired from a different system and/or application (e.g. joint imaging [124], speech [80]) may be wildly different. It is, therefore, recommended to re-train these SNR-based models on data obtained in the same setting as the TT-rGRAPPA reconstructions are aimed for.

This work focuses primarily on the investigation of the proposed metric, *predicted* r^2 w.r.t radial GRAPPA, which uses the entire calibration data (through-k-space/time) itself as the reference, and provides a valuable method to quantify the significance of the radial-GRAPPA-calibrated weights to be applied on the missing points. On the other hand, the alternative metric, referred to as *predicted* r^2 w.r.t Ground Truth, is the metric that provides estimates of accuracy for the reconstructed missing points with respect to the would-be-acquired points on the same k-space locations at the same time instant, and thus, that would be the metric to obtain the quantitative measures for the fidelity of the radial GRAPPA reconstructions. The limitation of *predicted* r^2 w.r.t Ground Truth, however, is that it would require a numerical simulation that provides ground-truth images for the alternative reconstructions (i.e. TT-rGRAPPA Zero-Fill) with varying degrees of $r^2_{cut\text{-}off}$ in order to investigate the meaning of the metric's values from an image quality perspective. Future work that entails a reliable and realistic numerical simulation can help validate this particular metric as well, which could provide a universal framework by which radial GRAPPA reconstructions can be assessed.

2.5.4 Conclusion

This chapter describes a methodology in quantifying generalization performance of the radial GRAPPA weights calibration on a missing-point level. The methodology is validated via comparisons of the standard through-time radial GRAPPA reconstructions with alternative reconstructions that incorporated the proposed metric. Moreover, the dependence of GRAPPA weights calibration on underlying signal-to-noise ratio is quantified, leading to actionable insights for the utility of the accelerated imaging technique that is the subject of this work.

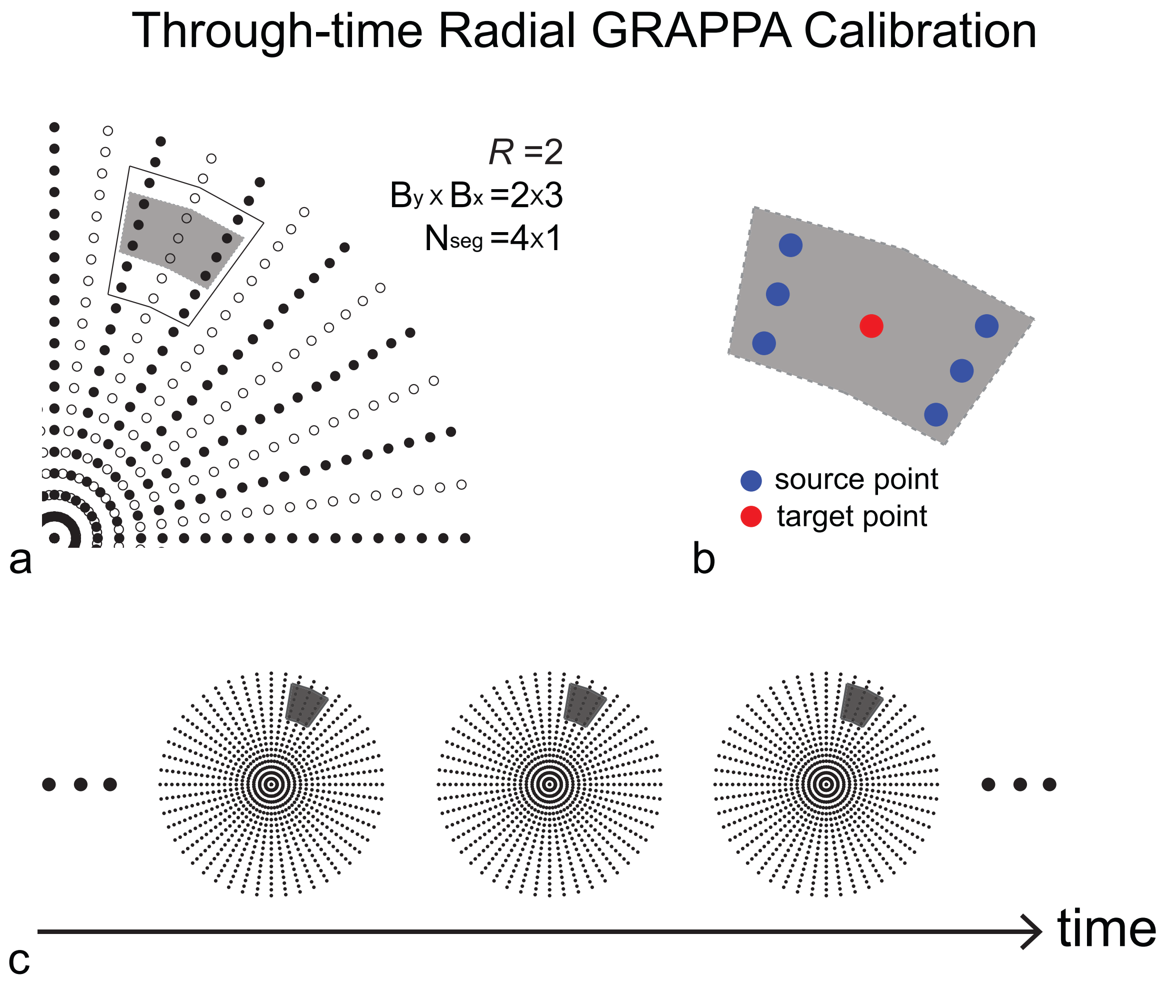

Figure 2.1. Depiction of the through-time radial GRAPPA calibration scheme. A 2-fold undersampled frame is illustrated in **a**, where closed and open circles indicate acquired and missing k-space data, respectively. A GRAPPA kernel (gray box) of B_y x B_x = 2x3 is shown within the k-space segment (solid box) that would yield 4x1 = 4 observations for its weight calibration when a fully-sampled calibration scan frame is utilized. The same GRAPPA kernel is magnified in **b**. The geometries of kernels vary for every target point over k-space. A calibration scan composed of N_{full} successive fully-sampled (closed circles) frames is illustrated in **c**. The same k-space segment depicted in **a** (solid box) is shown on each frame (dark gray shaded) of the calibration scan.

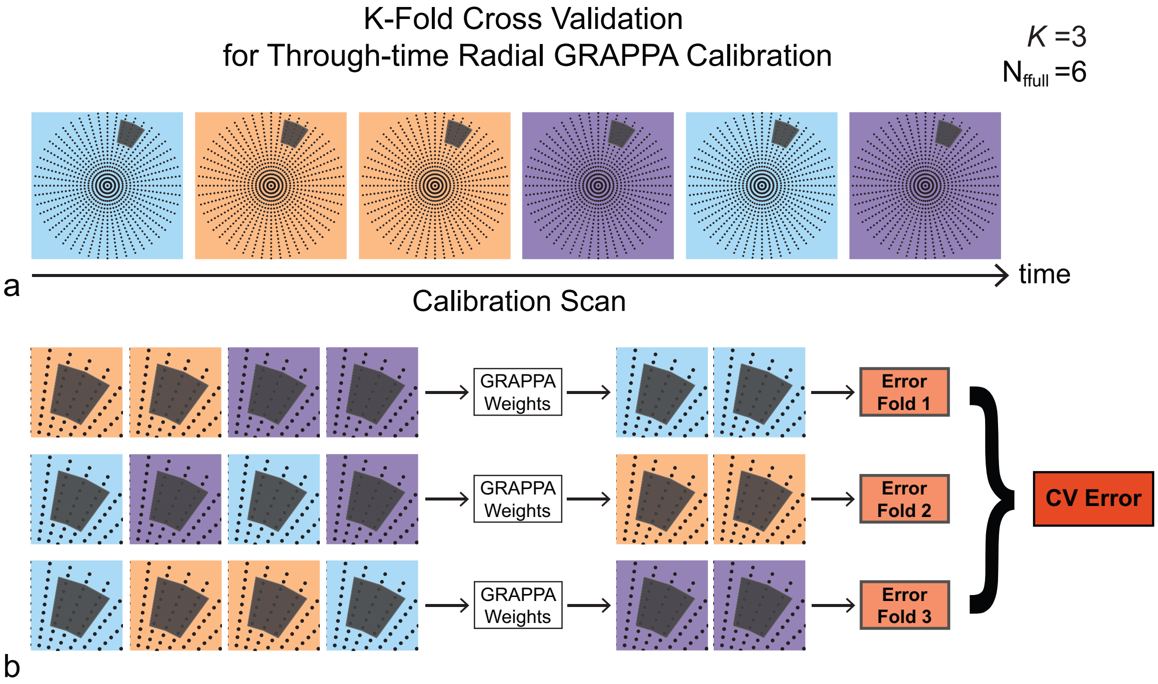

Figure 2.2. Illustration of the K-fold cross-validation method for obtaining generalization error estimates of the radial GRAPPA calibration scheme with a choice of K=3. N_{full} =6 fully sampled calibration frames are depicted in **a**, where the frames in the same CV fold are shaded with the same color. The error (performance metric) is computed on each CV fold after applying the GRAPPA weights, calibrated from data taken from frames excluding that fold, to its source points as depicted in **b**. The reported CV error (or metric) is then obtained by taking the average of the errors computed for each one of CV folds.

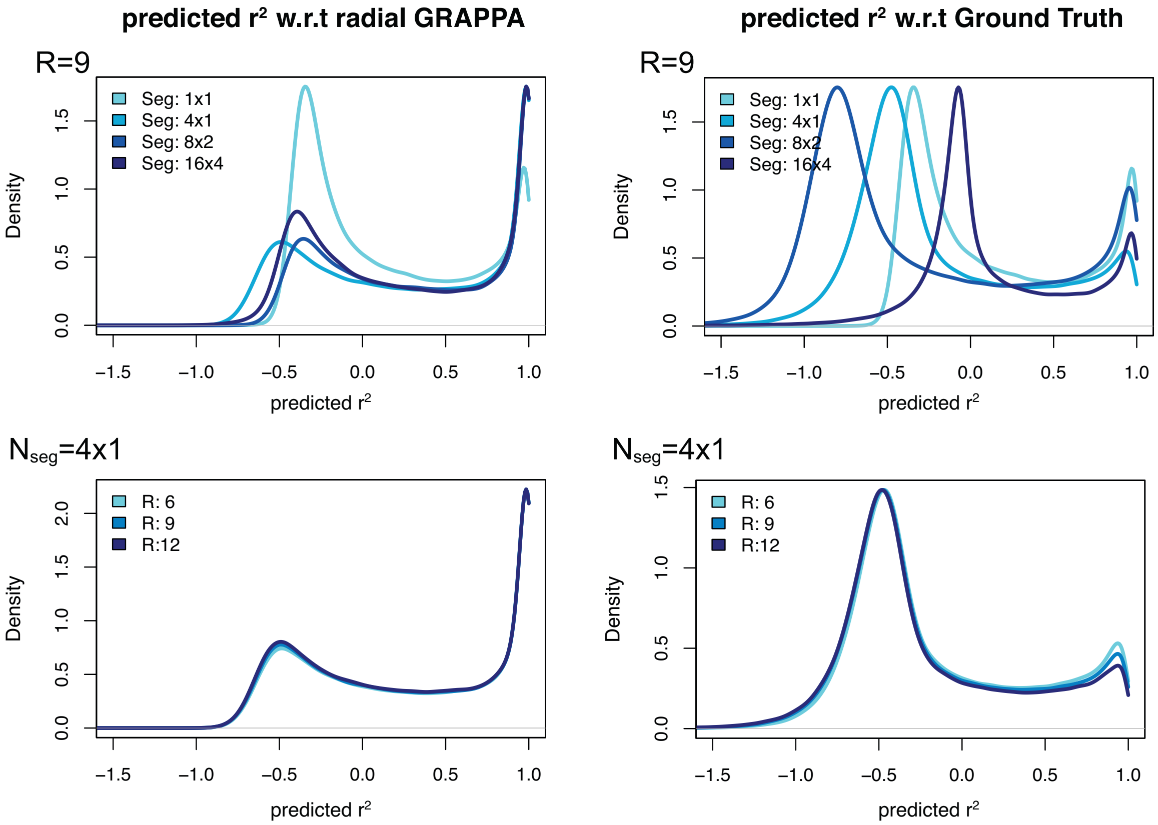

Figure 2.3. Graphs of density distributions of predicted r-squared w.r.t radial GRAPPA and w.r.t Ground Truth on data acquired from a human short-axis slice. Predicted r-squared for various radial GRAPPA segment sizes and acceleration factors are displayed.

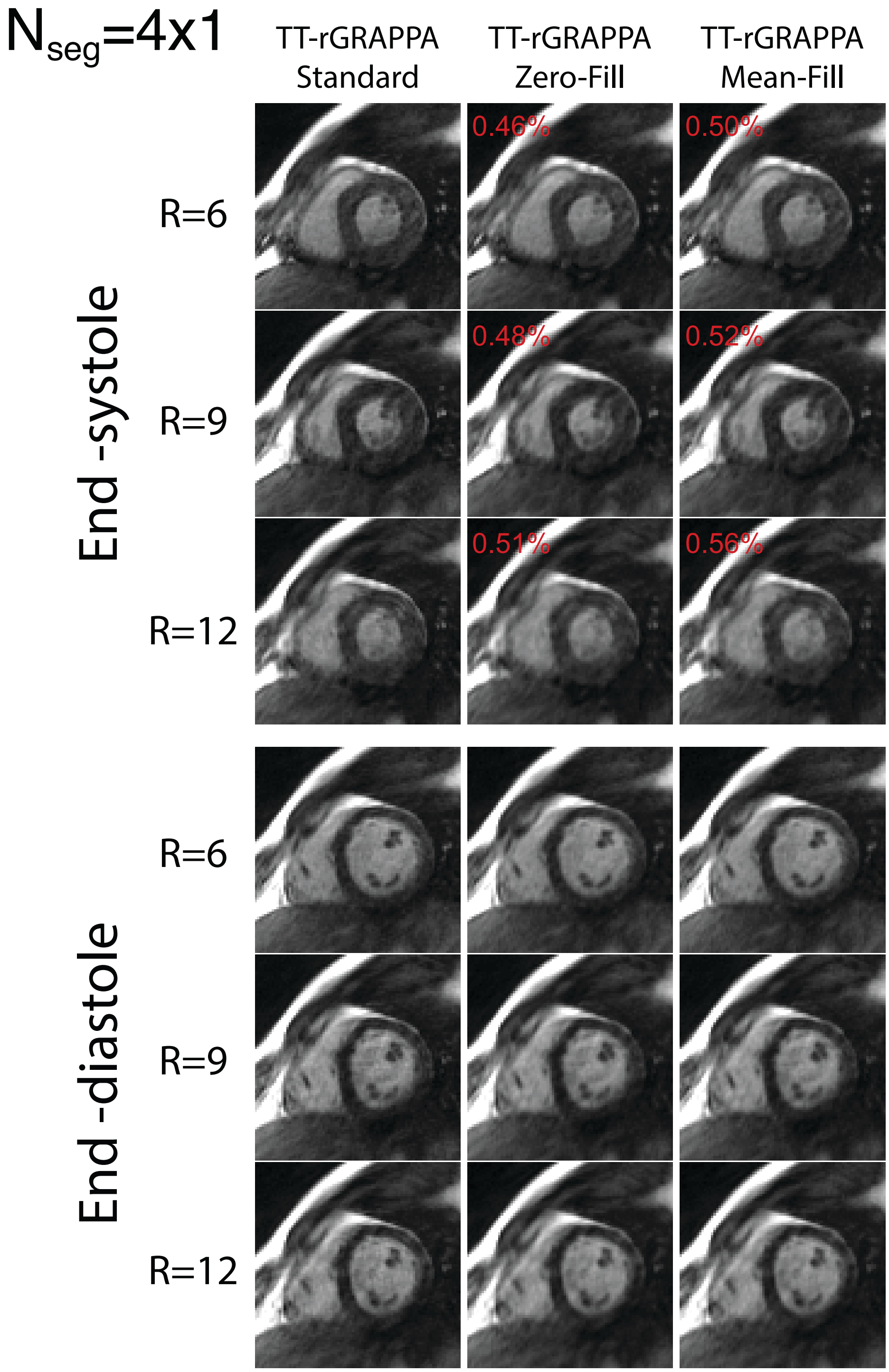

Figure 2.4. Example end-systolic and end-diastolic images from a human short-axis slice reconstructed with TT-rGRAPPA (Standard), TT-rGRAPPA Zero-Fill and TT-rGRAPPA Mean-Fill on data acquired with various undersampling factors. The cutoff values for the TT-rGRAPPA Zero-Fill and TT-rGRAPPA Mean-Fill reconstructions were chosen as $r^2_{cut\text{-}off} = 0$ and radial GRAPPA segment of N_{seg}= 4x1 was used for all reconstructions. Mean values of RMSEs with respect to the standard reconstructions over 200 reconstructed frames for both alternative methods are displayed on their respective systolic images.

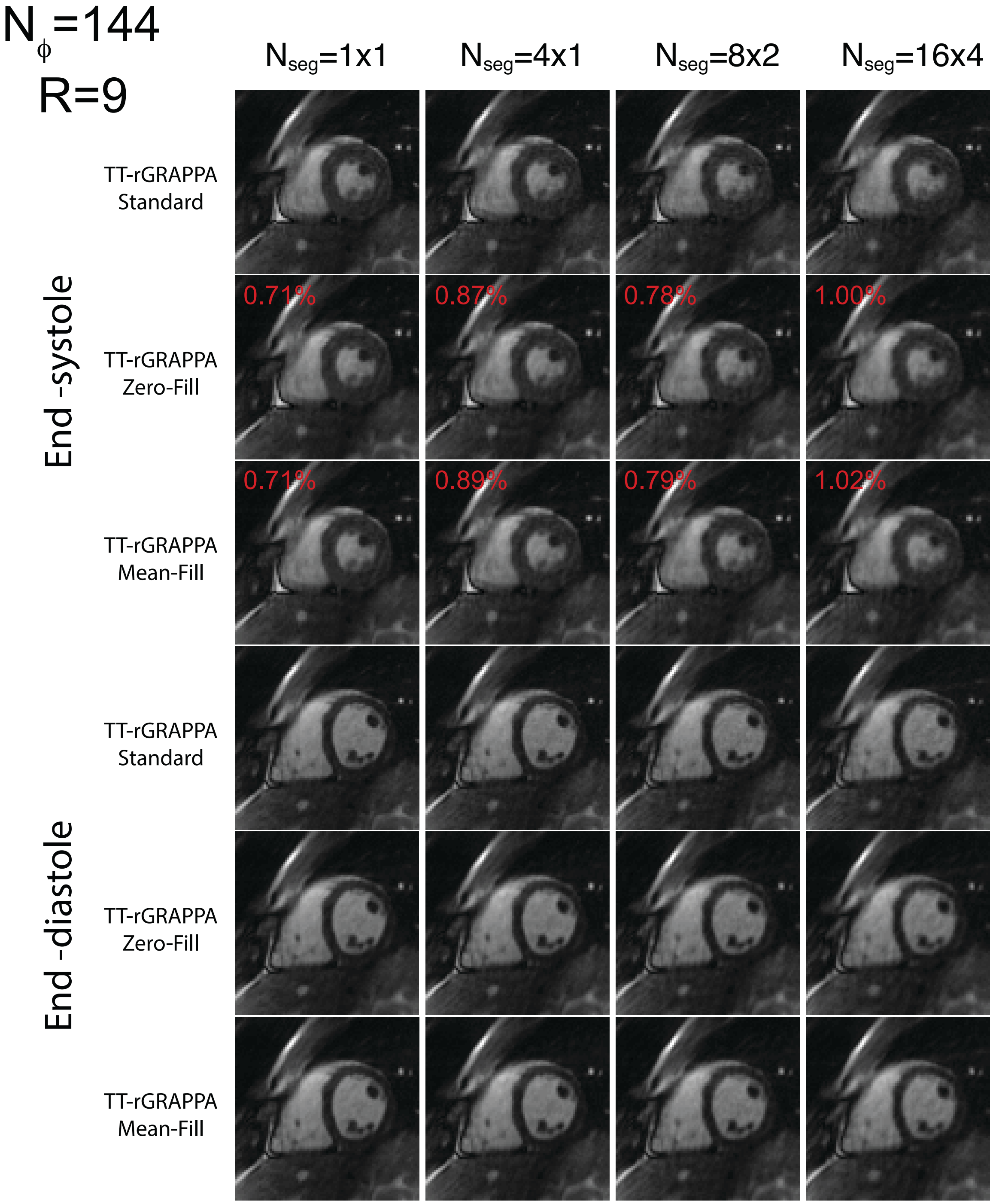

Figure 2.5. Example end-systolic and end-diastolic images from a human short-axis slice, acquired with an undersampling factor of R=9, reconstructed with TT-rGRAPPA (Standard), TT-rGRAPPA Zero-Fill and TT-rGRAPPA Mean-Fill using various radial GRAPPA segment sizes. The cutoff values for the TT-rGRAPPA Zero-Fill and TT-rGRAPPA Mean-Fill reconstructions were chosen as $r^2_{cut\text{-}off} = 0$. Mean values of RMSEs with respect to the standard reconstructions over 200 reconstructed frames for both alternative methods are displayed on their respective systolic images.

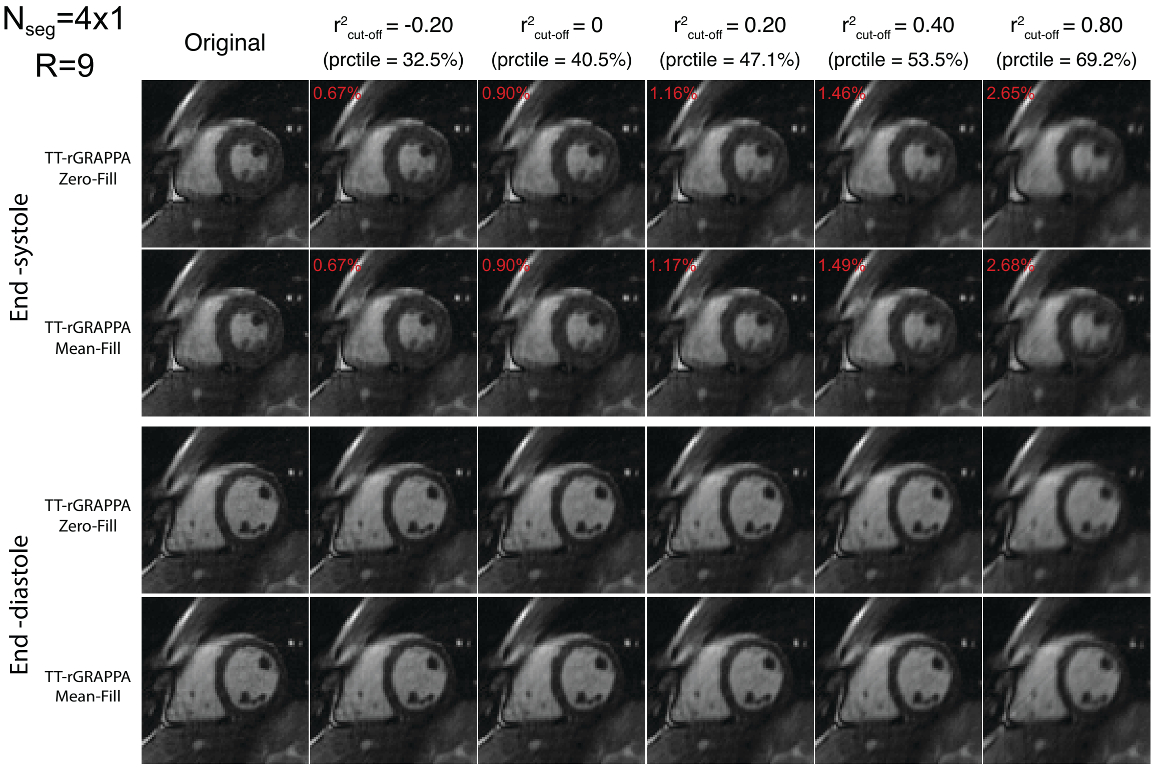

Figure 2.6. Example end-systolic and end-diastolic images from a human short-axis slice, acquired with an undersampling factor of R=9, reconstructed with both alternative TT-rGRAPPA methods using various $r^2_{cut\text{-}off}$ values. A radial GRAPPA segment of N_{seg}= 4x1 was used for all reconstructions. The left-most column (Original) displays reconstructions with no imputing, using the standard TT-rGRAPPA method. Mean values of RMSEs with respect to the standard TT-rGRAPPA reconstructions over 200 reconstructed frames for both alternative methods are displayed on their respective systolic images.

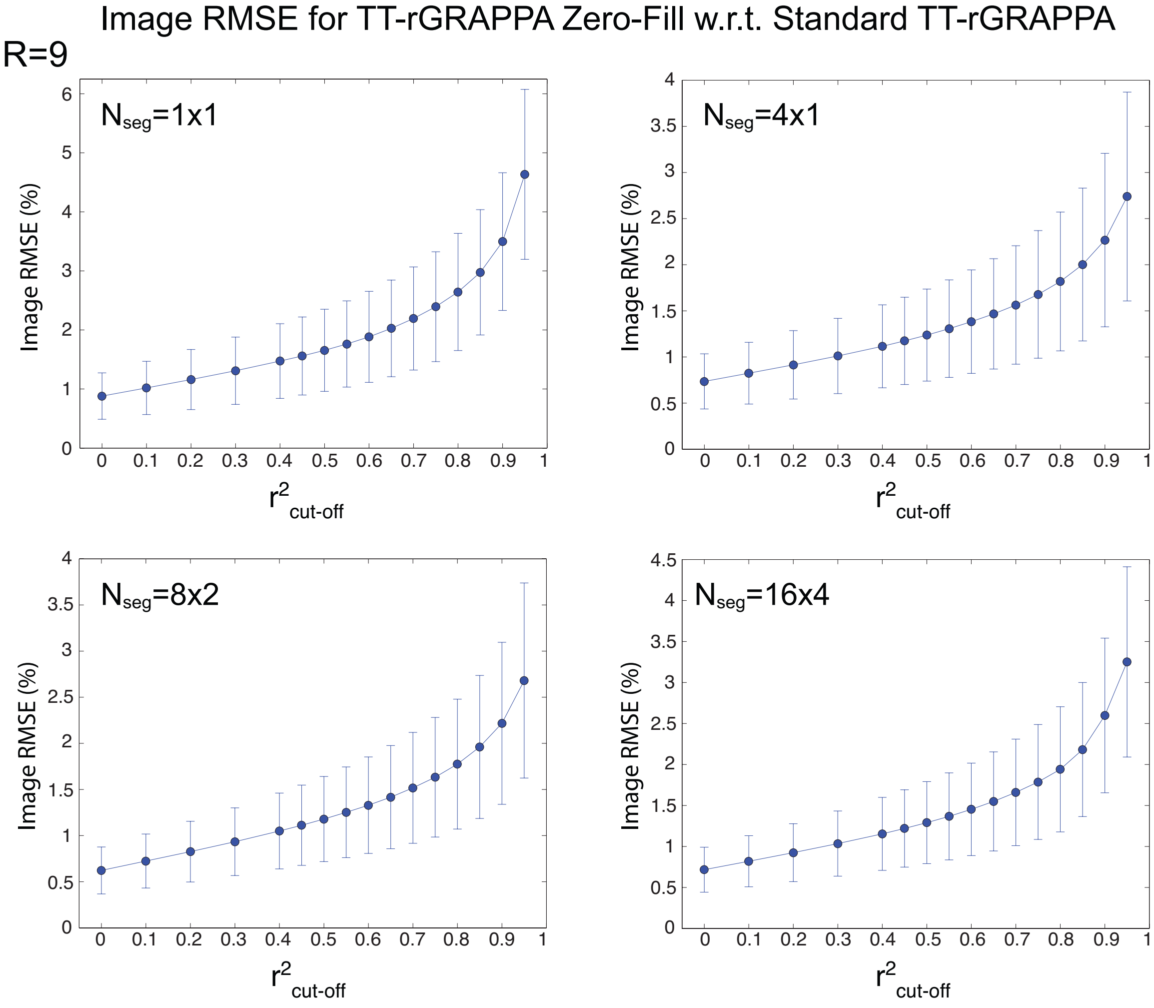

Figure 2.7. Plots of image RMSE with respect to standard TT-rGRAPPA versus $r^2_{cut\text{-}off}$ values for the TT-rGRAPPA Zero-Fill method. RMSEs are computed on images from 8 volunteer scans (mid short-axis slice) and the error bars indicate the standard deviations. The relationship between image RMSE versus $r^2_{cut\text{-}off}$ is plotted for various radial GRAPPA segment sizes, all based on data undersampled with R=9.

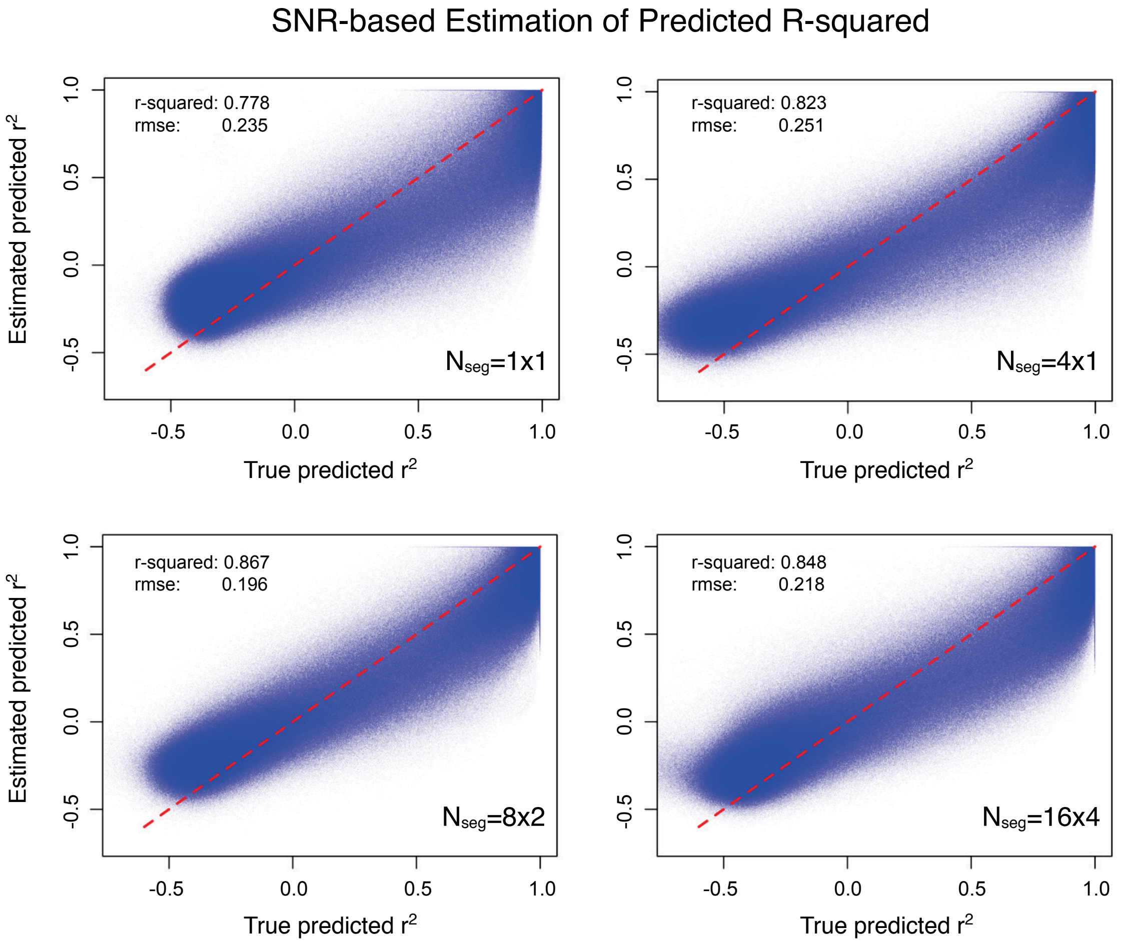

Figure 2.8. Results of the SNR-based predicted R-squared estimation are displayed by plotting the predicted values against the actual ones. For each radial GRAPPA segment size, a regression model trained on data acquired from 7 human volunteers is used to predict the *predicted* R-squared associated with the missing points on the accelerated frames of a different 8th volunteer scan.

Table 2.1. Deciles of *predicted* r^2 values for GRAPPA calibrations for an undersampling factor of R=9. The values are obtained by taking an average (and standard deviation as denoted by ±) of the respective deciles from all (8) volunteer data.

	10%	20%	30%	40%	50%	60%	70%	80%	90%
***predicted* R-squared w.r.t. Radial GRAPPA**									
N_{seg} 1x1	-0.387 (±0.017)	-0.329 (±0.026)	-0.262 (±0.042)	-0.161 (±0.068)	-0.005 (±0.098)	0.217 (±0.117)	0.491 (±0.104)	0.755 (±0.063)	0.934 (±0.022)
N_{seg} 4x1	-0.532 (±0.022)	-0.400 (±0.031)	-0.229 (±0.041)	0.007 (±0.049)	0.302 (±0.045)	0.599 (±0.033)	0.827 (±0.023)	0.952 (±0.013)	0.994 (±0.003)
N_{seg} 8x2	-0.384 (±0.023)	-0.269 (±0.034)	-0.116 (±0.045)	0.098 (±0.058)	0.363 (±0.056)	0.634 (±0.042)	0.843 (±0.026)	0.958 (±0.012)	0.995 (±0.002)
N_{seg} 16x4	-0.430 (±0.021)	-0.331 (±0.029)	-0.204 (±0.042)	-0.014 (±0.058)	0.245 (±0.067)	0.536 (±0.063)	0.789 (±0.047)	0.938 (±0.023)	0.994 (±0.003)
***predicted* R-squared w.r.t. Ground Truth**									
N_{seg} 1x1	-0.387 (±0.017)	-0.329 (±0.026)	-0.262 (±0.042)	-0.161 (±0.068)	-0.005 (±0.098)	0.217 (±0.117)	0.491 (±0.104)	0.755 (±0.063)	0.934 (±0.022)
N_{seg} 4x1	-0.715 (±0.040)	-0.592 (±0.033)	-0.513 (±0.033)	-0.444 (±0.037)	-0.363 (±0.051)	-0.220 (±0.094)	0.049 (±0.121)	0.415 (±0.089)	0.767 (±0.038)
N_{seg} 8x2	-0.964 (±0.021)	-0.855 (±0.025)	-0.771 (±0.034)	-0.676 (±0.054)	-0.523 (±0.098)	-0.253 (±0.146)	0.140 (±0.145)	0.567 (±0.097)	0.878 (±0.037)
N_{seg} 16x4	-0.282 (±0.038)	-0.151 (±0.025)	-0.092 (±0.021)	-0.052 (±0.024)	0.004 (±0.048)	0.130 (±0.082)	0.359 (±0.093)	0.649 (±0.070)	0.890 (±0.033)

Table 2.2. Coefficients of the SNR-based *predicted* r^2 estimation model (linear regression). All models (for each segment size) are leave-one-out cross-validated by using the data acquired from 7 volunteer scans to fit the model coefficients and applying the model to the data of the remaining volunteer scan to get validated predictions. The final coefficients are obtained by taking an average (and standard deviation as denoed by ±) over 8 such models. The r-squared and the rmse of the models are all computed on the validated predictions also. Model coefficients are to be applied after the proper logarithm* transform and standardization.

	Intercept	SNR trg_real	SNR trg_imag	SNR mean_src_real	SNR mean_src_imag	SNR sd_src_real	SNR sd_src_imag	cond. number
N_{seg} 1x1	0.152 (±0.008)	0.141 (±0.004)	0.142 (±0.004)	0.104 (±0.010)	0.164 (±0.012)	-0.042 (±0.011)	-0.050 (±0.009)	0.027 (±0.003)
N_{seg} 4x1	0.268 (±0.003)	0.153 (±0.006)	0.153 (±0.006)	0.200 (±0.019)	0.195 (±0.009)	-0.045 (±0.004)	-0.012 (±0.003)	-0.080 (±0.022)
N_{seg} 8x2	0.337 (±0.004)	0.110 (±0.004)	0.109 (±0.004)	0.222 (±0.007)	0.245 (±0.010)	-0.086 (±0.003)	-0.085 (±0.003)	-0.018 (±0.010)
N_{seg} 16x4	0.273 (±0.005)	0.067 (±0.003)	0.068 (±0.003)	0.227 (±0.011)	0.170 (±0.015)	-0.129 (±0.008)	-0.092 (±0.009)	0.181 (±0.011)

r-squared/rmse: N_{seg}=1x1 0.778/0.235; N_{seg}=4x1 0.823/0.251;
N_{seg}=8x2 0.867/0.196; N_{seg}=16x4 0.848/0.218

* log transform on all covariates except the condition number (cond. number) : $\log_{10}(x+20)$
on cond. number : $\log_{10}(x)$

3 REAL-TIME FREE-BREATHING CARDIAC IMAGING WITH SELF-CALIBRATED THROUGH-TIME RADIAL GRAPPA[1]

---

[1] Adapted from: O. Sayin, H. Saybasili, M.M. Zviman, M. Griswold, H. Halperin, N. Seiberlich, D.A. Herzka. “Real-Time Free-Breathing Cardiac Imaging with Self-Calibrated Through-Time Radial GRAPPA.” Magnetic Resonance in Medicine 2017;77(1):250-264.

3.1 Introduction

Cardiac magnetic resonance (CMR) imaging is a strong clinical tool for the noninvasive assessment of cardiac function [125–127] and cardiomyopathy [128–131]. Conventional segmented cine imaging is ECG-gated and the image quality depends on the regularity of cardiac motion. However, images can be non-diagnostic when cardiac arrhythmias are present or when the patient cannot breath-hold as required. Though several studies have reported promising results with free-breathing cine imaging which utilized various methods that helped avoid breath-holding such as motion correction) [42,43], respiratory navigation [132] or retrospective self-gating [133], these methods have not been widely accepted in clinic. Real-time cardiac imaging removes assumptions of periodicity from cardiac motion and obviates the need for breath-holding, and thus, is an active field of research as a potential alternative to conventional cine imaging [47,134].

To successfully capture wall motion abnormalities and left ventricular function with real-time CMR, each image should be acquired with sufficient contrast and spatiotemporal resolution to accurately delineate endocardial and epicardial borders [24]. If using a standard balanced steady-state free precession (bSSFP) sequence and targeting a temporal resolution of ~50 ms, fewer than 20 phase encoding lines or radial projections can be acquired given that a typical $TR \approx 2.5$ msec. Therefore, parallel imaging (PI) techniques which enable image reconstruction from undersampled k-space by incorporating coil sensitivities in either the image domain [51], or k-space [52] are typically utilized for artifact-free CMR imaging. Nevertheless, in 2D imaging, image quality can suffer for acceleration factors > 4 due to noise amplification inherent in PI [135]. Other techniques that exploit the intrinsic spatiotemporal correlations (i.e. the k-t domain) in cardiac data have demonstrated higher acceleration factors [50,58], but are affected by temporal blurring. Spatiotemporal undersampling has been used in conjunction with the conventional PI methods as well [57,58,136], offering higher acceleration factors for real-time cardiac imaging, but it has been shown to be difficult to achieve 50 ms temporal resolution together with adequate spatial resolution using standard Cartesian k-space trajectories.

Non-Cartesian k-space trajectories, such as radial or spiral sampling, can be undersampled with less coherent aliasing artifacts on reconstructed images compared to Cartesian imaging [11,60,61,64]. For example, up to 3-fold undersampling for radial trajectories have been demonstrated to yield images of good quality without any post-processing [11,63,64]. Additionally, non-Cartesian k-space coverage results in reduced motion artifact, which is important for robust cardiac imaging [59]. Furthermore, non-Cartesian k-space trajectories permit parallel imaging to achieve high acceleration factors in the form of direct extensions of established PI techniques such as Sensitivity Encoding (SENSE) [66,137] or the Generalized Autocalibrating Partially Parallel Acquisitions (GRAPPA) [67,68,70,105,138] beyond conventional Cartesian k-space imaging and other more specialized methods [71,139–142]. Among these, the combination of radial sampling with the GRAPPA technique has gained interest due to improved image quality due to new calibration schemes [67,68], which enable robust imaging even at acceleration factors ≥ 8 [68,101]. Furthermore, low-latency reconstructions with radial GRAPPA have been demonstrated [106,107,143], making true real-time imaging with real-time reconstruction possible.

As originally described, radial GRAPPA (rGRAPPA) requires at least one fully sampled calibration k-space acquired prior to accelerated imaging to compute the GRAPPA weights for every missing point in the undersampled k-space [67]. Refinements of the technique use multiple fully sampled frames making reconstruction more robust although the calibration time increases, extending scan time [68]. Several algorithms for radial GRAPPA without calibration have been proposed [144–147]. For example, computation of GRAPPA weights can be achieved by constructing synthetic fully sampled calibration data via multiplication with an image domain mask, which is generated either from coil sensitivity estimates from the densely-sampled k-space center [144], or from a post-processing algorithm that attenuates streaking [145]. Multiplication with an image domain mask is equivalent to a convolution of the undersampled k-space, which allows the estimation of a fully sampled calibration k-space. The reported image quality is good, however, residual streaking artifacts remain for acceleration factors > 4. Another method computes the GRAPPA weights directly from the undersampled data via interpolation of the relative shifts along the azimuthal direction [146]. Although this technique yields image quality comparable to that of radial GRAPPA with fully sampled calibration data, reconstructions from highly radially undersampled k-space (with <50 projections) have not been reported. This is likely due to the fact that the accuracy of the weights interpolation decreases with increasing distance between two adjacent projections, which could be problematic for real-time cardiac imaging where highly undersampled acquisitions are desired to maintain temporal resolution.

This work proposes an alternative self-calibration technique for radial GRAPPA to be utilized in highly accelerated imaging and suitable for true real-time implementation. The technique is validated in swine and human subjects, and reconstruction error, relative to a gold standard, are reported.

3.2 Theory

3.2.1 Radial GRAPPA Calibration

To speed up acquisition with GRAPPA sampling, only every 1 out of R adjacent phase encoding (PE) lines or projections is acquired, and the missing $R-1$ PE lines or projections are estimated from the acquired projections in the neighborhood. This estimation of missing spatial frequencies is made possible by exploiting the spatial variations of the coil sensitivities in multi-channel receiver arrays that represent a convolution kernel applied during acquisition in the Fourier domain.

For GRAPPA reconstruction, the kernel weight sets that describe the contribution of the source points (acquired data) to the target point (missing data) need to be defined [52]. By convention, a B_y x B_x kernel (or block) selects the B_x closest k-space points in the readout direction from the B_y lines closest to the target missing point as source points. The target point is estimated as a weighted combination of $N_B= B_y$ x B_x source points and this process is carried out for every missing k-point.

With Cartesian sampling, the relative geometry of the source points with respect to the target point in k-space are identical throughout the entire undersampled k-space. Hence, the acquisition of a fully sampled k-space provides many occurrences of the kernels to be used in weights set calculation, which requires solving a single linear system [52]. However, in azimuthally undersampled radial trajectories, the relative positions of the source points with respect to the target point vary over k-space, resulting in unique kernel geometry per missing point, and requiring solving as many separate linear systems for determination of per-point weight sets. Since the kernel geometries are unique, there exists only one kernel occurrence per each weight set to be calculated even if an entire k-space is fully sampled. In the original formulation of radial GRAPPA [67], this problem was dealt with by dividing the k-space into small segments spanning a number of projections ($N_{seg,proj}$) and readout points ($N_{seg,read}$) the size of the segment being N_{seg}= $N_{seg,read}$ x $N_{seg,proj}$. Each segment was treated as a Cartesian k-space with the assumption that kernel geometries for missing points were similar enough within the segment, and thus, a single set of weights was necessary for the estimation of all target points within the segment.

More recently, an alternative calibration involving a multiplicity of fully-sampled k-spaces was proposed [68]. With this through-time calibration, required information for determination of the kernel was obtained from multiple repetitions in time instead of occurrences over a segment. Calibration consisting of N_{frames_full} fully sampled frames provided multiple occurrences of the same exact kernel geometry for every target point. This approach drastically increased the accuracy of weight set calculation at the expense of increased calibration scan time.

By integrating both through-time calibration and through-k-space calibration to reduce N_{frames_full} [68], calibration duration is reduced, improving clinical applicability [101]. The combination of smaller k-space segments (e.g. N_{seg}=4x1), which better preserve kernel geometry assumptions, and through-time calibration allows weights to be computed from kernel occurrences that are more similar in geometry compared to those in the original through-k-space formulation, yielding more accurate reconstructions. This hybrid through-time/through-k-space calibration technique, referred to as simply through-time radial GRAPPA (TT-rGRAPPA) in this work, permits artifact-free high quality real-time imaging from highly undersampled radial data [68].

3.2.2 Self-Calibrated Radial GRAPPA

In through-k-space calibration, fully sampled k-space segments are utilized to obtain kernel observations, the geometries of individual kernels used to compute a distinct weights set are similar to one another but not identical. In this work, we also exploit the idea that weights computation can be accomplished using kernels with approximate geometries, yet we restrict the search for such kernels to the undersampled k-spaces of the actual accelerated scans. As a first step in accomplishing this goal, we reduce the GRAPPA kernel to a one-sided kernel by choosing to include the source points from only the acquired projection that is closer to the missing point. In other words, the number of source points as N_B=3x2 is reduced to N_B=3x1, which is referred to as "half-block" through-time radial GRAPPA (HB-TT-rGRAPPA) throughout this manuscript. Then, for any missing point in the k-space, the search for kernels with similar geometries is performed by sliding the N_B=3x1 source block point by point in the direction of the k-space center and checking whether the geometry is "similar" to original when this block is paired with a point, to serve as the target point, from another acquired projection, as shown in Figure 3.1c (red arrow). To be more specific, the measure of similarity between two kernels is the inverse difference of each kernel's distance between the midpoint of the source block and the target point. After the undersampled k-space is searched in this manner, the most similar $N_{similar}$ kernels are used to calibrate weights for the missing k-space point. Furthermore, the number of kernel occurrences is boosted via repetitions over time from multiple successive accelerated frames (N_{frames_acc}), similar to the through-time rGRAPPA calibration. Thus, the proposed rGRAPPA calibration method is called self-calibrated through-time radial GRAPPA (SC-TT-rGRAPPA). Figure 3.1 depicts the acquisition of the required training data for calibration directly from the undersampled data in detail.

To obtain kernel occurrences with better geometric similarity, one last modification is applied to radial GRAPPA as a variation in the k-space undersampling scheme. Considering a fully-sampled radial grid with N_{ϕ} projections, only $N_{\phi,acc}$=N_{ϕ}/R projections are acquired per time frame in the accelerated scan. The density of sampling is doubled by alternating azimuthal positions of the acquired projections by $\lfloor R/2 \rfloor$ in the fully sampled grid for every other frame. In other words, the angles of the projections differ by $\lfloor R/2 \rfloor \cdot (\pi/N_{\phi})$ in successive frames. Utilizing this alternating k-space trajectory results in roughly twice as many k-space samples to be used for weights calibration in SC-TT-rGRAPPA compared to the conventional acquisition scheme. Thus, kernel occurrences with better similarity and/or simply more occurrences with equivalent similarity can be obtained. The sequence modification is depicted in Figure 3.1, and will be referred to as “alternating k-space” throughout this work.

3.3 Methods

3.3.1 Data Acquisition

In vivo cardiac data were acquired under free breathing without ECG-gating from one healthy swine and normal human subjects (N=13). ACUC and IRB approval was obtained for all studies, as was informed consent. A modified bSSSP sequence with a metronome-like view ordering [68] to prevent eddy-current-induced artifacts was used as illustrated in Figure 3.1. Images were reconstructed with two distinct image matrix sizes at 128x128 and 192x192. The matrix size was determined by the number of samples in the readout, and double oversampling was employed in all scans with 256 or 384 samples per readout. For scans resulting in both image matrix sizes, a variety of settings for N_ϕ (number of projections in a fully sampled calibration scan) and R (acceleration factor) was used in data acquisition. Specifically, 128x128 images were produced from scans that used N_ϕ = [128, 144], and 192x192 images were produced from scans that used N_ϕ = [192, 216, 224, 256]. Throughout this manuscript, scans resulting in 128x128 and 192x192 images are referred to as *Standard Resolution* and *High Resolution,* respectively. Field-of-view (FoV) was held constant at 250 mm^2 for all experiments, yielding spatial resolutions of $1.95\text{x}1.95\text{mm}^2$ (*Standard Res*) and $1.30\text{x}1.30\text{mm}^2$ (*High Res*).

3.3.2 Animal Studies

For accurate estimation of GRAPPA weights that represent solely the interrelation of coils' sensitivity profiles with one another, motion during Through-time Radial GRAPPA calibration is necessary. Computing the weights from temporal replicas of the same image information inevitably copies information from this stationary image into the GRAPPA weights, biasing reconstruction towards the calibration image, and hence, no stationary phantom studies were carried out in this work. Instead, a comprehensive *in vivo* imaging study was performed on one healthy swine on a 1.5T scanner (Avanto, Siemens Medical Solutions, Erlangen, Germany). Standard chest (2x3=6) and spine (3x3=9) arrays yielding a total of N_C=15 receiver coils were used. Other scan parameters were: Slice thickness=7.0mm, flip angle=50°, Standard Res/High Res TR=2.8/3.2 ms, and TE=TR/2. The effect of various acquisition and reconstruction parameters on the performance of the proposed technique was measured. Gold-standard reference images were reconstructed with N_{frames_full}=400 fully sampled calibration frames using N_{seg}=1x1 (i.e. no through-k-space calibration) as in [34]. Three short-axis (SAX) slices and one horizontal long-axis (LAX) slice were imaged. Defining R_{cart}=$N_{PE}/N_{\phi,acc}$ as the acceleration rate w.r.t a fully sampled *Cartesian* scan, the following combinations of $[N_\phi; R; R_{cart}]$ were used in scanning. *Standard Res*: [N_ϕ=128; R=8; R_{cart}=8], [N_ϕ=144; R=6; R_{cart}=5.3], [N_ϕ=144; R=9; R_{cart}=8] and [N_ϕ=144; R=12; R_{cart}=10.7]. *High Res*: [N_ϕ=192; R=8; R_{cart}=8] and [N_ϕ=192; R=12; R_{cart}=12]. All accelerated scans were performed using both the conventional k-space and the alternating k-space (Fig. 3.1) trajectories.

To determine the effects of the self-calibration parameters, several different reconstructions were performed using a variety of $N_{similar}$ and N_{frames_acc} values for each scan. Specifically, $N_{similar}$ values were set to [1,2,4,6,8], and N_{frames_acc} was varied between 6 and 120. The evaluation criteria used was chosen to be the normalized root-mean-square-error (RMSE) with respect to the reference TT-rGRAPPA reconstructions (N_{seg}=1x1, N_{frames_full}=400). TT-rGRAPPA and HB-TT-rGRAPPA reconstructions with N_{seg}=4x1 (N_{frames_full} =80) and N_{seg}=16x4 (N_{frames_full}=6) were also included in the comparison of the images reconstructed by SC-TT-rGRAPPA. The RMSE values were then used to choose the optimal parameters for SC-TT-rGRAPPA.

3.3.3 Normal Human Subject Studies

The human subjects were divided into two sets. For first set of subjects (N=8), short-axis cardiac images were acquired on a 1.5T scanner (Avanto, Siemens Medical Solutions, Erlangen, Germany). Scan parameters were: N_C=15 (same coil configuration as in the animal studies), slice thickness=8.0mm, flip angle=45°, Standard Res/High Res TR=2.8/3.2 ms, and TE=TR/2. Imaging was performed using the same set of $[N_\phi; R; R_{cart}]$ combinations as in the swine study with the exception of $[N_\phi=128; R=8; R_{cart}=8]$. Only the alternating k-space trajectory was employed. For each subject, a stack of 12 adjacent slices were scanned in a sequential manner where each slice was imaged between 5 to 10 seconds to insure coverage through one complete respiratory cycle. In addition, for one mid-ventricular slice, calibration data with 400 fully sampled frames as in the swine study were acquired to enable gold-standard TT-rGRAPPA reconstructions and hence, computation of RMSEs in the SC-TT-rGRAPPA reconstructions.

The second set of normal subjects (N=5) was imaged at a 1.5T scanner (Aera, Siemens Medical Solutions, Erlangen, Germany) using combinations of standard chest and spine receiver arrays yielding a larger number of total coils (N_C=20-30), which permitted imaging at higher acceleration rates and resolution. Other scan parameters were: slice thickness=6.0mm, flip angle=70°, Standard Res/High Res TR=2.7/3.1 ms, and TE=TR/2. In addition to the $[N_\phi; R; R_{cart}]$ combinations utilized in the first set of human studies, combinations of $[N_\phi=216; R=12; R_{cart}=10.7]$, $[N_\phi=224; R=14; R_{cart}=12]$, $[N_\phi=256; R=16; R_{cart}=12]$ and $[N_\phi=192; R=16; R_{cart}=16]$ were also used for the *High Resolution* scans with 192x192 final image matrix. For each subject, one short-axis slice and one long-axis slice were imaged using the alternating k-space trajectory.

3.3.4 Image Reconstruction

All image reconstruction was carried out in MATLAB (MathWorks Inc., Natick, MA) and used non-uniform FFT [9,148] for gridding. For TT-rGRAPPA and HB-TT-rGRAPPA, GRAPPA weights were computed via the SVD-based pseudo-inverse (i.e. *pinv()*), whereas Tikhonov regularization with a constant Tikhonov λ per image depending on image resolution (1e-06 ≤ λ ≤ 6e-06]) was utilized in the calibration of the weights for SC-TT-rGRAPPA. The addition of regularization suppressed noise in the SC-TT-rGRAPPA calibration as further explained in the discussion, and helped improve image quality. SC-TT-rGRAPPA calibrations using N_{frames_acc} = [10, 20, 120] for [N_{ϕ}=144; R=9] and [N_{ϕ}=192; R=8] scans took [130, 148, 238] and [244, 263, 440] seconds on average on our dual-socket six-core Intel Xeon E5-2620 v2 at 2.10 GHz system, respectively. Furthermore, due to the alternating view ordering, residual image artifacts changed every other frame, which presented itself as a high-frequency flicker. Hence, a low-pass temporal filter the following parameters was applied: passband frequency=0.90 ϖ, stopband frequency=0.98 ϖ, allowed passband ripple=1 dB and stopband attenuation=60 dB.

3.4 Results

3.4.1 Animal Studies

Figure 3.2 shows example images from the swine heart in both end-systole and end-diastole acquired with the alternating k-space trajectory. Images reconstructed from all three methods using fully sampled calibration data look very similar to one another. “Half-block” through-time radial GRAPPA reconstructions are almost identical to those of the standard TT-rGRAPPA with less apparent grainy noise. This could be attributed to the fact that the linear system in the calibration for HB-TT-rGRAPPA weights is twice as over-determined as the one in TT-rGRAPPA. Using a larger segment size (i.e. N_{seg}=16x4) also does not result in a major difference expect some slight blurring in smaller structures such as the papillary muscles. On the right-most column, images reconstructed with the proposed SC-TT-rGRAPPA method are shown. N_{frames_acc} =100 was used, which corresponds to 4.4 and 7.7 seconds of real-time imaging for the standard and high resolution scans, respectively. The images reconstructed with the self-calibrated method are comparable to images from the other reconstructions. There is visible CNR degradation and some loss of structures near the periphery, but the heart is well visualized with good delineation of the myocardium.

3.4.1.1 Quantitative Analysis of Image Quality

Figure 3.3 shows plots of the RMSE values in the SC-TT-rGRAPPA reconstructions for each scan of the central short-axis slice acquired with the alternating trajectory from the swine experiment when different self-calibration parameters are used. As expected, RMSE decreases monotonically with the number of undersampled frames used in the weights calibration except for $N_{similar}$=8. Similarly, RMSE decreases as $N_{similar}$ increases with the exception at $N_{similar}$=8. For small values of N_{frames_acc} (<30), reconstructions with 8 similar kernels may outperform those with smaller $N_{similar}$ values since the weights calibration system will be only slightly overdetermined with fewer number of kernels, however, $N_{similar}$=8 does not yield the lowest RMSE for higher values of N_{frames_acc}. The unexpected behavior of the RMSE versus N_{frames_acc} when $N_{similar}$=8 is used may suggest that kernel geometries are not sufficiently similar to the original kernel geometry beyond the first 6 similar kernels that are obtained from the undersampled k-space. With an abundance of the frames used in calibration, $N_{similar}$=6 yields the optimal reconstructions with the lowest RMSE except for N_{ϕ}/R=144/6 where $N_{similar}$ values of 2,4 and 6 produce indistinguishable results. Hence, $N_{similar}$=6 is chosen as the optimal value for the SC-TT-rGRAPPA reconstructions in the results presented in the remainder of this manuscript.

Table 3.1 displays RMSEs of SC-TT-rGRAPPA reconstructions with $N_{similar}$=6 and N_{frames_acc}=120 as well as RMSEs of the standard TT-rGRAPPA and HB-TT-rGRAPPA reconstructions for scans in the swine experiment. RMSEs are averaged across slices with the standard deviations averaged in percentage relative their corresponding means prior to averaging. Switching from the regular to the alternating k-space trajectory, there is a noticeable decrease in RMSE for the self-calibrated reconstructions. RMSEs of SC-TT-rGRAPPA reconstructions further increase as the acceleration rate increases as expected. Moreover, RMSEs for N_{ϕ}=192 are higher than those for the standard base resolution for all reconstructions. Table 3.1 also illustrates the feasibility of the proposed half-block rGRAPPA method.

3.4.2 Healthy Volunteer Studies

Figure 3.4 shows short-axis images from a healthy subject in both end-systole and end-diastole for all of the accelerated scans acquired with the alternating trajectory. Images reconstructed with SC-TT-rGRAPPA are qualitatively comparable to those reconstructed with TT-rGRAPPA except a subtle loss in blood-to-myocardium contrast that is more visible at R=12. Figure 3.5 and Figure

3.6 show human images of 10 short-axis slices from base to apex at end-diastole and end-systole for N_ϕ/R=144/9 and N_ϕ/R=192/12 respectively. The image quality of SC-TT-rGRAPPA reconstructions is consistent across slices, with the CNR loss more apparent in the systolic frames. Figure 3.7 displays SC-TT-rGRAPPA reconstructions from human data acquired with N_ϕ/R=144/9 and N_ϕ/R=192/12 where every other frame from a complete cardiac cycle is shown for each. While the N_ϕ/R=192/12 reconstruction appears to have noticeably degraded image quality compared to N_ϕ/R=144/9, the increase in RMSE is not excessive. Figure 3.8 shows end-diastolic images from a healthy subject imaged with a larger array of receiver coils and under greater acceleration factors ($R \geq 12$). Using larger receiver arrays permit acceleration factors as high as R=16 for the standard TT-rGRAPPA technique. Although there is visible loss of SNR and slight residual streaking, SC-TT-rGRAPPA reconstructions at these acceleration rates are still feasible.

3.5 Discussion and Conclusion

3.5.1 Comparison to Standard Radial GRAPPA

The images reconstructed with the proposed self-calibrated radial GRAPPA method presented in this work demonstrate the feasibility of real-time free breathing cardiac imaging without the need for separate training data. In the self-calibrated reconstructions from the animal scans, the mean RMSE averaged over 4 slices had a maximum of 5.60% with respect to the gold standard TT-rGRAPPA reconstructions. The images reconstructed with the proposed self-calibrated method do exhibit discrepancies when visually compared to their TT-rGRAPPA counterparts, yet image quality is preserved for most CMR applications. The difference in reconstruction quality is more distinguishable in the short-axis slice from the swine study. This may be due to the greater dynamic range of signal intensity and/or the effect of the coil configuration in that orientation. Figure 3.4 demonstrates the successful visualization of the myocardium with SC-TT-rGRAPPA for various acceleration rates. At R=12, blood-myocardium contrast is decreased yet should still be adequate for delineation of the endocardial border. The papillary muscles in the left ventricle are also reconstructed with good definition.

The data in Figure 3.3 suggests that $N_{similar}$=6 is the optimal number of similar kernels for the extent of this study, and with a N_B=3x1 kernel, 100 accelerated frames are sufficient for accurate weight estimation in SC-TT-rGRAPPA. For a temporal footprint per image of ~44 msec, this corresponds to <5 sec per slice. For higher resolution imaging, a maximum of 8 sec per slice is needed. Assuming that the left ventricle can be covered with 12 slices, a function study could be completed in one to two minutes depending on desired resolution and without any gating or breath-holding. Since real-time scans usually span at least one complete respiratory cycle to ensure acquisition of an end-expiration beat, this is close to the minimum scan duration. Though further studies are needed to determine the clinical utility of this technique, this is an exciting scenario that could lead to the widespread usage of SC-TT-rGRAPPA in situations in which breath-holding is not feasible. Figures 3.5 and 3.6 illustrate the feasibility of such time-efficient whole heart imaging with multiple short-axis slices from base to apex reconstructed with both TT-rGRAPPA and SC-TT-rGRAPPA. SC-TT-rGRAPPA-reconstructed images appear noisier compared to the TT-rGRAPPA reconstructions, however image quality is consistent across all slices.

Based on the RMSEs shown in Table 3.1, it can be argued that SC-TT-rGRAPPA is sub-optimal to TT-rGRAPPA even when few fully sampled calibration frames are used with a larger segment size (i.e. N_{seg}=16x4, N_{frames_full}=6), and thus, it may not provide value and clinical utility over TT-rGRAPPA. However, it is important to bear in mind that there is no real ground truth when computing the RMSEs as we are simply restricted to a subjective gold standard in the form of TT-rGRAPPA reconstructions using N_{seg}=1x1 and N_{frames_full} =400. The RMSE-based comparison between SC-TT-rGRAPPA and the standard TT-rGRAPPA is therefore biased towards TT-rGRAPPA (with N_{seg}=16x4 and N_{frames_full}=6) since the RMSEs for TT-rGRAPPA is computed with respect to a reconstruction of the same type with the only discrepancy being the larger segment size. Moreover, even though TT-rGRAPPA with N_{seg}=16x4 may require a calibration scan of only 2-4 seconds, it is still considerably disruptive given that it needs to be repeated for any change in slice position or orientation during imaging.

3.5.2 Image Quality versus Acceleration Factor

The results presented in this work suggest that the acceleration rate (R) is a major factor that hinders the performance of SC-TT-rGRAPPA as in any other parallel imaging technique. Table 3.1 shows the systematic increase in RMSE as R increases for both standard and high resolution scans. This is expected since as R increases, the undersampled k-space from which kernels with similar geometry are obtained gets sparser, and thus, the assumption that the geometries of the kernels from which weights are calculated are similar enough to the ideal geometry starts to break down. Considering the reconstructions from scans using the alternating trajectory, the steepest increase in RMSE is at the jump from R=6 to R=9, which is consistent with our observations that SC-TT-rGRAPPA on 6-fold undersampled data yield images not easily distinguishable from their TT-rGRAPPA counterparts whereas the images reconstructed by the two methods appear visibly different for acceleration rates of $R \geq 8$. Also, even though the increase in RMSE from R=9 to R=12 may not seem significant with a mean of 0.32 %, the reference images for R=12 are already inferior to those of R=9 in overall image quality, and thus, the self-calibrated reconstructions at higher accelerations rates may appear with poorer quality than expected.

3.5.3 Technical Considerations

Due to the alternating view ordering, residual image artifacts changed every other frame, which presented itself as a high-frequency flicker. A low-pass filter successfully removed these artifacts. Though this may have lead to a loss of very high frequency cardiac dynamics, its effect on diagnostic quality of imaging was minimal [24]. For example, an accelerated scan with image sampling rate of 23Hz (44ms/frame) can capture about 10 frequency harmonics on a subject with heart rate of 70 bpm, and the low-pass filter used here would reduce that to 9 harmonics. Setser *et al.* [24] showed that decreasing the captured harmonics from 10 to 8 only yields less than 2% and 3% deviation in the computations of left ventricular volume and ejection fraction, respectively. The temporal filter used in this work would lead to smaller deviation in these metrics. The design of a low-pass filter with a higher passband to allow more frequency harmonics can also be considered.

The source and target data points used in any GRAPPA calibration process are assumed to represent samples of k-space of the same object. For standard TT-rGRAPPA, this data is acquired within a narrow temporal window spanning less than one undersampled frame. However, the data used for calibration in SC-TT-rGRAPPA has a broader temporal window, since two contiguous undersampled frames are combined into a single k-space when alternating trajectory is utilized. The source-target pairing includes points that are acquired more than one image apart, permitting more motion with possible deterioration of the estimation process. More specifically, in TT-rGRAPPA, the sampling times of the source points and the target point within the same kernel vary roughly between TR and $(R\text{-}1) \cdot$ TR, where TR is the time it takes to acquire one projection. On the other hand, this time difference can be as great as $2 \cdot N_{\phi,acc} \cdot$ TR for SC-TT-rGRAPPA calibration. This discrepancy may be in part responsible for the increased RMSEs observed between the two techniques.

In standard TT-rGRAPPA, GRAPPA weights are computed using MATLAB's implementation of the SVD-based pseudo-inverse (i.e. *pinv()*). When GRAPPA weights were computed similarly using *pinv()* for SC-TT-rGRAPPA, the reconstructed images appeared noisier than images reconstructed with the standard approach. Investigation of the condition numbers of each reconstruction, an indicator for inversion stability and noise amplification, revealed that the condition numbers for the SC-approach were indeed higher than for standard TT-rGRAPPA, and markedly so for higher acceleration rates. To ameliorate these effects, which were more apparent at higher acceleration rates, Tikhonov regularization was incorporated into the reconstruction at the expense of contrast and blurring. However, the determination of the factors leading to noise enhancement as well as optimizing the choice of Tikhonov λ are subjects of further research. Also, due to the radially decreasing SNR, it may prove to be beneficial to parametrize λ as a function of radial position to achieve a more optimal regularization.

Having a higher number of coils for reconstruction increased maximum achievable acceleration rate, further improving temporal resolution as observed in the two subsets of normal subjects. However, the addition of coils increases the number of weights to be determined, and can increase the number of undersampled frames required to achieve a sufficiently overdetermined system for accurate estimation of weights. Nevertheless, to achieve aggressive acceleration rates $R \geq 12$, more coils were advantageous and necessary.

3.5.4 Half-Block Radial GRAPPA

Aside from a novel self-calibration method for radial GRAPPA, this work also introduces an alternative for the standard through-time radial GRAPPA, namely, half-block through-time radial GRAPPA as depicted in Figure 3.1. HB-TT-rGRAPPA utilizes only one acquired projection to reconstruct the nearest missing projections in its neighborhood whereas rGRAPPA and TT-rGRAPPA use the acquired projections on either side. Note that as the undersampling factor grows, the angular spread between acquired projections in the accelerated scan increases. Thus, when standard radial GRAPPA is employed, missing projections are primarily closer to one of the two acquired projections, the source points on the further projection are relatively far from the target points and may not yield significant contribution in the estimation process. Therefore, the discrepancies between the images reconstructed with standard radial GRAPPA and half-block radial GRAPPA are small with only 0.19% increase in RMSE, on average (Table 3.1). Since the size of the weights set is reduced in half, HB-TT-GRAPPA is less prone to overfitting when the least-squares problem is not sufficiently overdetermined. The feasibility of half-block radial GRAPPA is demonstrated by comparison to standard radial GRAPPA in Figure 3.2. Also, HB-TT-rGRAPPA and standard TT-rGRAPPA exhibit indistinguishable RMSE values and images at higher resolutions. Hence, for these scans the half-block approach could be used to reduce the pre-calibration scan duration if necessary. HB-TT-rGRAPPA may also benefit from larger kernels (e.g. N_B=5x1) to increase reconstruction accuracy though that also remains a subject for future work.

3.5.5 Extensions and Future Work

The herein-proposed self-calibrated radial GRAPPA method has potential to be translated into clinic with a real-time reconstruction implementation as similarly demonstrated for the standard through-time rGRAPPA [107]. Since the weights calibration and image reconstruction can be decoupled and made asynchronous in a parallelized framework [107,143], real-time display of images can start rapidly. Figure 3.3 shows that with $N_{similar}$=6 and 10 undersampled frames (~330-660 ms for *Standard Res.*), images with decent quality can be reconstructed, and with more time to obtain ~100-120 undersampled frames, well within the duration of one respiratory cycle, for the more accurate weights calibration, image quality would progressively improve. As a final consideration, the proposed approach for calibration can be directly extended to the 3-dimensional through-time radial GRAPPA technique [78,149], which could make 3D real-time procedure guidance feasible.

3.5.6 Conclusion

The self-calibrated through-time radial GRAPPA technique presented in this work demonstrates the feasibility of image reconstructions from aggressively undersampled radial data in the specific application of free breathing non-gated cardiac imaging without the need for additional calibration data. Employing undersampling factors ranging from 6 to 16, real-time cardiac images with frame rates as high as 30 (33 ms/image) and 26 (38 ms/image), at spatial resolutions of 1.95 mm^2 and 1.30 mm^2 respectively, are demonstrated without using additional scan time for calibration. The proposed self-calibrated radial GRAPPA method may be applicable in other real-time imaging scenarios where a separate calibration scan is not an option.

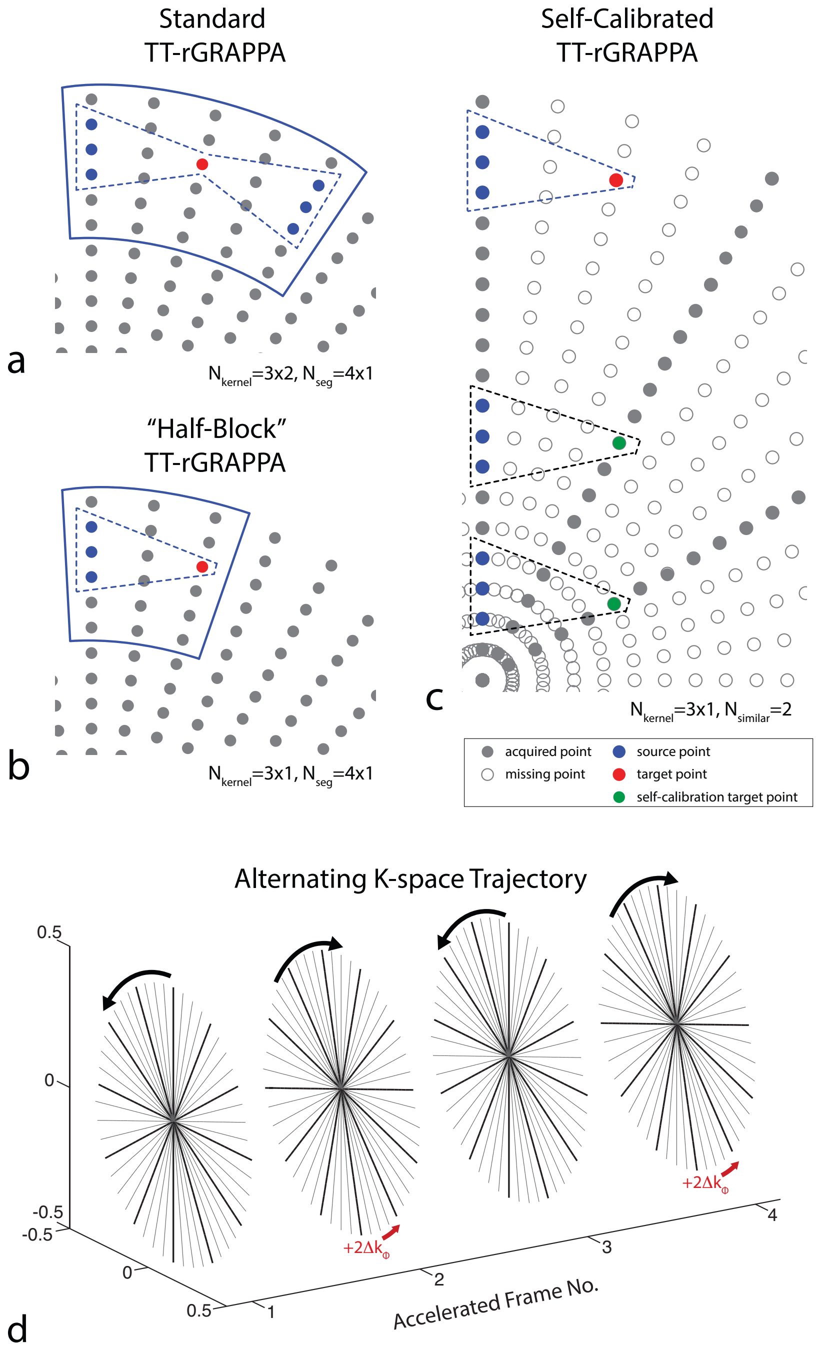

Figure 3.1. Depiction of the through-k-space portion of various radial GRAPPA calibration methods. Dashed boxes contain GRAPPA kernels with source (blue) and target points (red). The solid blue lines in a and b show segment size for calibration. The acquisition of training data directly from the undersampled k-space for self-calibration is depicted in c as 2 kernels towards the k-space center (with green target points) are used kernel replicates to calibrate the weights for the actual kernel (with red target point). The modified “alternating k-space” acquisition is shown in d for a *R*=4 accelerated scan. The azimuthal positions of the acquired projections are increased by $\lfloor \boldsymbol{R/2} \rfloor \cdot \Delta k_\phi$ (red arrows) every other frame where Δk_ϕ is the azimuthal angle between consecutive projections in the fully sampled k-space. The metronome-like view ordering to avoid eddy current effects is also depicted (black arrows).

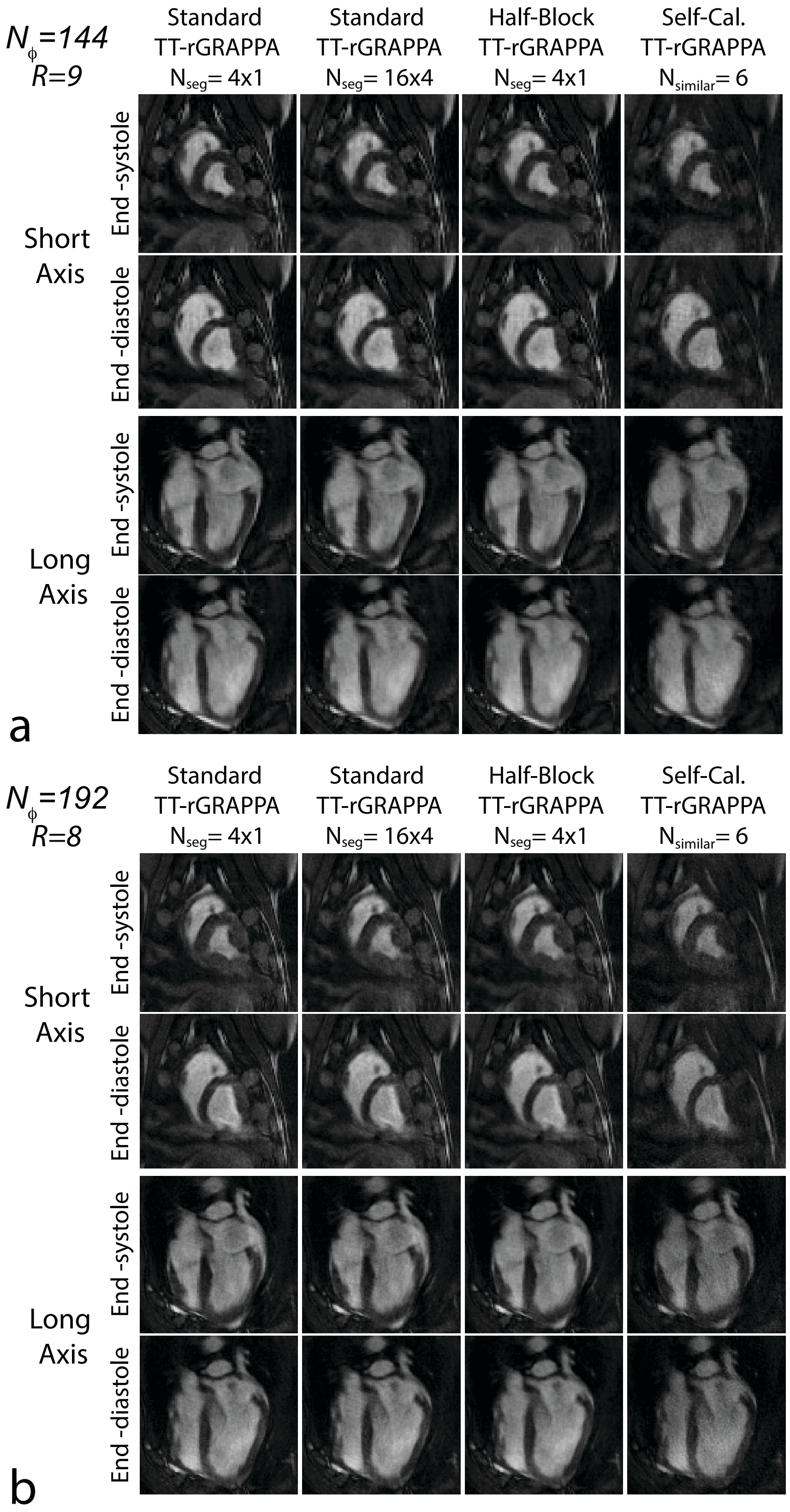

Figure 3.2. **a**: Example images from a normal swine reconstructed from 9-fold undersampled data (N_ϕ=144, $N_{\phi,acc}$=16) with a spatial resolution of 1.95x1.95 mm^2 and a temporal resolution of 44.3 ms/frame. For SC-tt-rGRAPPA, a total of 100 undersampled frames (~4.4 sec) and $N_{similar}$ = 6 were used in calibration. **b**: Same as in (a) except data was 8-fold undersampled (N_ϕ=192, $N_{\phi,acc}$=24) with a spatial resolution of 1.30x1.30 mm^2 and a temporal resolution of 77.5 ms/frame. Alternating trajectory was used in both scans.

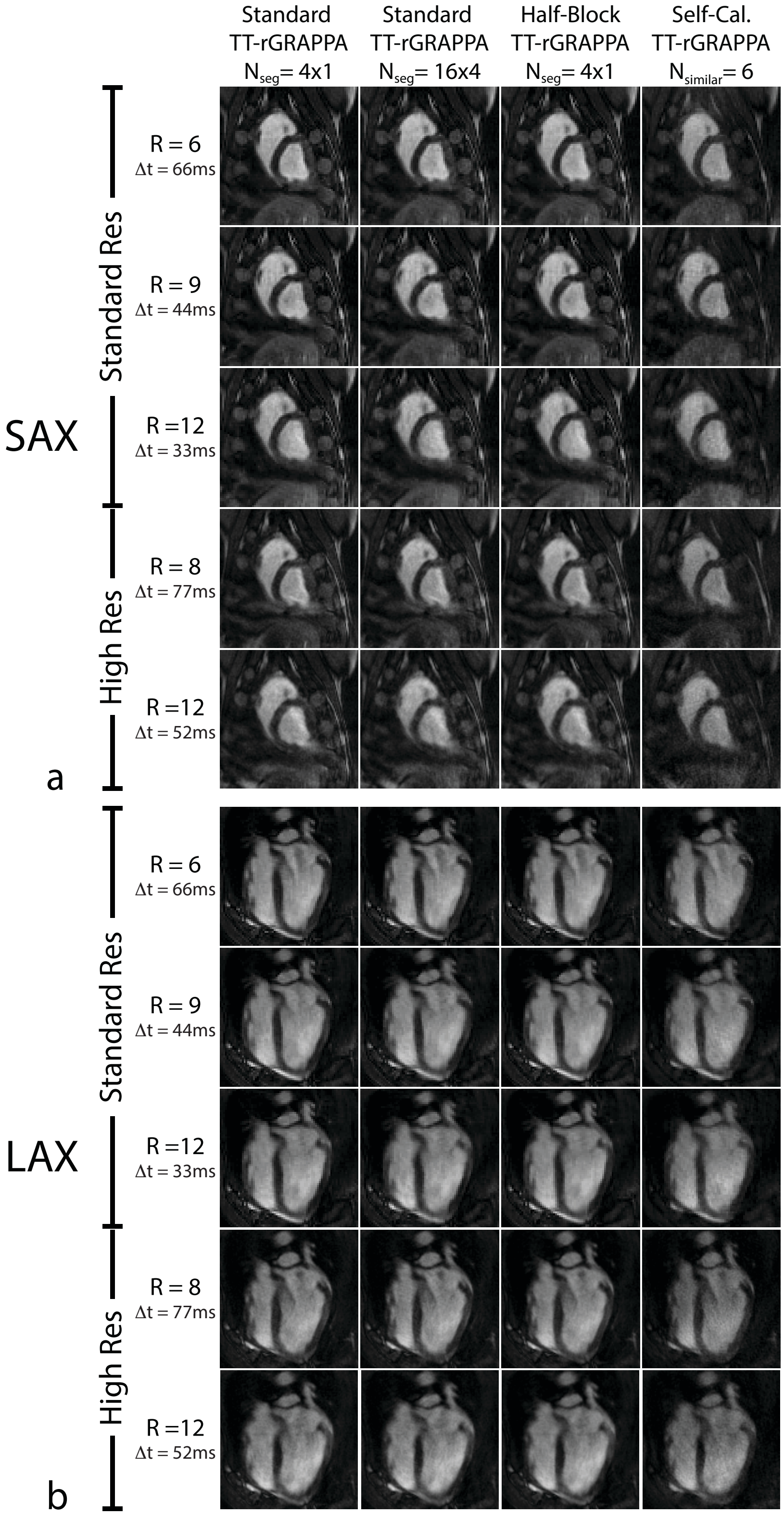

Figure 3.3. **a:** Example end-diastolic images of a short-axis slice from a normal swine. Reconstructed images from data with various undersampling factors are shown. For self-calibrated TT-rGRAPPA, 100 total undersampled frames and $N_{similar} = 6$ were used in weights calibration. Δt denotes the temporal footprint of the images. **b:** End-diastolic images of a long-axis slice from the same swine acquired and reconstructed in the same manner as in (a). Alternating k-space was employed in all scans.

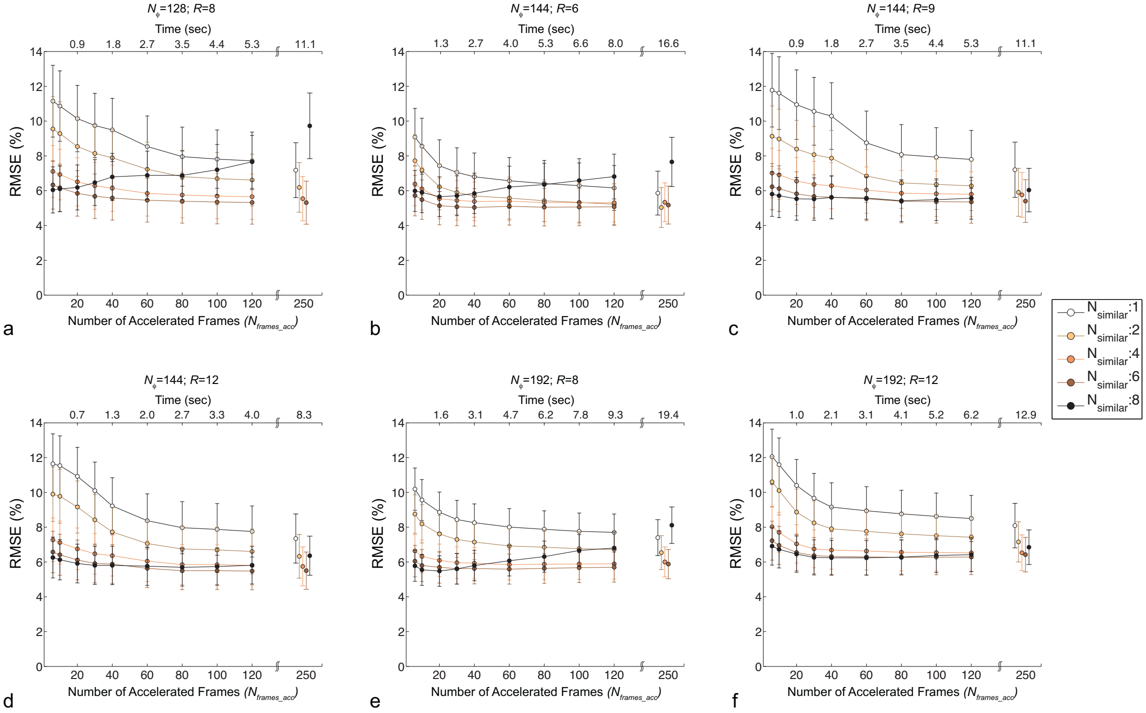

Figure 3.4. RMSE values of self-calibrated radial GRAPPA reconstructions of data acquired from a short-axis slice through a swine heart. Six different accelerated scans of varying resolution and acceleration rate (R) are shown. All acquisitions used the alternating k-space view ordering. RMSEs are plotted with respect to the number of accelerated frames used in calibration (N_{frames_acc}) with different colors of lines corresponding to various $N_{similar}$ values. Top horizontal axes indicate the lengths of the accelerated scans used in weights calibration in seconds. $N_{similar}$=6 yielded the results with the lowest error. Greater values of $N_{similar}$ lead to overfitting resulting in error that increased as more accelerated frames were used in calibration.

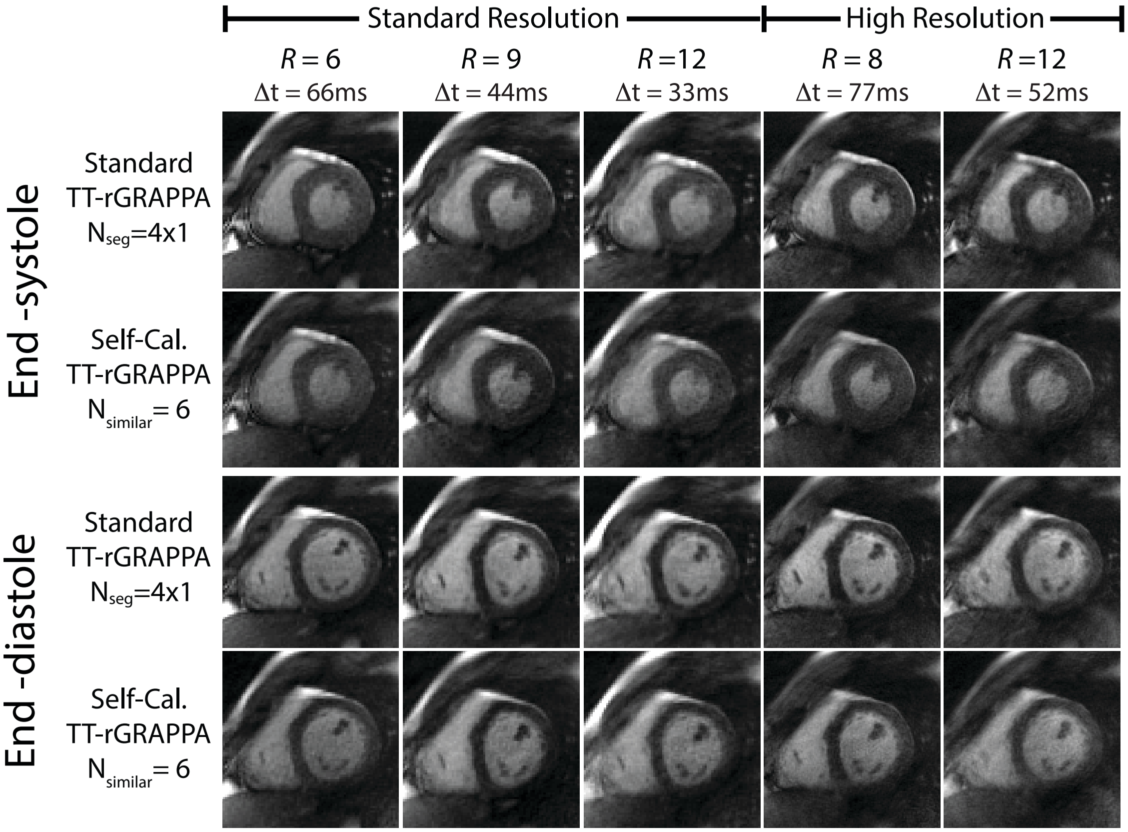

Figure 3.5. Example images from a human short-axis slice reconstructed with both standard TT-rGRAPPA and self-calibrated TT-rGRAPPA (SC-TT-rGRAPPA) are displayed. Images from data with various undersampling factors are shown. For SC-TT-rGRAPPA, 180 total undersampled frames and $N_{similar} = 6$ were used in weights calibration. Δt denotes the temporal footprint of the images. Alternating k-space was employed in all scans.

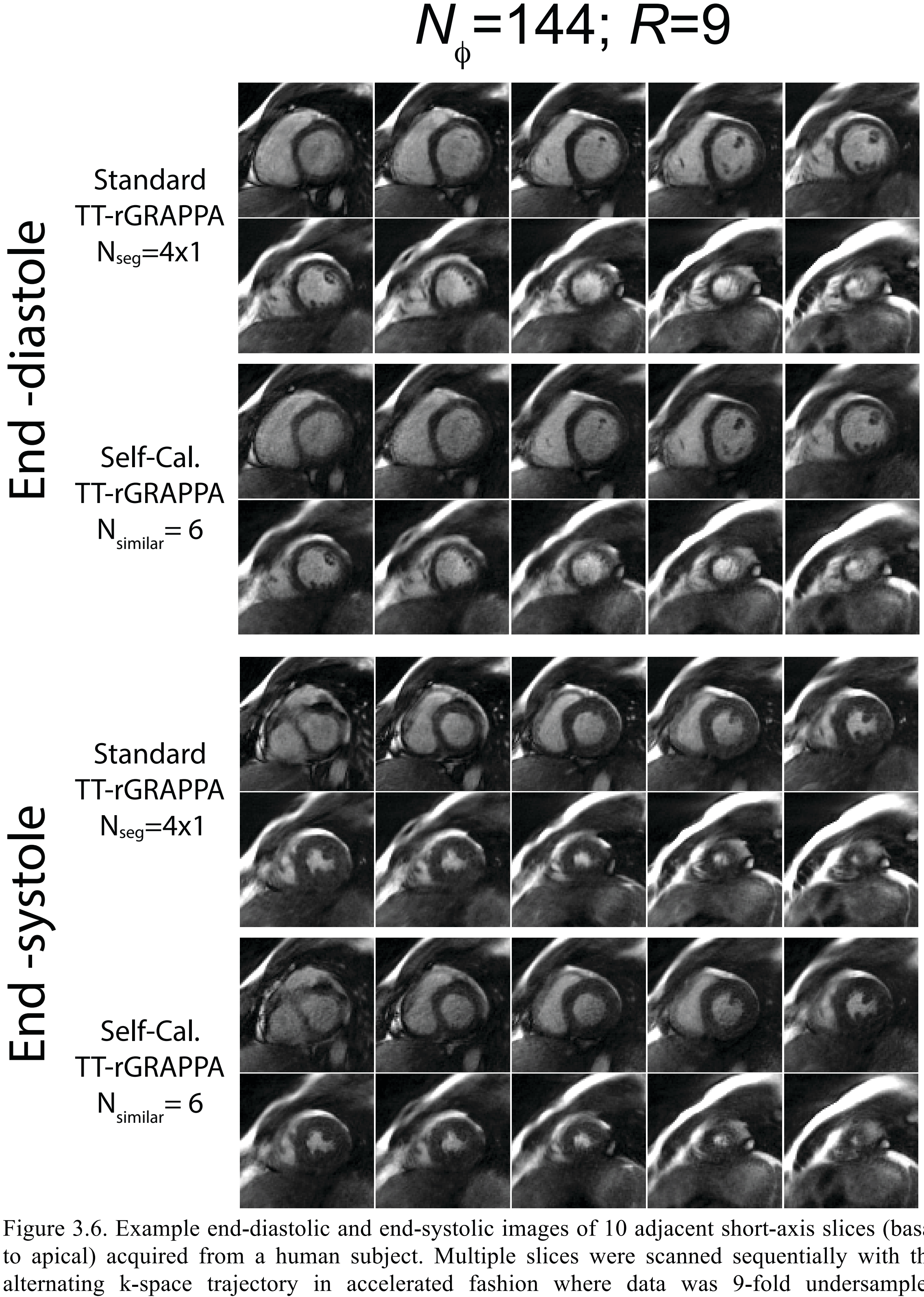

Figure 3.6. Example end-diastolic and end-systolic images of 10 adjacent short-axis slices (basal to apical) acquired from a human subject. Multiple slices were scanned sequentially with the alternating k-space trajectory in accelerated fashion where data was 9-fold undersampled (N_{ϕ}=144, $N_{\phi,acc}$=16) yielding a spatial resolution of 1.95x1.95 mm^2 and a temporal resolution of 44.3 ms/frame. Images were reconstructed with both standard TT-rGRAPPA and self-calibrated TT-rGRAPPA.

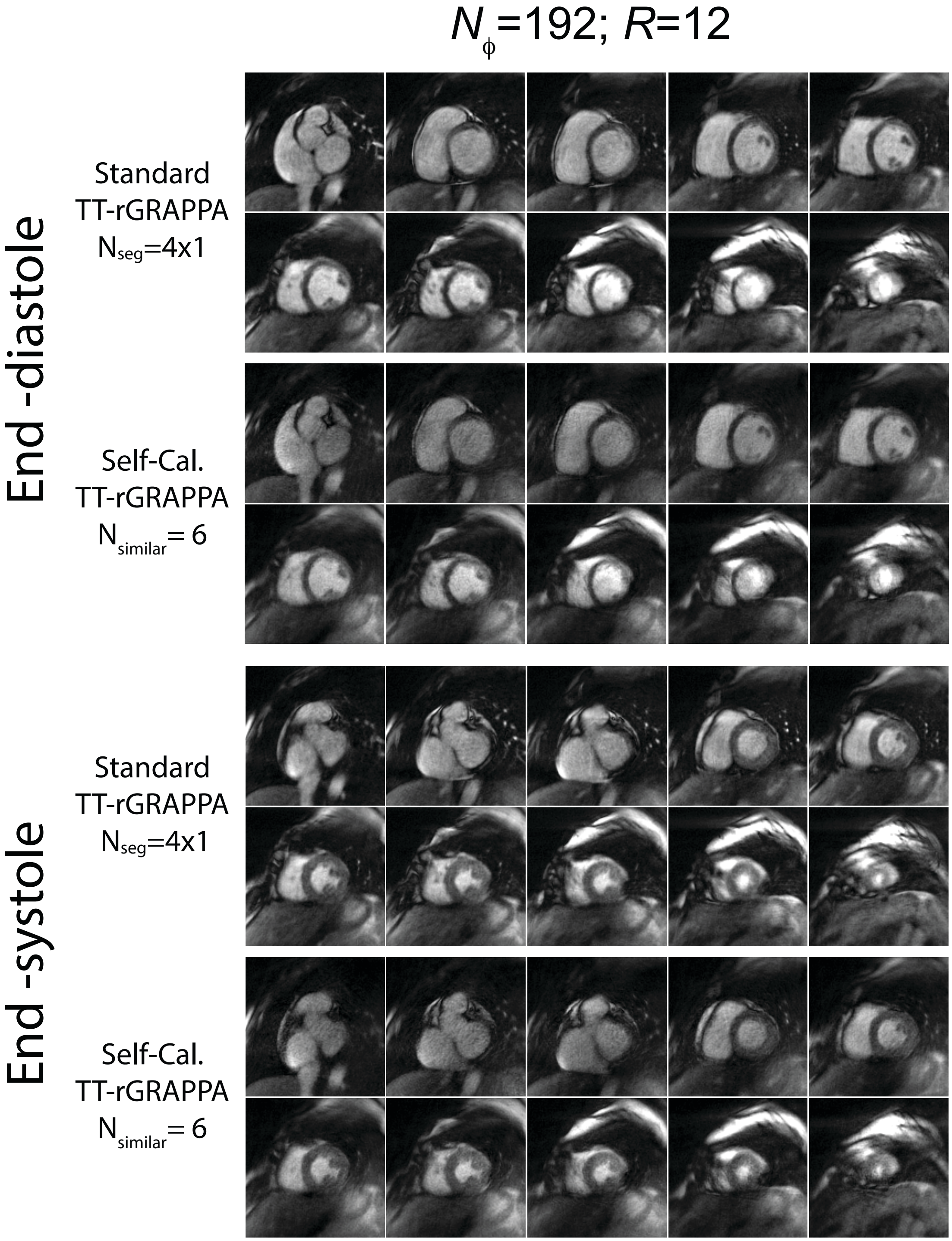

Figure 3.7. Example end-diastolic and end-systolic images of 10 adjacent short-axis slices (basal to apical) acquired from a human subject. Multiple slices were scanned sequentially with the alternating k-space trajectory in accelerated fashion where data was 12-fold undersampled (N_ϕ=192, $N_{\phi,acc}$=16) yielding a spatial resolution of 1.30x1.30 mm^2 and a temporal resolution of 51.7 ms/frame. Images were reconstructed with both standard TT-rGRAPPA and self-calibrated TT-rGRAPPA.

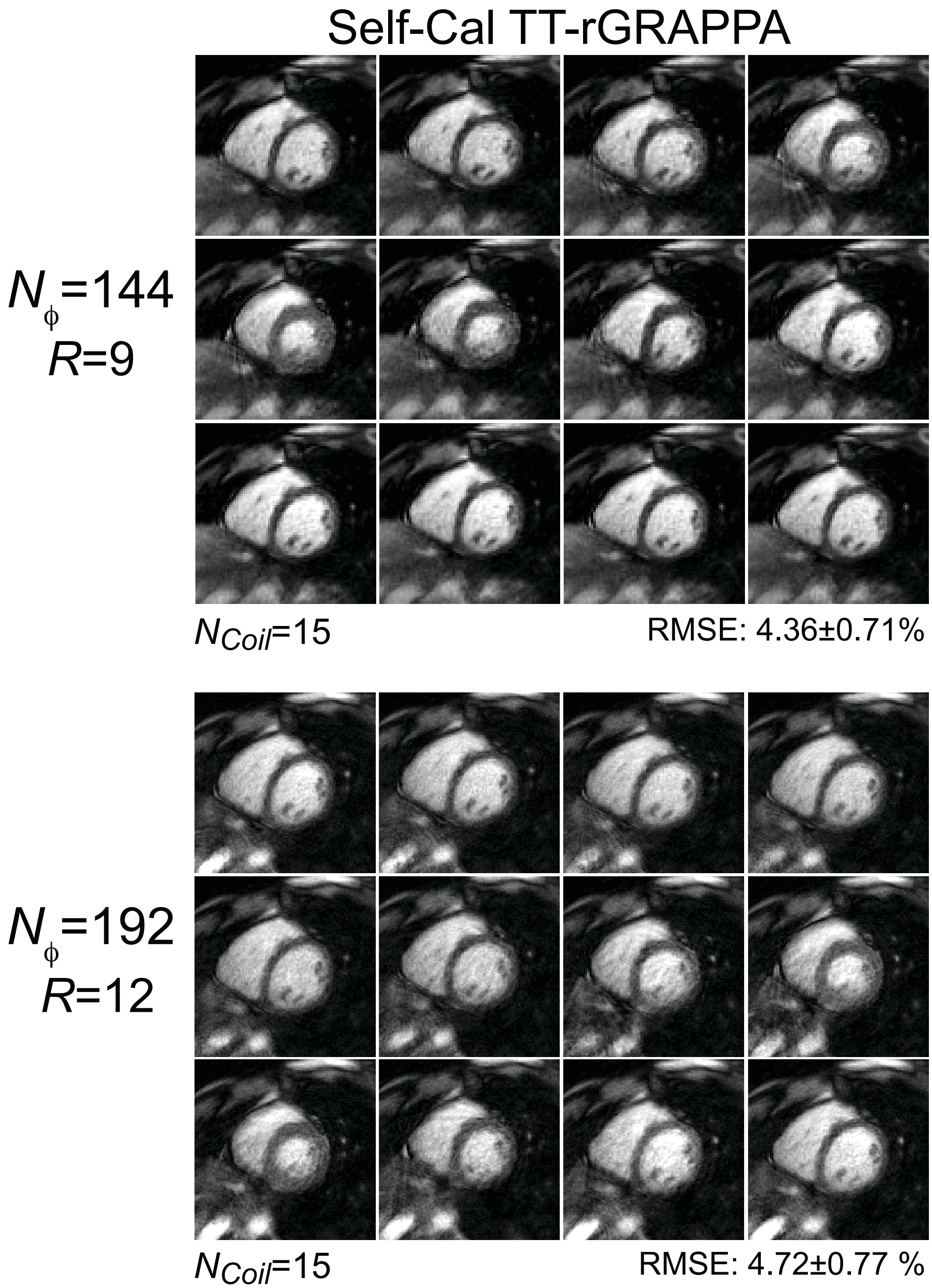

Figure 3.8. Example images from a human short-axis slice reconstructed with the proposed self-calibrated through-time radial GRAPPA (SC-TT-rGRAPPA) method using $N_{similar}$ = 6 and N_{frames_acc} = 180. Image series where every other frame from successive frames over one cardiac cycle are displayed. RMSEs of images reconstructed with SC-TT-rGRAPPA are computed w.r.t the gold-standard through-time radial GRAPPA reconstructions with N_{seg} = 1x1 and N_{frames_full} = 400. Alternating k-space was employed in both scans.

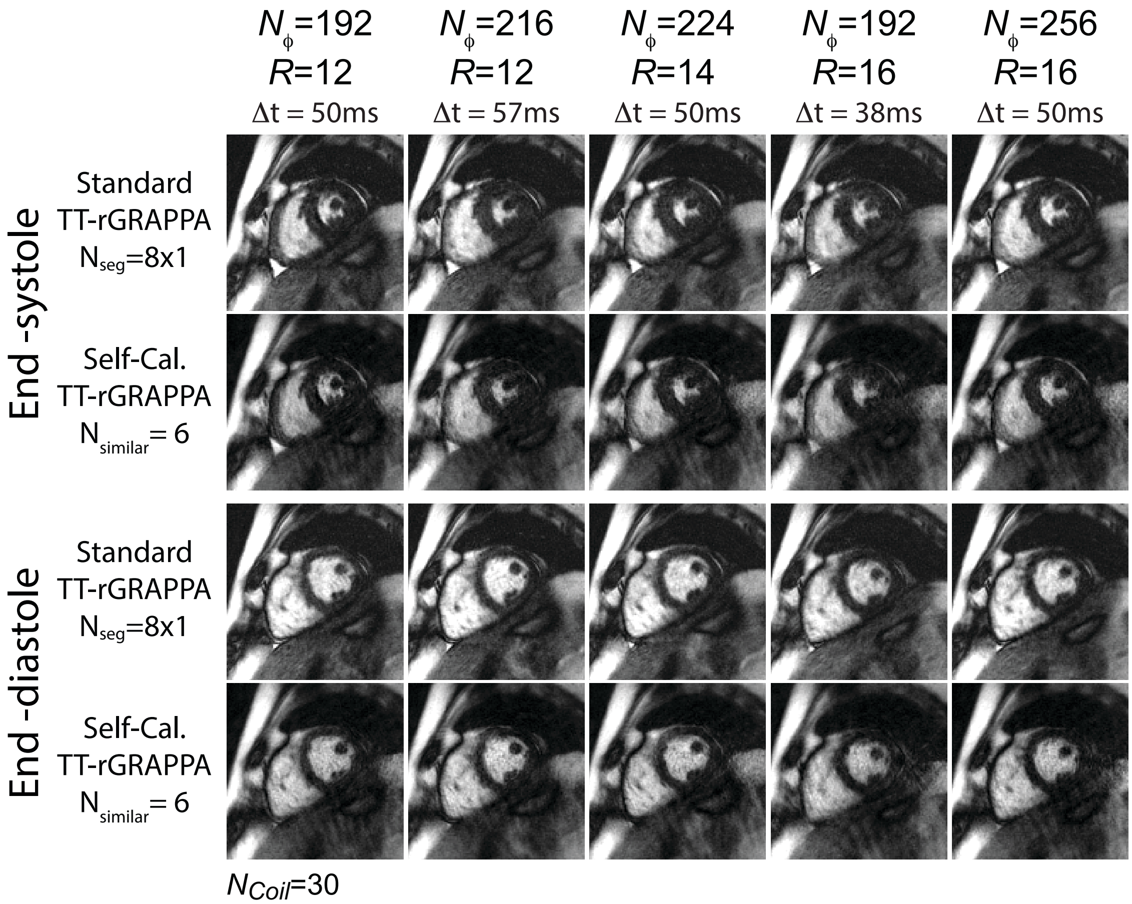

Figure 3.9. Example end-systolic and end-diastolic images from a short-axis slice of a healthy human subject reconstructed with both standard TT-rGRAPPA and self-calibrated TT-rGRAPPA are displayed. Images from accelerated scans with various undersampling factors ($R \geq 12$) are shown. Δt denotes the temporal footprint of the images. Alternating k-space trajectory was employed in all scans.

		Standard TT-rGRAPPA		**Half-Block TT-rGRAPPA**	**Self Calib. TT-rGRAPPA**	
N_ϕ (spat. res.)	Accel. Rate R	N_{seg}=4x1 N_B=3x2 N_{frames_full}=80 (μ±σ, %)	N_{seg}=16x4 N_B=3x2 N_{frames_full} =6 (μ±σ, %)	N_{seg}=4x1 N_B=3x1 N_{frames_full} =80 (μ±σ, %)	$N_{similar}$=6 N_B=3x1 N_{frames_acc} =120 (μ±σ, %)	Pulse Sequence
128 (1.95x1.95mm^2)	8	1.30±0.11	2.19±0.23	1.68±0.24	5.70±0.70	Reg
		1.23±0.29	2.02±0.36	1.52±0.64	5.19±0.92	Alt
144 (1.95x1.95mm^2)	6	1.01±0.27	1.65±0.34	1.21±0.48	7.16±1.15	Reg
		0.94±0.26	1.50±0.29	1.07±0.25	4.55±0.84	Alt
	9	1.24±0.24	2.13±0.34	1.52±0.46	8.69±1.25	Reg
		1.21±0.31	2.02±0.37	1.39±0.31	5.06±0.89	Alt
	12	1.55±0.11	2.68±0.23	1.93±0.32	9.73±0.96	Reg
		1.43±0.29	2.44±0.35	1.70±0.30	5.38±0.90	Alt
192 (1.3x1.3mm^2)	8	1.66±0.13	2.15±0.17	1.68±0.32	7.02±0.73	Reg
		1.68±0.21	2.14±0.23	1.65±0.20	5.25±0.68	Alt
	12	2.11±0.18	2.85±0.22	2.23±0.36	9.02±0.90	Reg
		2.04±0.34	2.72±0.37	2.06±0.33	5.65±0.81	Alt

rGRAPPA: radial GRAPPA; TT: Through-Time; Reg: Regular radial acquisition; Alt: Alternating k-space radial trajectory sequence;

Table 3.1. Comparison of RMSEs obtained after reconstructing for diverse resolution and acceleration factors tested on the normal swine. Data shown for Self-calibrated rGRAPPA reflects N_{frames_acc} =120. All values are relative to gold standard rGRAPPA calibrated with N_{frames_fs}=400 and N_{seg}=1x1.

4 REAL-TIME FREE-BREATHING CARDIAC IMAGING WITH SELF-CALIBRATED RADIAL GRAPPA AND A GOLDEN-ANGLE VIEW ORDER

4.1 Introduction

The use of magnetic resonance imaging (MRI) as a tool to evaluate cardiac motion and myopathy has been an integral part of clinical procedures over the past few decades, and one of the more established uses of cardiac MRI is the measurement of cardiac function. Segmented cine imaging [29] is the conventional choice of method to this end; however, it is traditionally performed with ECG-gating during breath-hold. Much work aims at removing the need for breath holding, using of respiratory bellows, motion correction methods [42,43] and self-navigation [132] among many other techniques. Similarly, the need for ECG gating has been addressed with self-gated cine techniques with retrospective reconstruction [133]. Nevertheless, segmented ECG-gated breath-held cine imaging has continued to be the standard clinical approach.

Real-time MRI has is immune to cardiac or respiratory motion artifacts, and thus is feasible during cardiac arrhythmia and/or irregular breathing patterns. However, since real-time acquisitions require images to be reconstructed from very narrow temporal snapshots of data, k-space must be aggressively undersampled when imaging at clinically desired spatial resolution. For example, a target temporal footprint of about 50 msec limits the number of readouts that can be used to reconstruct an image frame to no more than 20 when a typical balanced steady-state free-precession (bSSFP) readout of TR≈2.5 msec is employed, and the high acceleration rate (R) has been the major obstacle against the adoption of the technique.

Various acceleration techniques have been explored in the context of real-time cardiac MRI. Standard parallel magnetic resonance imaging (pMRI) methods that utilize Cartesian k-space coverage such as SENSE or GRAPPA generally fail to achieve artifact-free images with sufficient spatial and temporal resolution, and thus, are not suitable for real-time cardiac function imaging. On the other hand, undersampling with non-Cartesian k-space trajectories, yield less coherent aliasing artifacts that are more tolerable. They are also more favorable for accelerated imaging because typical non-Cartesian trajectories oversample the SNR-rich center of k-space, even under high rates of undersampling. To leverage such properties of non-Cartesian k-space coverage, extensions of SENSE [66] and GRAPPA [67,105] that accommodate non-Cartesian sampling have been proposed for real-time MRI. Among these, radial GRAPPA equipped with an improved GRAPPA weights calibration scheme [68] has gained particular interest due to the robustness of the image quality it offers under acceleration factors ≥ 8.

Apart from parallel imaging, sparsity-driven techniques, such as compressed sensing (CS) [55], have been shown effective in reconstructing highly undersampled MRI data, and naturally have been applied to cardiac MRI individually and in combination with parallel imaging methods [82,93,94,150] to achieve the higher acceleration rates. Similarly, techniques that exploit spatio-temporal correlations, which require the implicit assumption of temporal sparsity, have also reported high acceleration factors for real-time cardiac MRI [58,136]. Though these techniques demonstrate high image quality, the assumption of temporal sparsity inevitably hinders their utility for certain applications where that assumption may not hold (e.g. cardiac arrhythmias). This assumption also weakens the real-time nature of these methods since a reconstructed image frame still depends on the acquired data for previous and even future frames that may be used as part of the overall process as an effort to enforce sparsity in the temporal dimension.

The temporal resolution, measured by the width of the time window of time during which all of the data is acquired to generate an image, is an important parameter for real-time MRI. Typically, temporal resolution is fixed and based on the number of lines of k-space acquired per Cartesian or non-Cartesian image. For radial sampling, a novel view ordering employing a golden-ratio-based increment per each new radial spoke was proposed to facilitate flexibility ins choosing the temporal footprint of an image [97]. With this view ordering scheme, the azimuthal angle is incremented by ~111.25° for each new projection in a continuous manner, which ensures roughly uniform coverage of k-space for any arbitrary sequence of consecutive radial spokes.

Hence, with golden angle the temporal window (i.e. TR times the number of radial lines or spokes) can be chosen completely arbitrarily as desired.

Given such advantages, golden angle radial imaging can be highly useful in a real-time MRI setting, and though there have been multiple studies in accelerated MRI using the golden angle view ordering, these methods have not yet been translated to the clinic for real-time cardiac MRI applications. Techniques that leverage spatiotemporal sparsity (i.e CS) and multi-coil correlations (i.e. parallel imaging) combined with golden-angle radial acquisition [96,151] have reported 2D cardiac images with diagnostic image quality and temporal resolution. However, as discussed earlier, the dependence on temporal sparsity necessitates the acquisition of data from multiple cardiac phases and respiratory cycles, limiting the flexibility gained via golden angle real-time imaging. There are other accelerated MRI techniques that are k-space coverage agnostic [66,71], but these methods have not demonstrated acceleration factors ≥ 6 with success.

Radial GRAPPA with an improved calibration scheme [68] has been shown to achieve adequate image quality in cardiac MRI in the presence of undersampling factors ≥ 8, though it necessitates multiple fully-sampled k-space frames for calibration, which limits the use of the technique. Moreover, the weights calibration framework requires the calibration data to be sampled on the exact same azimuthal angles as that of the accelerated frames, after being filling with estimated projections. Therefore, radial GRAPPA, designed for the view ordering scheme that acquires every 1 out of R adjacent radial projections, cannot be directly applied to radial data acquired with the golden-angle view order.

A recently proposed self-calibrated version of radial GRAPPA [108], which uses the sequence of previous accelerated frames itself to carry out the weights calibration, demonstrated the possibility of successful weights calibration from GRAPPA kernels that are extracted from arbitrary k-space regions provided the kernels are similar in geometry to the target GRAPPA kernel. This work extends this radial GRAPPA calibration technique to be utilized in accelerated radial imaging with acquired projections on arbitrary azimuthal locations and demonstrates the feasibility of real-time cardiac MRI using the golden-angle radial view ordering.

4.2 Theory

4.2.1 Standard Radial GRAPPA versus Half-Block Self-Calibrated Radial GRAPPA

Standard radial GRAPPA weights sets used in the estimation of points missed due to undersampling are calculated from fully and sequentially sampled data acquired in advance. With self-calibration, the undersampled data itself is used for weights set determination. With radial GRAPPA [67], only every 1 out of *R* consecutive radial projections is acquired for the accelerated frames and the missing *R-1* projections are estimated. Typically, the GRAPPA kernel (or block) of size B_{read} x B_{proj} = 3x2 estimates every missing point's signal on an accelerated frame as a weighted sum of the signals of B_{read} points on both of the surrounding acquired radial projections (source projections). Conversely, "half-block" radial GRAPPA (HB-rGRAPPA) [108], uses B_{proj}=1 and a 3x1 block, estimating the signal at a missing point using only the closest acquired projection on either side. The half-block kernel facilitates the collection of geometrically "similar" kernel occurrences (or repetitions) for weights set estimation during self-calibration as finding occurrences of kernels using a single source projection is easier than that of the traditional GRAPPA kernel with two source projections. We define kernel similarity as the inverse of the distance (in k-space) between the mid-point of the source block and the target point.

During half-block weights set estimation, the distances between all acquired points and all other points on the same projection are examined to determine the most similar 3x1 source kernels, with typically 6-8 source kernels used for calibration. This comprises the "through-k-space" search for source-target pairs as a first step in increasing the number of viable kernel occurrences available for weights set estimation, and ultimately reducing the number of frames needed for calibration. The number of kernel occurrences is further increased with data from multiple successive accelerated frames, acquired before the accelerated frame that contains the missing point. This constitutes the "through-time" component of the weights calibration process.

4.2.2 Self-Calibrated Radial GRAPPA for Golden-Angle View Order

Any arbitrary sequence of consecutive projections based on the golden-angle view ordering has two or three distinct azimuthal gaps between adjacent projections [97]. The unsampled projections are chosen to lie integer multiples of Δ_{angle} degrees apart from the acquired projection that precedes them on the azimuthal dimension, with $\Delta_{angle} = \frac{180}{N_{\phi}}$ where N_{ϕ} is the number of projections in a fully sampled grid in the conventional radial view ordering case. This scheme of generating the locations of missing projections dictates that all azimuthal gaps on the final reconstructed k-space are equal with the exception of the gap between each acquired projection and the missing projection that comes right before it as depicted in Figure 4.1**.** Such uniformity leads to a more efficient coverage of k-space and assures that the number of projections estimated with radial GRAPPA are at a minimum while globally satisfying a maximum angle gap criterion. For a target image matrix of N_y x N_y = 128 x128, N_{ϕ} must be chosen greater than $\frac{\pi}{2}$ x 128 ≈ 200 in order to satisfy the Nyquist criterion throughout k-space, however, it has previously been shown that images can be reconstructed free of streaking artifacts using N_{ϕ} values of 128 or 144 [68,107,108], resulting in typical Δ_{angle} values of 1.40625° and 1.25° respectively. Finally, as in the original half-block radial GRAPPA reconstruction, the source blocks for missing projections reside on the acquired projection closest to them along the azimuthal dimension.

The golden-angle view ordering strategy is further different than conventional radial imaging view ordering from the perspective of collecting kernel repetitions for Half-block radial GRAPPA due to the fact that no single projection angle is ever repeated in the entire sequence of projections, which removes the possibility of utilizing the "through-time" and "through-k-space" dimensions of the process as two separate components where the total number of kernel repetitions for calibration is determined in a multiplicative manner [108]. Given that more than B_{read}xN_C kernel repetitions are required for the GRAPPA calibration system to be over-determined, the exploration for similar kernels needs to be extended beyond confining the source block to reside on the same projection. To this end, the range of candidate projections, on which the source blocks can reside, is extended to include the previous $N_{proj\_calib\_\mathrm{source}}$ -1 projections acquired before the source projection of the missing point where GRAPPA weights are to be calibrated. Then, for each one of the $N_{proj\_calib\_\mathrm{source}}$ potential source projections, $N_{kernel\_proj\_window}$ projections around this projection, based on the time acquired, are included in the search for target points that may form kernels of desired similarity, ensuring that the data in each kernel repetition may have a maximum temporal footprint of $\frac{N_{kernel\_proj\_window}.\mathrm{TR}}{2}$ where TR is the readout repetition time. The value of this temporal footprint needs to be comparable, if not less than, to that of the accelerated frames for the GRAPPA calibration process to be meaningful. The other important parameter in the kernel repetition search is D_{kernel_max} which is defined as the maximum allowed magnitude (in the k_x-k_y space) of the vector difference between the original GRAPPA kernel and the candidate kernel normalized by $\Delta k_{readout}$, distance between adjacent readout points, where the mid-point of the source block and the target point denote the starting and terminal point of a GRAPPA kernel vector respectively. D_{kernel_max} values smaller than 1 ensure that the loss in weights accuracy may not yield visible imperfections on the image level. The process of obtaining the kernel occurrences for weights calibration is depicted in Figure 4.2.

One additional set of modifications to this scheme of collecting calibration data is to confine the source block for candidate kernel occurrences to reside in a certain neighborhood around the source block of the original kernel. To this end, similar kernels were excluded from the calibration system if they resided on projections further than $\Delta_{angle\_source,max}$ degrees from the source projection of the original kernel. Similarly, candidate kernels were only included for weights calibration if the center source point resided within a neighborhood of $\Delta_{readout\_source,max}$ readout samples around the center source point of the original kernel with respect to their radial (readout) position. This enforces signal power, and thus, signal-to-noise ratio (SNR), similarity along the repetitions of the GRAPPA calibration system and helps stabilize the estimation process. This measure was deemed necessary given that kernel repetitions could generally arise from all regions of k-space, including those that have wildly different SNR levels than that of the source block in the acquired projection.

4.3 Methods

4.3.1 Simulations

To extract quantitative measures of image quality, a real-time free breathing bSSFP cardiac MRI scan was simulated using the numerical cardiac MRI phantom MRXCAT [112], which is based on the XCAT phantom [152,153] that delivers realistic tissue masks that can be parameterized for motion. Specifically, MRXCAT was utilized to generate 600 successive frames of a torso in free breathing with each frame having a temporal footprint of ~24msec where such artifact-free frames were generated via a Cartesian CINE MRI simulation (using MRXCAT). These frames were then sampled with the MRI operators provided in an open-source Matlab toolbox [148] to generate the k-space projections stream for the radial Golden-Angle trajectory that is of interest in this work.

The MRI scan and external parameters of the simulation were: TR=3.0 msec, samples on a projection ($N_{Readout}$) = 256, field of view (FoV) = 400x400 mm^2, resolution = 1.56x1.56x7.0mm^3, flip angle=60°, image matrix=256x256, N_C=16 receiver channels, SNR=20 dB, average heart rate=64 bpm, respiratory period=5 sec. Acceleration rate was varied to have number of projections on an accelerated frame, N_{ϕ_acc}, between 12 and 32, which led to temporal footprints between 36 and 96 msec. In comparison, direct non-uniform FFT (NUFFT)[9] and iterative SENSE [66,154] reconstructions were performed and normalized root mean square error (nRMSE) values with respect to the ground truth were calculated for each reconstructed frame.

4.3.2 Volunteer Studies

In vivo cardiac data were acquired under free breathing from N=2 healthy human volunteers. Informed consent was received for all experiments in accordance with the IRB approval. One volunteer was scanned on a 1.5T scanner (Aera, Siemens Medical Solutions, Erlangen, Germany) with the following parameters: N_C=36, resolution=2.03x2.03x7.0mm^3, flip angle=50°, TR=3.05ms, $N_{Readout}$=256, FoV=260x260mm. Another volunteer was scanned on a 1.5T scanner (Avanto, Siemens Medical Solutions, Erlangen, Germany) with the following parameters: N_C=30, resolution=1.72x1.72x7.0mm^3, flip angle=45°, TR=2.9ms, $N_{Readout}$=256, FoV=220x220mm. Both volunteers were scanned in the cardiac short-axis (SAX) orientation, and the second volunteer (Avanto) was additionally scanned in the vertical and horizontal long-axis (LAX) orientations.

4.3.3 Image Reconstruction

All image reconstruction was performed in MATLAB (MathWorks Inc., Natick, MA) and gridding of k-space data back to image domain was carried out via NUFFT using an open-source toolbox [148]. For the proposed radial GRAPPA reconstruction, GRAPPA weights were computed using Tikhonov regularization. Iterative non-Cartesian SENSE reconstructions were performed using the MATLAB scripts provided in the GitHub repo for the ISMRM 2013 Sunrise Educational Course [154], where coil sensitivity maps were estimated from direct NUFFT reconstructions of oversampled k-spaces, consisting of the previous $N_{proj\_calib\_\mathrm{source}}$ consecutive projections before the first spoke of the accelerated frame in an effort to keep the consistency in the amount of data used in both SENSE and GRAPPA reconstructions. A regularization lambda equal to 8 was used in all iterative SENSE reconstructions.

After an empirical exploration of the hyper-parameter space for the scheme of obtaining kernel repetitions for GRAPPA calibration, the following parameters were used in all experiments: $N_{proj\_calib\_\mathrm{source}}$ = 480, D_{kernel_max} =1.0, $\Delta_{angle\_source,max}$=3.0°, $\Delta_{readout\_source,max}$ =12. When the number of similar kernels collected for the GRAPPA weights calibration of a particular target missing point exceeded 250, the 250 most similar kernels, in terms of the vector difference from the original GRAPPA kernel, were included in the calibration. Also, Δ_{angle}=1.40625° was chosen for all reconstructions as N_{Φ} = 128 defined a fully-sampled k-space. B_{read} = 3 was utilized, yielding a Half-Block GRAPPA kernel in size 3 x 1.

To reduce residual image artifacts largely due to the variable point spread functions that results from the golden angle view order, a 5th-order temporal median filter was performed where necessary (as disclosed under the Results section of this chapter), similar to other works [48,151]. When reconstructing end-systole and/or end-diastole images, there was a nuance in the usage of this temporal filter such that the filter was applied to a series of 5 consecutive frames that were reconstructed from sets of projections with a 75% overlap between the adjacent frames.

4.4 Results

4.4.1 Simulations

Figure 4.3 shows short-axis images from the MRXCAT-based real-time MRI simulation in bend-systole and end-diastole for various undersampling factors. Images were reconstructed with all three methods (i.e direct NUFFT, Golden-Angle radial GRAPPA and iterative SENSE) and RMSEs w.r.t the respective ground truth images are reported. The temporal median filter was utilized as a post-processing step as explained in Methods. The RMSEs for GA radial GRAPPA and iterative SENSE are comparable, being mostly in the 17-19% range. However, a closer look at the images reveal that RMSEs may not correlate well with image quality as while the level of residual artifacts and/or structural degradation mostly increases with the acceleration factor, the RMSEs do not necessarily. Qualitatively speaking, the GA radial GRAPPA (GA-rGRAPPA) reconstructions are better than iterative SENSE reconstructions, especially for $N_{\phi\_acc} < 20$, with far less residual streaking and structural deformation. GA-radial-GRAPPA-reconstructed images show a higher level of blurring than those of iterative SENSE, however, the tissue structures are much more preserved unlike near-complete loss of certain structures (diaphragm wall, back wall) in the iterative SENSE reconstructions.

4.4.2 Healthy Volunteer Studies

Figure 4.4 displays reconstructions of a short-axis cardiac scan of a healthy human volunteer where every other frame from a complete cardiac cycle is shown for each of the three reconstructions (two rows per each) of the same raw k-space data. Each successive k-space frame contains 16 projections yielding a temporal resolution of 49 ms/frame. The GA radial GRAPPA reconstructions display far less residual streaking compared to iterative SENSE reconstructions. Moreover, the tissue structures around the heart (e.g. liver) display less deformation in the GA-rGRAPPA-reconstructed images. Similarly, Figure 4.7 shows images of every other frame from one cardiac cycle reconstructed with all three methods (three rows per each) where successive frames contain 12 projections, yielding a temporal resolution of 37 ms/frame. With aggressive acceleration (i.e. N_{ϕ_acc} = 12), GA-rGRAPPA reconstructions stand out from iterative SENSE reconstructions as the significant level of residual streaking that iterative-SENSE-reconstructed images is considerably suppressed in GA-rGRAPPA.

Figure 4.5 shows short-axis view images from a healthy volunteer scan reconstructed with GA-rGRAPPA, the proposed radial GRAPPA scheme tailored to the golden-angle view order. 24 successive frames, reconstructed from data containing 16 projections each, that temporally span over one full cardiac cycle are displayed (left to right). Similarly, Figure 4.8 and Figure 4.9 show GA-rGRAPPA-reconstructed images, in short-axis and horizontal long-axis views respectively, from successive k-space frames that contain 12 projections each. 36 frames that temporally span over one full cardiac cycle are displayed. In any GA-rGRAPPA reconstruction, there is no overlap (i.e. view sharing) between successive k-space frames as each frame in Figures 4.5, 4.8 and 4.9 contain 16, 12 and 12 unique (as per the continuous Golden Angle view order that does not repeat an azimuthal angle) projections. The 5-th order median filter was applied along the temporal dimension to further reduce residual artifacts for each reconstruction.

Figure 4.6 shows short-axis images from a healthy volunteer in both end-systole and end-diastole reconstructed with direct NUFFT, GA-rGRAPPA and iterative SENSE. Reconstructions from various undersampling factors are demonstrated where N_{ϕ_acc} denote the number of projections each underlying frame contains, which are centered around the same projection for all the end-systole, and similarly all end-diastole, reconstructions. No temporal median filtering was applied. GA-rGRAPPA reconstructions demonstrate clear superiority over their iterative SENSE reconstructions with little-to-no residual streaking and better preservation of morphological structures such as the heart ventricles, the liver and the chest wall. On the other hand, the papillary muscles do not appear as sharp in the GA-rGRAPPA reconstructions.

4.5 Discussion

4.5.1 Benefits of GA-rGRAPPA

The images reconstructed with the proposed radial GRAPPA scheme (GA-rGRAPPA) presented in this work demonstrate the feasibility of a novel parallel imaging methodology tailored to the golden angle radial view order. Of existing image reconstruction techniques applied to golden angle radial data, those relying solely on parallel MRI, were either based on the SENSE or the SPIRIT framework, and this work introduces the first ever GRAPPA-based technique. The aggressive acceleration factors (N_{ϕ_acc} =12, temporal resolution ≈ 36 msec) achieved in this work, as shown in Figures 4.8 and 4.9 are scarce among such pMRI methods for free-breathing cardiac MRI. The technique does not limit the utility of the golden angle view order scheme in any way as the flexibility of choosing a temporal window, where acquired projections are to be used to generate an image, is completely preserved. GA-rGRAPPA can reconstruct images from any arbitrary window of projections since no assumptions about the azimuthal locations of the acquired projections are made. The reported images appear to be in sufficient quality for measuring cardiac function metrics (e.g. EF) and for providing high frame rate cardiac monitoring for procedure guidance.

The herein-proposed radial GRAPPA method for the Golden Angle radial acquisition scheme has potential to be translated into clinic with a real-time implementation as similarly demonstrated for the standard through-time radial GRAPPA method [107]. Even though the process of obtaining kernel locations for calibration is not feasible to be on the fly, at least with the current form of the algorithm, the kernel search does not depend on the data itself, and thus, can be completed prior to the scan, if one settles on the undersampling patterns – number of projections and the projection angle of the first acquired projection – of the frames to be reconstructed. Given the locations of calibration kernels, weights can be computed and applied in real-time using a system with sufficient levels of speed and parallelization. The duration of the temporal window to accumulate enough projections for calibrating the weights for an undersampled frame is on the order of $N_{proj\_calib\_\text{source}}$.TR, which would be less than 2 seconds, and therefore, is not generally not a limiting factor in the application of real-time free breathing cardiac MRI.

4.5.2 Comparison to iterative SENSE

Images reconstructed from human studies demonstrate the robustness of the proposed technique from the image quality perspective. Compared to their iterative-SENSE (i.e. CG-SENSE) counterparts, the images reconstructed with GA-rGRAPPA exhibit fewer residual streaking artifacts and better preservation of morphological structures (e.g. liver). Such superiority in image quality is accentuated with aggressive undersampling factors ($N_{\phi\_acc} \leq 16$) (Figures 4.6, 4.7) and such level of undersampling of acquired k-spaces is necessary for real-time cardiac MRI, which underlines the utility of the proposed method. On the other hand, one drawback of the GA-rGRAPPA reconstruction is the apparent loss of sharpness. A closer look at the images reveal that the myocardium and the papillary muscles have some level of blurring, compared to iterative SENSE reconstructions. However, this is expected because k-space-based pMRI methods are generally recognized to have this blurring effect in comparison to their image-based counterparts due to the finite support of the convolution operations on the spatial frequency domain (k-space).

4.5.3 Technical Considerations and Limitations

The images reconstructed from the numerical simulation (Figure 4.3) are significantly lower in quality than those reconstructed from data acquired in the human studies. Such degradation is apparent across the board in all of the three reconstruction methods used in this work. Two main probable contributors to this are the following: Firstly, the radial k-space data are not produced as a direct outcome of the analytical Fourier Transform operation on physical (continuous) coil image information, but are generated from the temporal snapshots of images that are themselves a result of a simulation (Cartesian-sampled). This additional layer of non-ideality inevitably pushes images reconstructed from such imperfectly generated data away from the ground truth. Secondly, the magnitude of the respiratory motion is quite large, which leads to substantial background (exterior to the heart) movement over the frames. The calibration windows for both GA-rGRAPPA (obtaining GRAPPA kernels) and iterative SENSE (estimation of coil sensitivity maps) span the time necessary to acquire ($N_{proj\_calib\_\mathrm{source}} + N_{kernel\_proj\_\mathrm{window}} / 2$) projections prior to the first acquired projection of the undersampled k-space, any severe fluctuations in the data that may result from excessive motion can hinder the stability of these reconstruction methods. Nevertheless, while RMSEs on Figure 4.3 are reported slightly higher for GA-rGRAPPA reconstructions than iterative reconstruction, GA-rGRAPPA-reconstructed images exhibit qualitative superiority to their iterative SENSE counterparts, as similar to the results from human volunteer studies, with lesser residual streaking and better preservation of tissue structures. The RMSE values seem to be very sensitive to scaling (pixel intensity) rather than preservation of regional details on the images. There is complete loss of certain structures in the iterative SENSE reconstructions. While imperfect, the numerical simulation gives a ballpark estimate on the accuracy of the proposed method.

One conspicuous limitation of this study is the lack of a systematic exploration of the hyper parameters for the proposed GA-rGRAPPA technique. The search domain for kernels to be included in the GRAPPA calibration system depends on the tuple ($N_{proj\_calib\_\mathrm{source}}$, D_{kernel_max}, $\Delta_{angle\_source,max}$, $\Delta_{readout\_source,max}$) and a constant value of this tuple at (480, 1.0, 3.0°, 12) was used in obtaining calibration data for each missing point in all GA-rGRAPPA reconstructions. The main obstacle to the systematic and automated exploration of the optimal values for these parameters, similar to a hyper-parameter grid search commonly used in machine learning, was the amount of computational time entailed in searching the space of possible similar kernels as discussed in the subsequent paragraph. In addition, the lack of a reliable error metric in the simulations would also render the exercise of optimal parameter search futile, as determining the set of parameters to yield the more accurate images can be ambiguous. Thus, the values of the parameters were determined based on trial and error upon observing the reconstructions on the volunteer scans. While this particular choice led to images in high quality across the board in the volunteer studies overall, it is probable that a more optimal setting exists, especially one that varies by the k-space location of the missing point.

As discussed above, the computational complexity in obtaining the positions (projection index and readout location) of the kernels that can be used in calibrating the GRAPPA weights was a significant nuisance in this work. To be more specific, with the current algorithm for kernel search, there are $(2\Delta_{angle\_source,max}/180).(2\Delta_{readout\_source,max}).N_{proj\_calib\_\mathrm{source}}$ possible acquired k-space points that can be the center point of a source block of a similar GRAPPA kernel, and $N_{kernel\_proj\_window}.N_{Readout}$ possible target points that could be accompanied with each of these candidate source blocks to produce a calibration kernel occurrence, resulting in a grid of candidate calibration kernels in length $(2\Delta_{angle\_source,max}/180)\ .(2\Delta_{readout\_source,max}).N_{proj\_calib\_\mathrm{source}}.$ $N_{kernel\_proj\_window}.N_{Readout}$ for every missing point in the undersampled k-space. Every possible candidate kernel is checked for the condition of similarity by calculating the vector difference between its source block and the target point and testing whether it doesn't exceed D_{kernel_max}. Taking into the entire set of missing k-space points for which GRAPPA weights are to be computed, for an undersampled frame with N_{ϕ_acc}=16, there are over 36 million such operations, and therefore, the search takes > 8 hours on average to complete on our current system with a parallelization factor of 6 (without exceeding memory constraints). While this appears as a major drawback of the technique, future work can speed the calibration kernel search by several folds via smart modifications to the current algorithm. One such modification could be along the dimension of the missing points: Since there are significant overlaps in the grid of candidate kernels between missing points, especially for those in close proximity, the geometries of candidate kernels that have already been calculated for one missing point can be cached and this information can be used in calculating the similarity (in vector difference) between that candidate kernel and another missing point, since vector operations are associative. This would lead to a drastic shrinkage of the grid of candidate kernels for calibration.

While GA-rGRAPPA is founded on principles of parallel imaging and does not directly utilize the explicit assumption of temporal sparsity, unlike some other techniques based on compressed sensing [96,151], the necessity of an extended temporal window ($\sim N_{proj\_calib\_\mathrm{source}}.\mathrm{TR}$) from which data are used for calibration likely requires the information to be relatively sparse along this (temporal) dimension. It is yet unclear the degree of temporal fluctuations this technique may survive, thus, further exploration may be necessary to test the real limits of this technique such as reconstructions on data acquired from patients with arrhythmias.

4.5.4 Conclusion

This chapter describes a novel self-calibrated radial GRAPPA technique that can be utilized in accelerated radial imaging with arbitrary azimuthal sampling. The technique is demonstrated on cardiac data acquired continuously with the golden-angle radial view order where single-shot images from as low as 12 radial projections are reconstructed with success. Since calibration data to reconstruct an arbitrarily chosen undersampled frame is collected from the stream of previous readouts only, this technique is suitable for real-time monitoring of cardiac function and may also be utilized for MR-guided interventional procedures

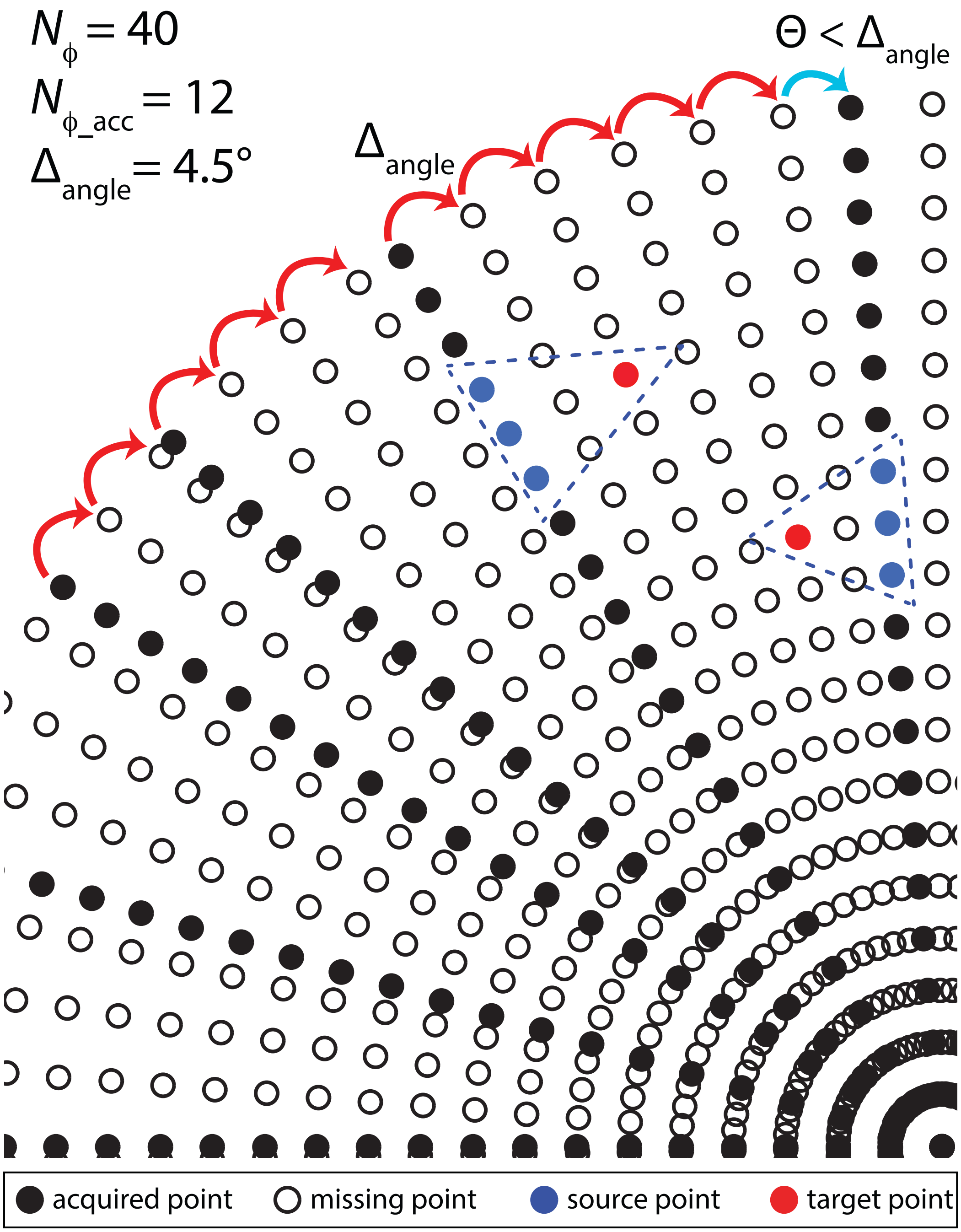

Figure 4.1. Depiction of the framework that constructs the accelerated k-space for reconstruction on a frame that contains 12 acquired projections. For demonstration purposes, N_ϕ is chosen to be 40, and thus, each "missing projection" lies Δ_{angle} = 4.5° apart from the projection that precedes it (azimuthal location increases clockwise). This leads to a near-uniform distribution of radial projections in the fully-sampled grid and also results in the smallest number of missing projections while ensuring no azimuthal gap exceeds 180 / Δ_{angle}. Blue dashed lines indicate Half-block radial GRAPPA kernels that are used in the estimation of the missing points (open circles).

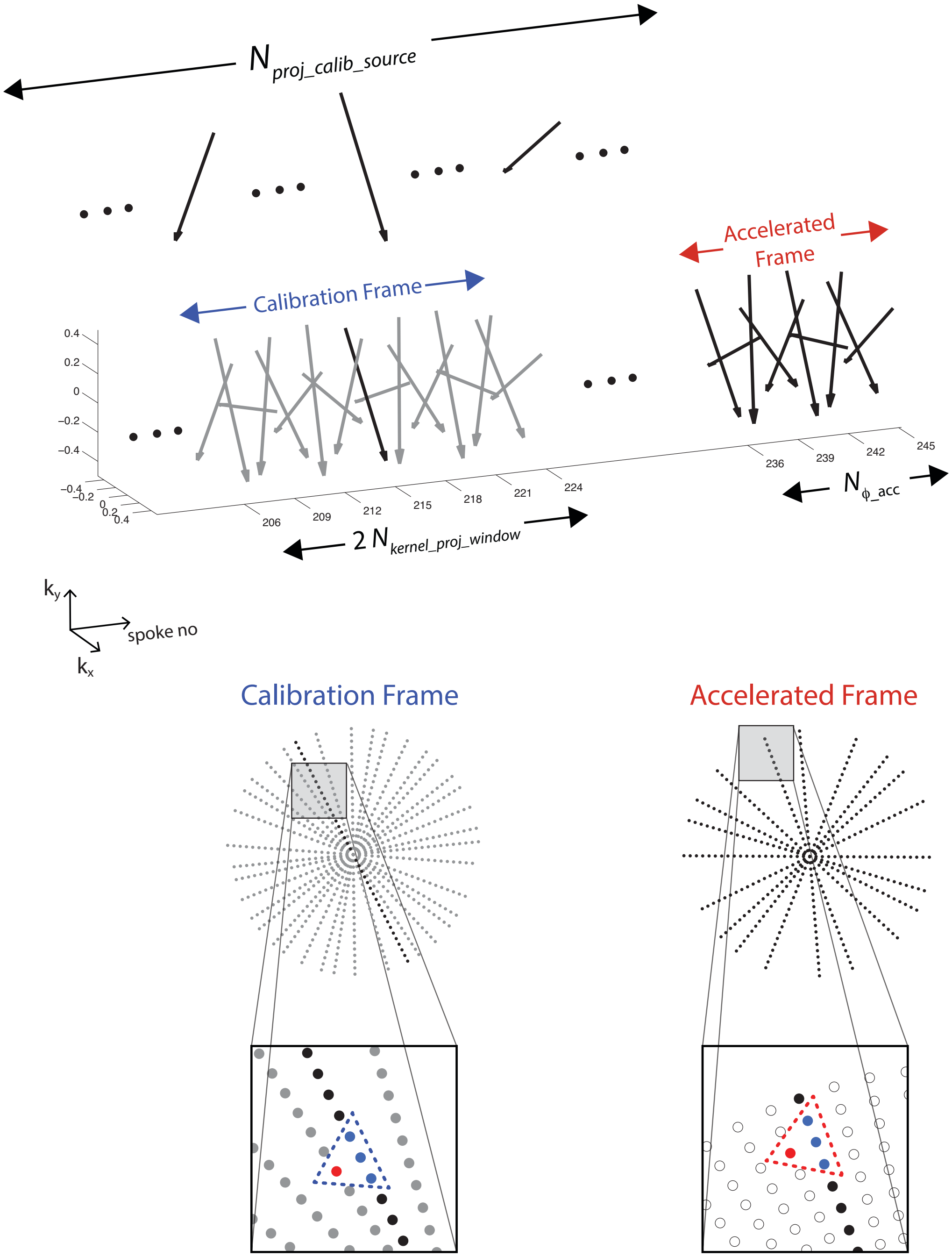

Example *Similar* Kernel
(Calibration)

Actual GRAPPA Kernel
(Reconstruction)

Figure 4.2. Depiction of the process of collecting similar kernel occurrences for GRAPPA weights calibration. There are $N_{proj\_calib\_\mathrm{source}}$ calibration frames and one such frame is visualized here, where the black spoke represent the source projection and gray spokes represent possible target projections (on which the target point in a similar GRAPPA kernel can lie). For each particular reconstruction block (dashed red line), every calibration frame is searched for possible similar kernels (dashed blue line). Data on such similar kernels then constitute the linear system for GRAPPA weights calibration for that particular missing point on the accelerated frame.

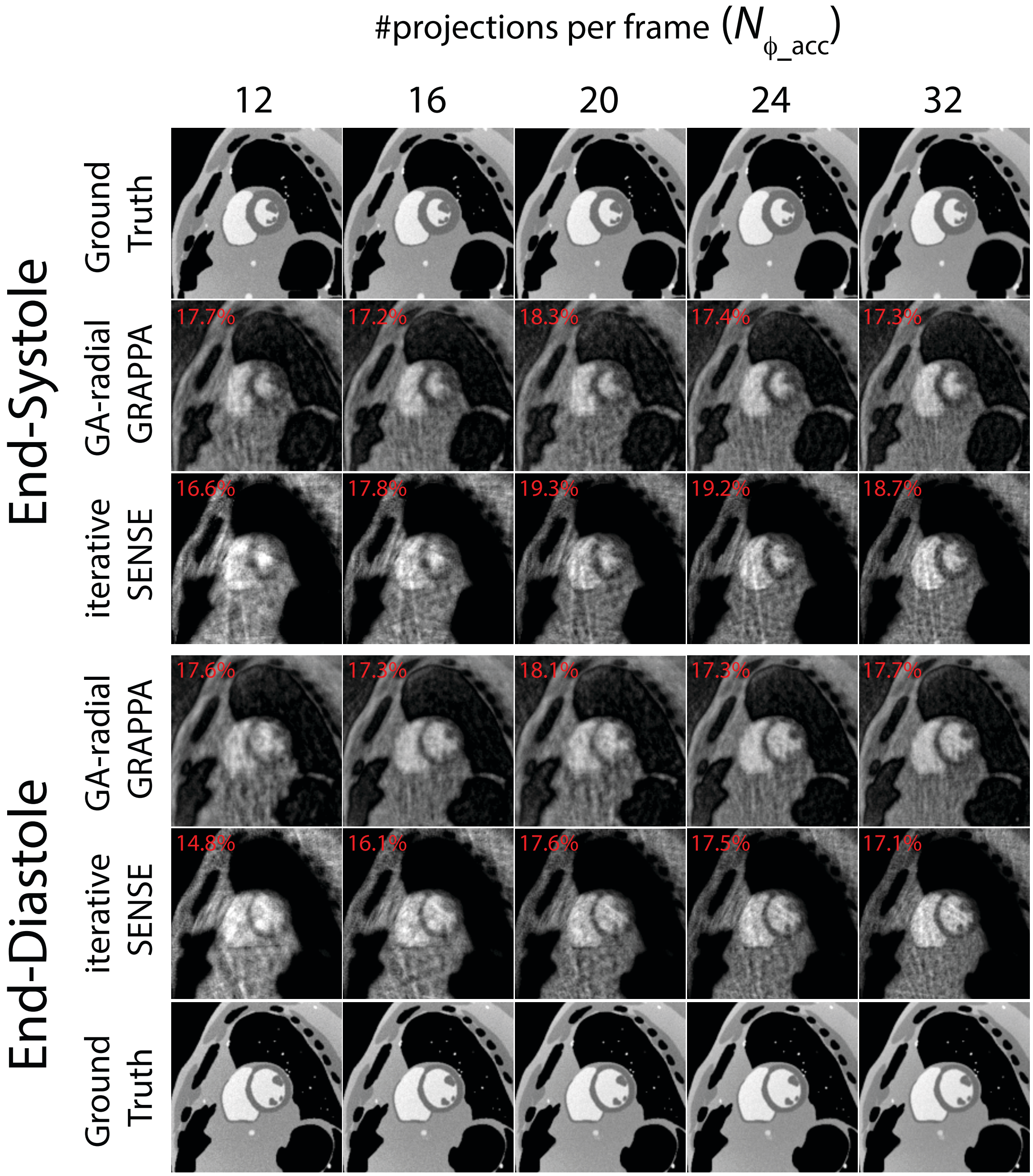

Figure 4.3. Example end-systolic and end-diastolic images from the real-time free breathing short-axis slice numerical simulation (MRXCAT). Reconstructions were performed with the proposed radial GRAPPA method and iterative SENSE, and RMSE values are displayed with respect to the respective ground truth images. Reconstructed images from data with various undersampling factors (N_{ϕ_acc}) are displayed.

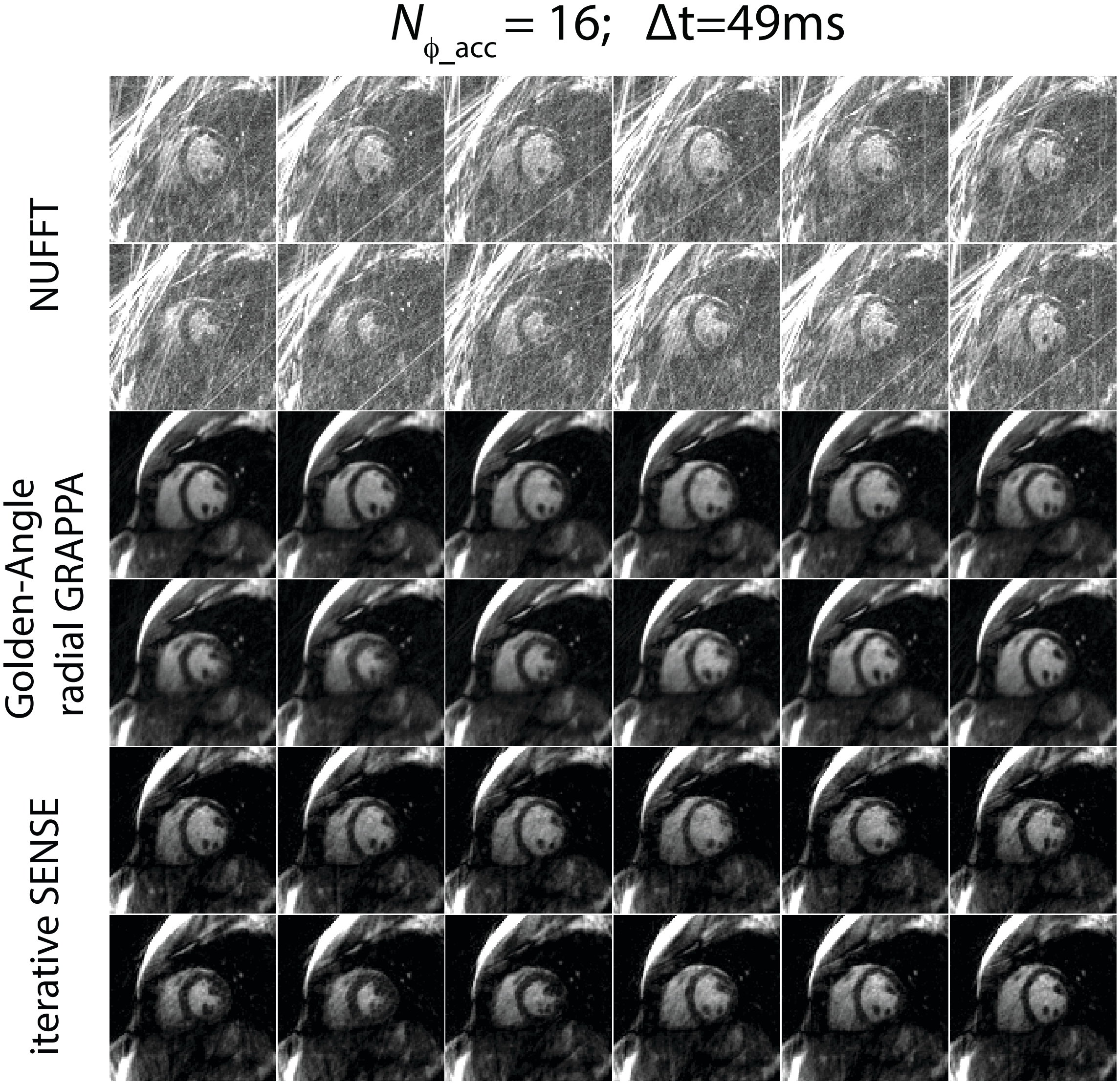

Figure 4.4. Example images from a human short-axis slice reconstructed with direct NUFFT, the proposed radial GRAPPA method and iterative SENSE. Image series where every other frame from successive frames over one cardiac cycle are displayed (left to right). Each frame contains 16 acquired projections yielding a temporal resolution of 49 ms/frame and a spatial resolution of 2.03x2.03 mm^2.

Figure 4.5. Example images from a human short-axis slice reconstructed with the proposed radial GRAPPA technique tailored to the golden-angle view order acquisition. 24 successive reconstructed frames that span over one cardiac cycle are displayed (left to right). Each frame contains 16 acquired projections yielding a temporal resolution of 49 ms/frame and a spatial resolution of 2.03x2.03mm^2. A 5-th order median filter was applied along the temporal dimension to further reduce residual artifacts.

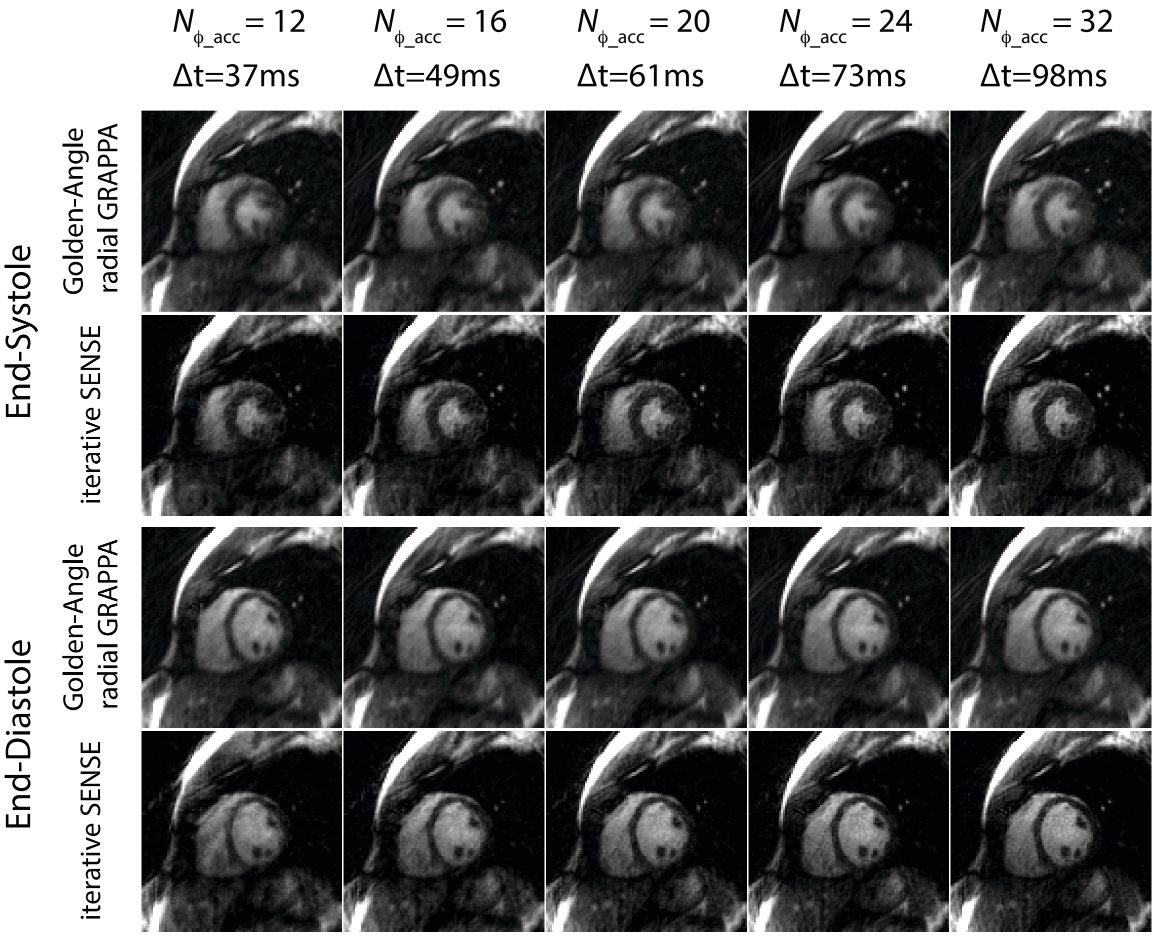

Figure 4.6. Example end-systolic and end-diastolic images from a human short-axis slice reconstructed with the proposed radial GRAPPA method and iterative SENSE are displayed. Images from data with various undersampling factors are shown. N_{ϕ_acc} and Δt denote the number of acquired projections for data per frame and the temporal footprint of the images, respectively.

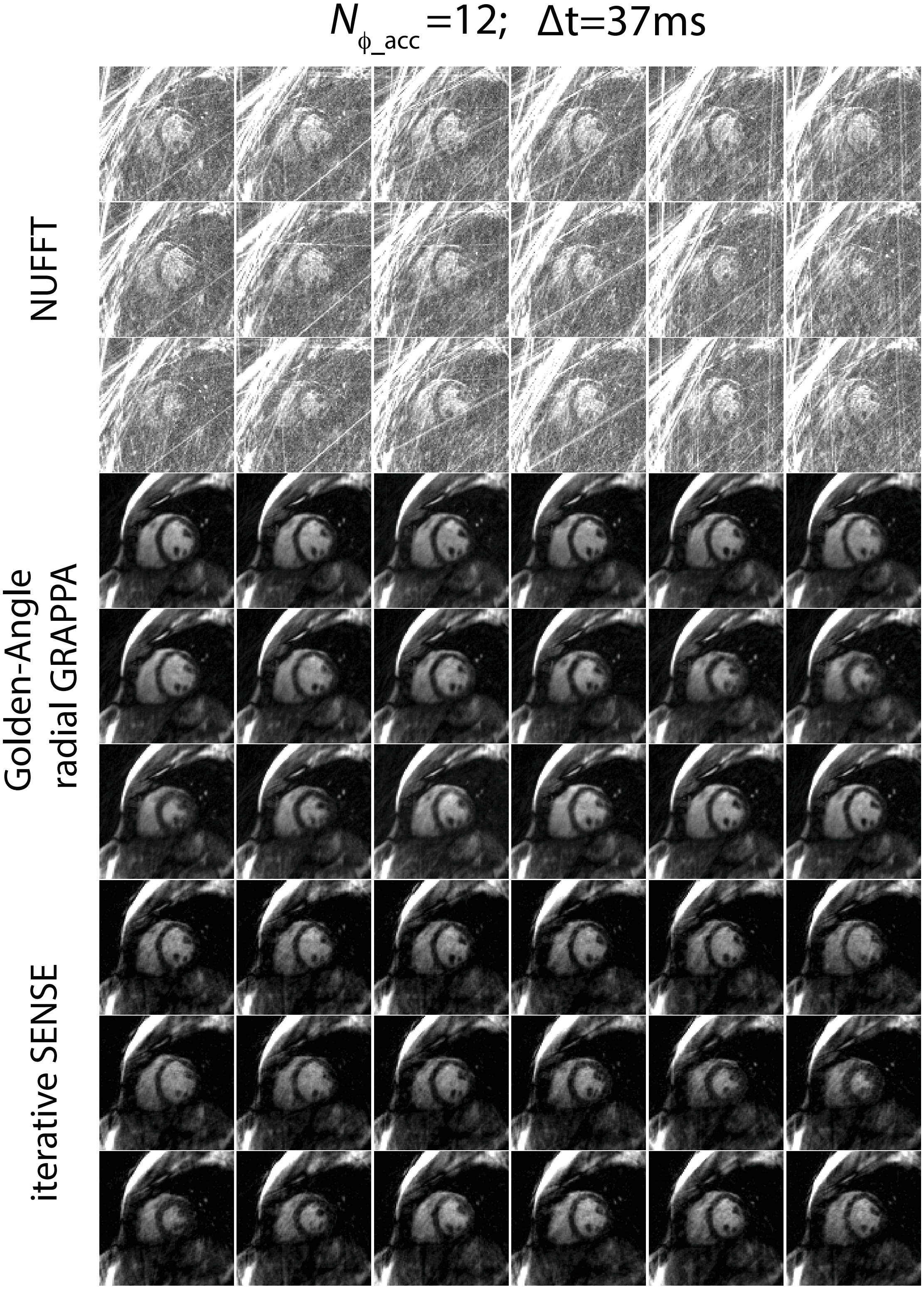

Figure 4.7. Example images from a human short-axis slice reconstructed with direct NUFFT, the proposed radial GRAPPA method and iterative SENSE. Image series where every other frame from successive frames over one cardiac cycle are displayed (left to right). Each frame contains 12 acquired projections yielding a temporal resolution of 37 ms/frame and a spatial resolution of 2.03x2.03 mm^2.

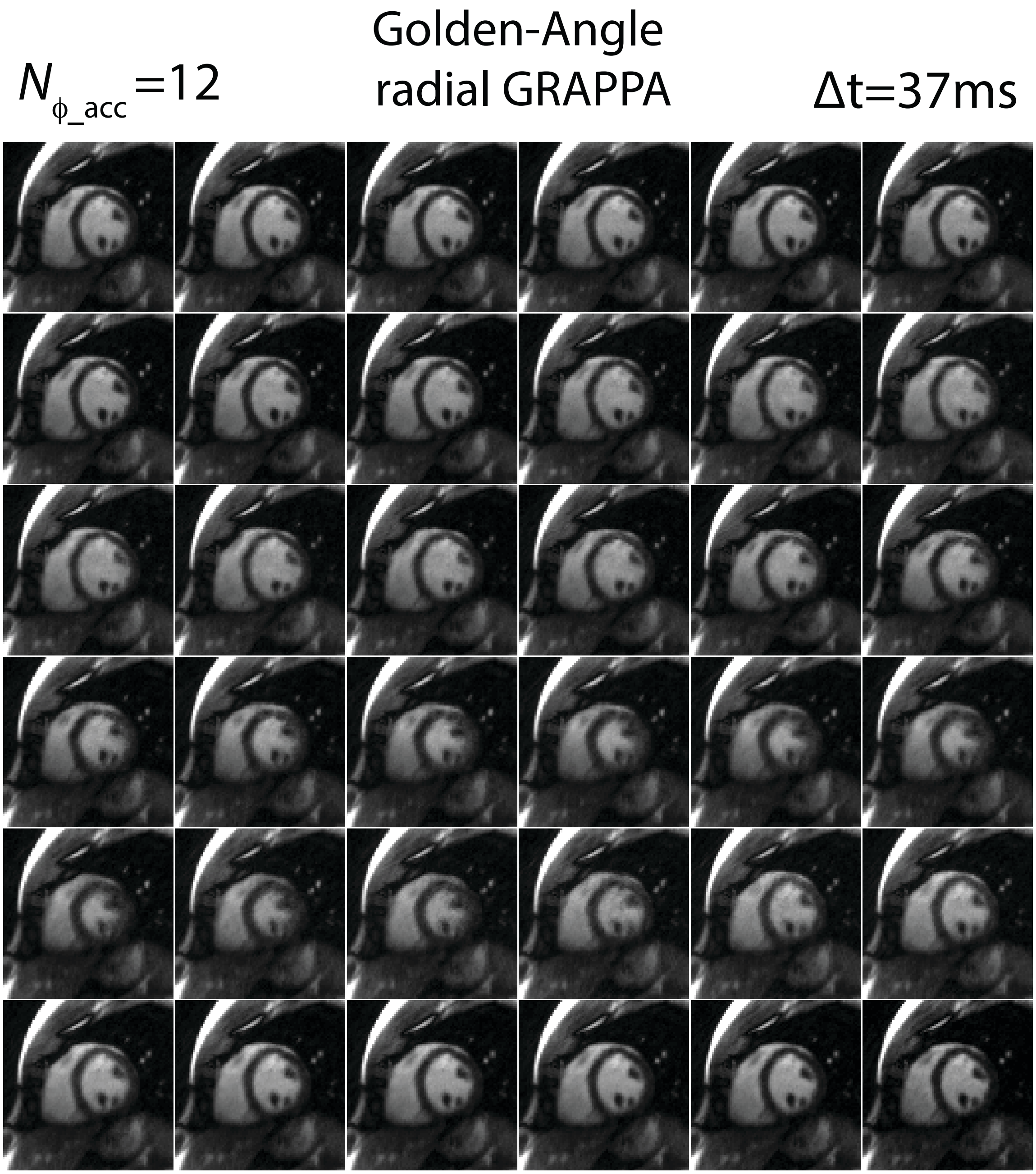

Figure 4.8. Example images from a human short-axis slice reconstructed with the proposed radial GRAPPA technique tailored to the golden-angle view order acquisition. 36 successive reconstructed frames that span over one cardiac cycle are displayed (left to right). Each frame contains 12 acquired projections yielding a temporal resolution of 37ms/frame and a spatial resolution of 2.03x2.03 mm^2. A 5-th order median filter was applied along the temporal dimension to further reduce residual artifacts.

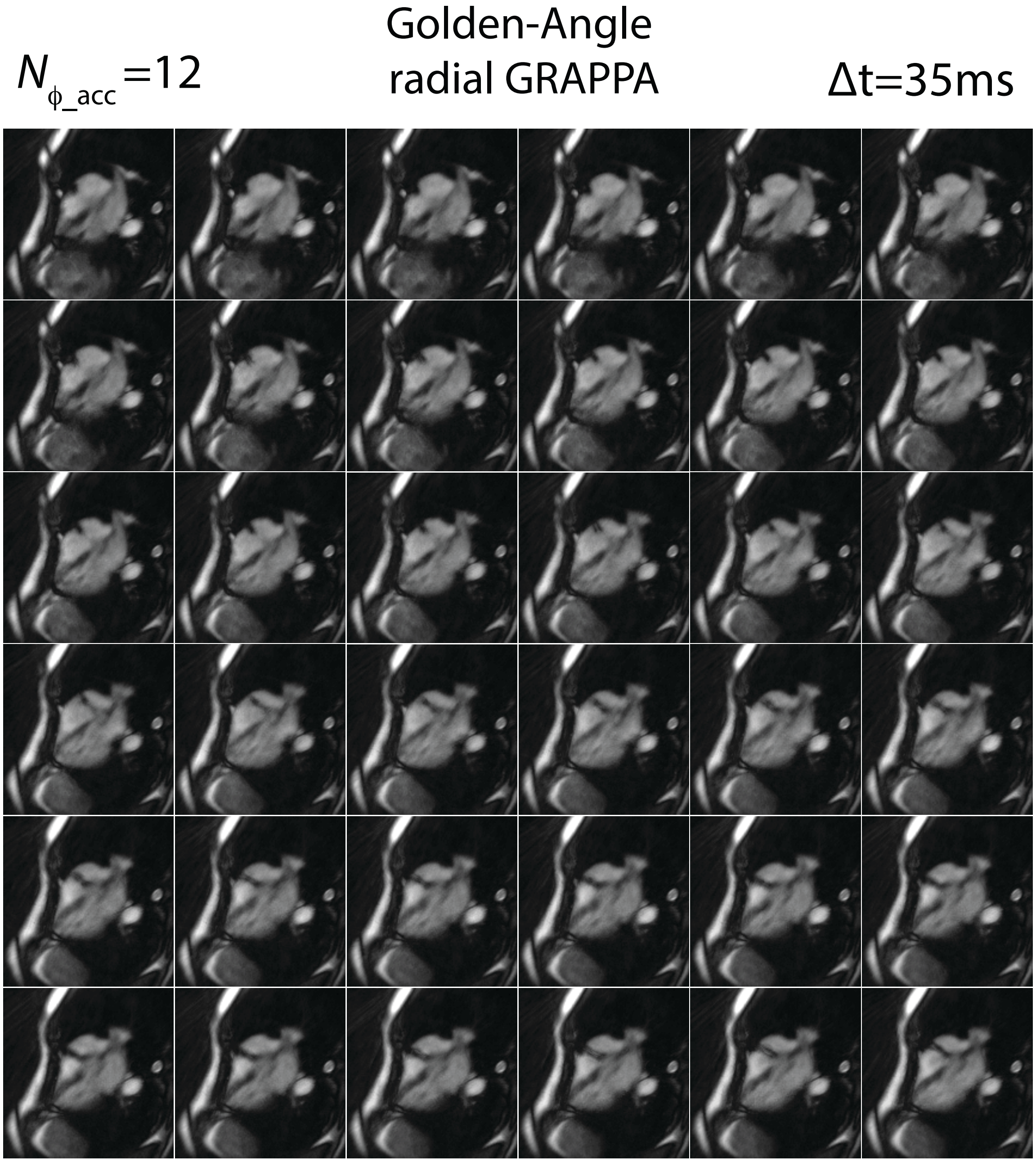

Figure 4.9. Example images from a human horizontal long-axis slice reconstructed with the proposed radial GRAPPA technique tailored to the golden-angle view order acquisition. 36 successive reconstructed frames that span over one cardiac cycle are displayed (left to right). Each frame contains 12 acquired projections yielding a temporal resolution of 35ms/frame and a spatial resolution of 1.72x1.72 mm^2. A 5-th order median filter was applied along the temporal dimension to further reduce residual artifacts.

5 CONCLUSION

5.1 Summary of the Current Work

In the present work, two novel techniques for highly accelerated MRI for the real-time monitoring of cardiac motion have been developed. In both techniques, the underlying data for an image is acquired in a single shot, in temporal windows described as the temporal footprint of a frame. As explained in the Introduction, the temporal footprints of images generally need to be shorter than 50ms, and with the current state of MRI hardware, this leads to images that are severely undersampled with missing spatial frequency information. In this work, images were reconstructed after estimating this information void in the spatial frequency domain (k-space) from data acquired during the previous frames of the same accelerated MRI scan. This distinguishes the novel techniques proposed in this work from other recent methods that achieve similar artifact-free reconstructions with high temporal resolution for real-time cine imaging in the sense that information content to reconstruct an image is not borrowed from data acquired a posteriori. The techniques were validated on animal and healthy human subject studies, with all the human MRI scans being performed under free breathing.

The common components among the techniques proposed, which enabled the reconstruction of images with sub-50ms temporal footprints, are the choices of radial k-space sampling and a k-space-based parallel imaging methodology. A novel technique that utilized both methodologies was developed previously, however, a separate calibration pre-scan that precedes the actual accelerated is required to collect the information to facilitate artifact-free reconstructions, and one of the important contributions of the current work is a self-calibration methodology that eliminates the requirement of an additional pre-scan. Another impactful contribution of this work is the generalization of this self-calibration method to a golden-angle radial view order, as an effort to leverage the flexibilities it brings, with the technique potentially being applicable to other arbitrary k-space sampling patterns. Much of the insights that guided the ideas to extend the originally proposed image reconstruction method to a self-calibrated technique are derived from the work describes in Chapter 2, which entailed a thorough quantitative analysis of the method in the context of real-time cardiac imaging.

5.2 Limitations and Future Work

The real-time single-shot images reconstructed via the novel techniques proposed in this work are comparable to other images reported by other cardiac MRI methods from an image quality perspective. However, the current work includes no evaluations of these methods on their ability to produce accurate cardiac functions indexes such as the left ventricular ejection fraction or the stroke volume. To validate the techniques further, myocardial mass measurements need to be conducted from the reconstructed images and this process needs to be performed on data acquired from numerous human subjects to facilitate robust statistical analyses. Similarly, the proposed techniques are suitable for imaging patients with arrhythmias, as no motion periodicity is assumed, but access to a patient population has been unavailable throughout this work. Real-time, open ended, monitoring of the cardiac motion is a challenging task, at which the methods proposed here have great potential in succeeding, but the validation of their capabilities in detecting irregular cardiac beats remain outstanding.

The utility of real-time monitoring of cardiac motion and function is relevant in the clinic only if the images can be generated on the fly. However, all image reconstructions were carried out offline via MATLAB scripts. Real-time reconstructions on radial GRAPPA have previously been demonstrated using a GPU-based system, therefore, the methods proposed in this work also have the potential to be translated to clinic with a real-time online setting. Providing that a real-time implementation is successful, the techniques may also provide value for MR-guided electrophysiology procedures where reconstructions need to accommodate frequent changes in slice orientations. Finally, this work can be extended to accelerated imaging with other non-Cartesian k-space trajectories such as spiral sampling.

REFERENCES

1. Edelstein WA, Hutchison JMS, Johnson G, Redpath T. Spin warp NMR imaging and applications to human whole-body imaging. Phys. Med. Biol. 1980;25:751–756. doi: 10.1088/0031-9155/25/4/017.

2. Oppenheim A V, Schafer R, JR B. Discrete-Time Signal Processing. 2nd Editio. Upper Saddle River, NJ, USA: Prentice-Hall, Inc.; 1999.

3. Ahmed N, Rao KR. Orthogonal Transforms for Digital Signal Processing. New York Springer-Verlag; 1975.

4. Lauterbur PC. Image Formation by Induced Local Interactions: Examples Employing Nuclear Magnetic Resonance. Nature 1973;242:190–191. doi: 10.1038/242190a0.

5. Natterer F. The Mathematics of Computerized Tomography. Stuttgart: Teubner; 1986.

6. Rasche V, Proksa R, Sinkus R, Börnert P, Eggers H. Resampling of data between arbitrary grids using convolution interpolation. IEEE Trans. Med. Imaging 1999;18:385–92. doi: 10.1109/42.774166.

7. Jackson JI, Meyer CH, Nishimura DG, Macovski A. Selection of a Convolution Function for Fourier Inversion Using Gridding. IEEE Trans. Med. Imaging 1991;10:473–478. doi: 10.1109/42.97598.

8. Pipe JG, Menon P. Sampling density compensation in MRI: Rationale and an iterative numerical solution. Magn. Reson. Med. 1999;41:179–186.

9. Fessler J a., Sutton BP. Nonuniform fast fourier transforms using min-max interpolation. IEEE Trans. Signal Process. 2003;51:560–574. doi: 10.1109/TSP.2002.807005.

10. Brodsky EK, Samsonov A a, Block WF. Characterizing and correcting gradient errors in non-cartesian imaging: Are gradient errors linear time-invariant (LTI)? Magn. Reson. Med. 2009;62:1466–76. doi: 10.1002/mrm.22100.

11. Boll D, Merkle E, Seaman D, Gilkeson R, Larson A, Simonetti O, Duerk J, Lewin J.

Comparison of ECG-Gated Rectilinear vs. Real-Time Radial K-Space Sampling Schemes in Cine True-FISP Cardiac MRI. J. Cardiovasc. Magn. Reson. 2004;6:793–802. doi: 10.1081/JCMR-200036124.

12. Kinahan PE, Defrise M, Clackdoyle R. The Fundamentals of PET and SPECT. In: Analytic Image Reconstruction Methods In Emission Tomography. Elsevier Inc.; 2004. pp. 421–442. doi: 10.1016/B978-012744482-6.50023-5.

13. Scott AD, Keegan J, Firmin DN. Motion in Cardiovascular MR Imaging. Radiology 2009;250:331–351. doi: 10.1148/radiol.2502071998.

14. Runge VM, Mark R. Progress In Radiology Overcoming Motion in Abdominal. 1988.

15. Runge VM, Wood ML. Fast imaging and other motion artifact reduction schemes: A pictorial overview. Magn. Reson. Imaging 1988;6:595–608. doi: 10.1016/0730-725X(88)90135-X.

16. Sakuma H, Fujita N, Foo T, Caputo G, Nelson S, Hartiala J, Shimakawa A, Higgins C. Evaluation of left ventricular volume and mass with breath-hold cine MR imaging. Radiology 1993;188:377–380.

17. Pelc N, Herfkens R, Shimakawa A, Enzmann D. Phase contrast cine magnetic resonance imaging. Magn Reson Q 1991;7(4):229–54.

18. Giri S, Chung Y-C, Merchant A, Mihai G, Rajagopalan S, Raman S V, Simonetti OP. T2 quantification for improved detection of myocardial edema. J. Cardiovasc. Magn. Reson. 2009;11:56. doi: 10.1186/1532-429X-11-56.

19. Eitel I, Friedrich MG. T2-weighted cardiovascular magnetic resonance in acute cardiac disease. J. Cardiovasc. Magn. Reson. 2011;13:13. doi: 10.1186/1532-429X-13-13.

20. Schwitter J. Myocardial perfusion. J. Magn. Reson. Imaging 2006;24:953–963. doi: 10.1002/jmri.20753.

21. Kim RJ, Fieno DS, Parrish TB, Harris K, Chen E, Simonetti O, Bundy J, Finn JP, Klocke FJ, Judd RM. Irreversible Injury , Infarct Age , and Contractile Function. Circulation 1999;100:1992–2003.

22. Detsky JS, Stainsby J a, Vijayaraghavan R, Graham JJ, Dick a J, Wright G a. Inversion-recovery-prepared SSFP for cardiac-phase-resolved delayed-enhancement MRI. Magn. Reson. Med. 2007;58:365–72. doi: 10.1002/mrm.21291.

23. Hall EJ. Lessons we have learned from our children : cancer risks from diagnostic radiology. Pediatr. Radiol. 2002:(32) 700–706. doi: 10.1007/s00247-002-0774-8.

24. Setser RM, Fischer SE, Lorenz CH. Quantification of left ventricular function with magnetic resonance images acquired in real time. J. Magn. Reson. Imaging 2000;12:430–8.

25. Oppelt A, Graumann R, Barfuss H, Fischer H, Hertl W, Schajor W. FISP: a new fast MRI sequence. Electromedica 1986; 3:15-18.

26. Hori Y, Yamada N, Higashi M, Hirai N, Nakatani S. Rapid Evaluation Of Right And Left Ventricular Function And Mass Using Real-time True-fisp Cine Mr Imaging Without Breath-hold: Comparison With Segmented True-fisp Cine Mr Imaging With Breath-hold. J. Cardiovasc. Magn. Reson. 2003;5:439–450. doi: 10.1081/JCMR-120022260.

27. Epstein FH, Kim D, McVeigh E. Reducing signal oscillations during the approach to steady state in True FISP using partial dephasing. In: Proceedings of the 9th Annual Meeting of ISMRM, Glasgow, Scotland, 2001. p 1786.

28. Scheffler K, Lehnhardt S. Principles and applications of balanced SSFP techniques. Eur. Radiol. 2003;13:2409–18. doi: 10.1007/s00330-003-1957-x.

29. Atkinson D J, Edelman R R. Cineangiography of the heart in a single breath hold with segmented turbo-FLASH sequence. Radiology 1991; 178: 357–360

30. Polson MJ, Barker AT GS. The effect of rapid rise-time magnetic fields on the ECG of the rat. Clin Phys Physiol Meas 1982;3:231–234.

31. Rokey R, Wendt R, Johnston D. Monitoring of acutely ill patients during nuclear magnetic resonance imaging: use of a time-varying filter electrocardiographic gating device to reduce gradient artifacts. Magn Reson Med 1988;6:240–5.

32. Dimick R, Hedlund L, Fram E, Utz J HR. Optimizing ECG Electrode Placement for

Cardiacgated Magnetic-Resonance-Imaging. Invest Radiol. 1986;21:S36–S36.

33. Laudon MK, Webster JG, Frayne R GT. Minimizing interference from magnetic resonance imagers during electrocardiography. IEEE Trans Biomed Eng 1998;45:160–4.

34. TA S. Wireless retrospective gating: application to cine cardiac imaging. Magn Reson Imaging 1990;8:675–81.

35. Larson AC, White RD, Laub G, McVeigh ER, Li D SO. Self-gated cardiac cine MRI. Magn Reson Med. 2004;51:93–102.

36. Buehrer M, Curcic J, Boesiger P KS. Prospective self-gating for simultaneous compensation of cardiac and respiratory motion. Magn Reson Med. 2008;60:683–90.

37. Odille F, Uribe S, Batchelor PG, Prieto C, Schaeffter T AD. Model-based reconstruction for cardiac cine MRI without ECG or breath holding. Magn Reson Med. 2010;63:1247–57.

38. Stehning C, Bornert P, Nehrke K, Eggers H SM. Free-breathing whole-heart coronary MRA with 3D radial SSFP and self-navigated image reconstruction. Magn Reson Med. 2005;54:76–80.

39. Holland AE, Goldfarb JW ER. Diaphragmatic and cardiac motion during suspended breathing: preliminary experience and implications for breath-hold MR imaging. Radiology. 1998;209:483–9.

40. Runge VM, Clanton JA, Partain CL JA. Respiratory gating in magnetic resonance imaging at 0.5 Tesla. Radiology. 1984;151:521–3.

41. Ehman RL, McNamara MT, Pallack M, Hricak H HC. Magnetic resonance imaging with respiratory gating: techniques and advantages. AJR Am J Roentgenol. 1984;143:1175–82.

42. Xue H, Kellman P, Larocca G, Arai AE, Hansen MS. High spatial and temporal resolution retrospective cine cardiovascular magnetic resonance from shortened free breathing real-time acquisitions. J. Cardiovasc. Magn. Reson. 2013;15:102. doi: 10.1186/1532-429X-15-102.

43. Kellman P, Chefd'hotel C, Lorenz CH, Mancini C, Arai AE, McVeigh ER. High spatial and temporal resolution cardiac cine MRI from retrospective reconstruction of data acquired in real time using motion correction and resorting. Magn. Reson. Med. 2009;62:1557–64. doi:

10.1002/mrm.22153.

44. Hu P, Hong S, Moghari MH, Goddu B, Goepfert L KK V. Motion correction using coil arrays (MOCCA) for free-breathing cardiac cine MRI. Magn Reson Med. 2011;66:467– 75.

45. Roemer PB, Edelstein W a, Hayes CE, Souza SP, Mueller OM. The NMR phased array. Magn. Reson. Med. 1990;16:192–225.

46. Walsh DO, Gmitro AF, Marcellin MW. Adaptive reconstruction of phased array MR imagery. Magn Reson Med. 2000;43:682–690

47. Voit D, Zhang S, Unterberg-Buchwald C, Sohns JM, Lotz J, Frahm J. Real-time cardiovascular magnetic resonance at 1.5 T using balanced SSFP and 40 ms resolution. J. Cardiovasc. Magn. Reson. 2013;15:79. doi: 10.1186/1532-429X-15-79.

48. Zhang S, Uecker M, Voit D, Merboldt K-D, Frahm J. Real-time cardiovascular magnetic resonance at high temporal resolution: radial FLASH with nonlinear inverse reconstruction. J. Cardiovasc. Magn. Reson. 2010;12:39. doi: 10.1186/1532-429X-12-39.

49. Sodickson DK, Manning WJ. Simultaneous acquisition of spatial harmonics (SMASH): fast imaging with radiofrequency coil arrays. Magn. Reson. Med. 1997;38:591–603.

50. Madore B, Glover GH, Pelc NJ. Unaliasing by fourier-encoding the overlaps using the temporal dimension (UNFOLD), applied to cardiac imaging and fMRI. Magn. Reson. Med. 1999;42:813–28.

51. Pruessmann KP, Weiger M, Scheidegger MB, Boesiger P. SENSE: sensitivity encoding for fast MRI. Magn. Reson. Med. 1999;42:952–62.

52. Griswold M a, Jakob PM, Heidemann RM, Nittka M, Jellus V, Wang J, Kiefer B, Haase A. Generalized autocalibrating partially parallel acquisitions (GRAPPA). Magn. Reson. Med. 2002;47:1202–10. doi: 10.1002/mrm.10171.

53. Yeh EN, Price MD. Recent advances in image reconstruction, coil sensitivity calibration, and coil array design for SMASH and generalized parallel MRI. 2002;13:158–163.

54. Pruessmann KP. Encoding and Reconstruction in Parallel MRI. NMR Biomed. 2006:288–

299. doi: 10.1002/nbm.1042.

55. Lustig M, Donoho D, Pauly JM. Sparse MRI: The application of compressed sensing for rapid MR imaging. Magn. Reson. Med. 2007;58:1182–1195. doi: 10.1002/mrm.21391.

56. Donoho DL, Santos JM, Pauly JM. Compressed Sensing MRI IEEE Signal Process. Mag. 2008;25(2):72–82.

57. Huang F, Akao J, Vijayakumar S, Duensing GR, Limkeman M. k-t GRAPPA: a k-space implementation for dynamic MRI with high reduction factor. Magn. Reson. Med. 2005;54:1172–84. doi: 10.1002/mrm.20641.

58. Tsao J, Boesiger P, Pruessmann KP. k-t BLAST and k-t SENSE: dynamic MRI with high frame rate exploiting spatiotemporal correlations. Magn. Reson. Med. 2003;50:1031–42. doi: 10.1002/mrm.10611.

59. Glover GH, Pauly JM. Projection Reconstruction Techniques for Reduction of Motion Effects in MRI. Magn. Reson. Med. 1992;28:275–289. doi: 10.1002/mrm.1910280209.

60. Meyer CH, Hu BS, Nishimura DG, Macovski A. Fast Spiral Coronary Artery Imaging. Magn. Reson. Med. 1992;13:202–213.

61. Ahn CB, Kim JH, Cho ZH. High-Speed Spiral-Scan Echo Planar NMR Imaging-I. IEEE Trans Med Imaging 1986;MI-5(1):2–7.

62. Qian Y, Zhang Z, Stenger VA, Wang Y. Self-calibrated spiral SENSE. Magn. Reson. Med. 2004;52:688–92. doi: 10.1002/mrm.20197.

63. Peters DC, Rohatgi P, Botnar RM, Yeon SB, Kissinger K V, Manning WJ. Characterizing radial undersampling artifacts for cardiac applications. Magn. Reson. Med. 2006;55:396–403. doi: 10.1002/mrm.20782.

64. Schaeffter T, Weiss S, Eggers H, Rasche V. Projection Reconstruction Balanced Fast Field Echo for Interactive Real-Time Cardiac Imaging. Magn. Reson. Med. 2001;46:1238–1241.

65. Gmitro AF, Alexander AL. Use of a Projection Reconstruction Method to Decrease Motion Sensitivity in Diffusion-Weighted MRI. Magn. Reson. Med. 1993;29(6):835–838.

66. Pruessmann KP, Weiger M, Bo P, Boesiger P. Advances in Sensitivity Encoding With Arbitrary k -Space Trajectories. Magn. Reson. Med. 2001;46:638–651.

67. Griswold MA, Heidemann RM, Jakob PM. Direct Parallel Imaging Reconstruction of Radially Sampled Data Using GRAPPA with Relative Shifts Synopsis. In: Proc. Intl. Soc. Mag. Reson. Med. 11. 2003;11:2349.

68. Seiberlich N, Ehses P, Duerk J, Gilkeson R, Griswold M. Improved radial GRAPPA calibration for real-time free-breathing cardiac imaging. Magn. Reson. Med. 2011;65:492–505. doi: 10.1002/mrm.22618.

69. Seiberlich N, Breuer F, Blaimer M, Jakob P, Griswold M. Self-calibrating GRAPPA operator gridding for radial and spiral trajectories. Magn. Reson. Med. 2008;59:930–5. doi: 10.1002/mrm.21565.

70. Seiberlich N, Lee G, Ehses P, Duerk JL, Gilkeson R, Griswold M. Improved temporal resolution in cardiac imaging using through-time spiral GRAPPA. Magn. Reson. Med. 2011;66:1682–8. doi: 10.1002/mrm.22952.

71. Lustig M, Pauly JM. SPIRiT: Iterative self-consistent parallel imaging reconstruction from arbitrary k-space. Magn. Reson. Med. 2010;64:457–71. doi: 10.1002/mrm.22428.

72. Hestenes MR SE. Methods of conjugate gradients for solving linear systems. Natl Bur Stand. J Res 1952;49:409–436.

73. Boubertakh R, Prieto C, Batchelor PG, Uribe S, Atkinson D, Eggers H, Sørensen TS, Hansen MS, Razavi RS, Schaeffter T. Whole-Heart Imaging Using Undersampled Radial Phase Encoding (RPE) and Iterative Sensitivity Encoding (SENSE) Reconstruction. Magn. Reson. Med. 2009;62:1331–1337. doi: 10.1002/mrm.22102.

74. Sorensen TS, Prieto C, Atkinson D, Hansen MS, Schaeffter T. GPU accelerated iterative SENSE reconstruction of radial phase encoded whole-heart MRI. Proc. 18th ISMRM Sci. Meeting Exhibit 2010;18:2869.

75. Hansen MS, Sørensen TS. Gadgetron : An Open Source Framework for Medical Image

Reconstruction. 2013;69:1768–1776. doi: 10.1002/mrm.24389.

76. Aandal G, Nadig V, Yeh V, Rajiah P, Jenkins T, Sattar A, Griswold M, Gulani V, Gilkeson RC, Seiberlich N. Evaluation of left ventricular ejection fraction using through-time radial GRAPPA. J. Cardiovasc. Magn. Reson. 2014 16(79):1–13.

77. Nadig V, Yeh V, Gulani V, Gilkeson RC, Seiberlich N. Quantification of left ventricular ejection fraction using through-time radial GRAPPA for real-time imaging. J. Cardiovasc. Magn. Reson. 2013;15:2–4.

78. Wright KL, Lee GR, Ehses P, Griswold M a, Gulani V, Seiberlich N. Three-dimensional through-time radial GRAPPA for renal MR angiography. J. Magn. Reson. Imaging 2014;40:864–74. doi: 10.1002/jmri.24439.

79. Wright KL, Chen Y, Saybasili H, Griswold MA, Seiberlich N G V. Quantitative High Resolution Renal Perfusion Imaging using 3D Through-time Radial GRAPPA. Invest Radiol. 2014;49(10):666–674.

80. A. C. Freitas, M. Ruthven, R. Boubertakh MEM. Improved real-time MRI to visualise velopharyngeal motion during speech using accelerated radial through-time GRAPPA. Magn. Reson. Mater. Phys. Biol. Med. 30(Suppl 1:S17–S18. doi: 10.1002/mrm.26611.

81. L. G. Gubin, B. T. Polyak EVR. The method of projections for finding the common point of convex sets. U.S.S.R. Comput. Math. Math. Phys. 1967;7:1–24.

82. Murphy M, Alley M, Demmel J, Keutzer K, Vasanawala S, Lustig M. Fast L1-SPIRiT Compressed Sensing Parallel Imaging MRI : Scalable Parallel Implementation and Clinically Feasible Runtime. IEEE Trans Med Imaging 2012;31:1250–1262.

83. Lustig M, Alley M, Vasanawala S, Donoho D, Pauly J. L1 SPIR-iT : Autocalibrating Parallel Imaging Compressed Sensing. In: Intl. Soc. Mag. Reson. Med. 17. ; 2009.

84. Donoho DL. Compressed Sensing. IEEE Trans. Inform. Theory 2006;52:1289–1306.

85. Kim Y, Narayanan SS, Nayak KS. Accelerated Three-Dimensional Upper Airway MRI Using Compressed Sensing. Magn. Reson. Med. 2009;61:1434–1440. doi: 10.1002/mrm.21953.

86. Akcakaya M, Hu P, Chuang ML, Hauser TH, Ngo LH, Manning WJ, Tarokh V, Nezafat R. Accelerated Noncontrast-Enhanced Pulmonary Vein MRA With Distributed Compressed Sensing. J Magn Reson Imaging 2011;33:1248–1255.

87. Hyun S, Han Y, Suh J. Accelerating knee MR imaging : Compressed sensing in isotropic three- dimensional fast spin-echo sequence. Magn. Reson. Imaging 2018;46:90–97. doi: 10.1016/j.mri.2017.10.018.

88. Akcakaya M, Nam S, Hu P, Moghari MH, Ngo LH, Tarokh V, Manning WJ NR. Compressed sensing with wavelet domain dependencies for coronary MRI: a retrospective study. IEEE Trans Med Imaging 2011;30:1090–1099.

89. Taubman DS MM. JPEG 2000: Image compression fundamentals, standards and practice. Kluwer International Series in Engineering and Computer Science. Kluwer Academic Publishers.; 2002.

90. Jung H, Sung K, Nayak KS, Kim EY, Ye JC. k-t FOCUSS : A General Compressed Sensing Framework for High Resolution Dynamic MRI. Magn Reson Med 2009;61:103–116. doi: 10.1002/mrm.21757.

91. M. Usman, C. Prieto, T. Schaeffter PB. k-t group sparse: A method for accelerating dynamic MRI. Magn. Reson. Med 2011;66:1163–1176.

92. Gamper U, Boesiger P KS. Compressed sensing in dynamic MRI. Magn Reson Med 2008;59:365–373.

93. Liang D, King K, Liu B YL. Accelerating SENSE using distributed compressed sensing. In: Proc 17th Annual Meeting ISMRM, Honolulu. ; 2009. p. p 377.

94. Otazo R, Kim D, Axel L, Sodickson DK. Combination of compressed sensing and parallel imaging for highly accelerated first-pass cardiac perfusion MRI. Magn. Reson. Med. 2010;64:767–76. doi: 10.1002/mrm.22463.

95. Vasanawala SS, Alley MT, Hargreaves BA, Barth RA, Pauly JM LM. Improved pediatric MR imaging with compressed sensing. Radiology 2010;256:607–616.

96. L. Feng, R. Grimm, K. T. Block, H. Chandarana, S. Kim, J. Xu, L. Axel, D. K. Sodickson and RO. Golden-angle radial sparse parallel MRI: Combination of compressed sensing, parallel imaging, and golden-angle radial sampling for fast and flexible dynamic volumetric MRI. Magn. Reson. Med. 2013;72:707–717.

97. Winkelmann S, Schaeffter T, Koehler T, Eggers H, Doessel O. An optimal radial profile order based on the Golden Ratio for time-resolved MRI. IEEE Trans. Med. Imaging 2007;26:68–76. doi: 10.1109/TMI.2006.885337.

98. Wright KL, Hamilton JI, Griswold M a, Gulani V, Seiberlich N. Non-Cartesian parallel imaging reconstruction. J. Magn. Reson. Imaging 2014;40:1022–40. doi: 10.1002/jmri.24521.

99. Schwab F, Schwarz F, Dietrich O, et al. Free breathing real-time cardiac cine imaging with improved spatial resolution at 3T. Invest. Radiol. 2013;48:158–66. doi: 10.1097/RLI.0b013e31827f1b68.

100. Nazarian S, Kolandaivelu A, Zviman MM, et al. Feasibility of real-time magnetic resonance imaging for catheter guidance in electrophysiology studies. Circulation 2008;118:223–9. doi: 10.1161/CIRCULATIONAHA.107.742452.

101. Aandal G, Nadig V, Yeh V, Rajiah P, Jenkins T, Sattar A, Griswold M, Gulani V, Gilkeson RC, Seiberlich N. Evaluation of left ventricular ejection fraction using through-time radial GRAPPA. J. Cardiovasc. Magn. Reson. 2014;16:79. doi: 10.1186/s12968-014-0079-8.

102. Pruessmann K P, Weiger M BP. Sensitivity encoded cardiac MRI. J. Cardiovasc. Magn. Reson. 2001;3:1–9.

103. Wintersperger BJ, Nikolaou K, Dietrich O, Johannes Rieber, Matthias Nittka, Maximilian F. Reiser SOS. Single breath-hold real-time cine MR imaging: improved temporal resolution using generalized autocalibrating partially parallel acquisition (GRAPPA) algorithm. Eur Radiol 2003;13:1931–1936.

104. M. L. Lauzon BKR. Effects of polar sampling in k-space. Magn. Reson. Med., 1996;vol 36:940–949.

105. Heidemann RM, Griswold M a, Seiberlich N, Krüger G, Kannengiesser S a R, Kiefer B, Wiggins G, Wald LL, Jakob PM. Direct parallel image reconstructions for spiral trajectories using GRAPPA. Magn. Reson. Med. 2006;56:317–26. doi: 10.1002/mrm.20951.

106. Sayin O, Saybasili H, Halperin H, Zviman M, Griswold MA, Seiberlich N, Herzka DA. Accelerated delayed enhancement imaging of myocardial infarction with through-time radial GRAPPA. J. Cardiovasc. Magn. Reson. 2014;16:W6. doi: 10.1186/1532-429X-16-S1-W6.

107. Saybasili H, Herzka DA, Seiberlich N, Griswold MA. Real-time imaging with radial GRAPPA: Implementation on a heterogeneous architecture for low-latency reconstructions. Magn. Reson. Imaging 2014;32:747–58. doi: 10.1016/j.mri.2014.02.022.

108. Sayin O, Saybasili H, Zviman MM, Griswold M, Halperin H, Seiberlich N, Herzka DA. Real-Time Free-Breathing Cardiac Imaging with Self-Calibrated Through-Time Radial GRAPPA. 2017;77:250–264. doi: 10.1002/mrm.26112.

109. C. Koay, J. Sarlls EÃ. Three-dimensional analytical magnetic resonance imaging phantom in the Fourier domain. Magn. Reson. Med. 2007;58:430–436.

110. Guerquin-Kern M, Lejeune L, Pruessmann KP UM. Realistic analytical phantoms for parallel magnetic resonance imaging. IEEE Trans Med Imaging 2012;31:626–36.

111. T. M. Ngo , G. S. K. Fung , S. Han , M. Chen , J. L. Prince , B. M. W. Tsui , E. R. McVeigh DAH. Realistic analytical polyhedral MRI phantoms. Magn. Reson. Med. 2016;76:663–678.

112. Wissmann L, Santelli C, Segars WP KS. MRXCAT: realistic numerical phantoms for cardiovascular magnetic resonance. J Cardiovasc Magn Reson 2014;16:63.

113. Tobon-Gomez C, Sukno FM, Bijnens BH, Huguet M FA. Realistic simulation of cardiac magnetic resonance studies modeling anatomical variability, trabeculae, and papillary muscles. Magn Reson Med. 2011;65:280–8.

114. Cook. RRP and RD. Cross-validation of regression models. J. Am. Stat. Assoc. 1984;79(387):575--583.

115. Kohavi R. A study of cross-validation and bootstrap for accuracy estimation and model

selection P. roc. 14th Int. Jt. Conf. Artif. Intell. 1995:338–345.

116. Shao J. Linear model selection by cross-validation. J. Amer. Stat. Assoc. 1993;88:486–494.

117. Arlot S CA. A survey of cross-validation procedures for model selection. Stat. Surv. 2010;4:40–79.

118. Akaike H. A New Look at the Statistical Model Identification I. EEE Trans. Autom. Control 1974;19:716–723.

119. H. A. Likelihood of a model and information criteria. J. Econom. 1981;16:3–14.

120. Draper NR, Smith H. Applied Regression Analysis. Wiley-Interscience.; 1998.

121. Glantz SA, Slinker BK. Primer of Applied Regression and Analysis of Variance. McGraw-Hill.; 1990.

122. Fulop S, K F. Algorithms for computing the time-corrected instantaneous frequency (reassigned) spectrogram, with applications. J. Acoust. Soc. Am. 2006;119:360–371.

123. F A, P F. Improving the Readability of Time-Frequency and Time-Scale Representations by the Reassignment Method. IEEE Trans. Signal Process. 1995;43:1068–1089.

124. Sayin O, Saybasili H, Guo L, Carrino JA, Sheehan FT, Griswold M, Seiberlich N, Herzka DA. Flexible real-time imaging of highly-dynamic knee joint motion. In: Proc. Intl. Soc. Mag. Reson. Med. 21. 2013.

125. Bellenger NG, Grothues F, Smith GC, Pennell DJ. Quantification of right and left ventricular function by cardiovascular magnetic resonance. Herz 2000;25:392–9.

126. Keenan NG, Pennell DJ. CMR of ventricular function. Echocardiography 2007;24:185–93. doi: 10.1111/j.1540-8175.2007.00375.x.

127. Grover S, Leong DP, Selvanayagam JB. Evaluation of left ventricular function using cardiac magnetic resonance imaging. J. Nucl. Cardiol. 2011;18:351–65. doi: 10.1007/s12350-010-9334-z.

128. Steel KE, Kwong RY. Application of cardiac magnetic resonance imaging in cardiomyopathy. Curr. Heart Fail. Rep. 2008;5:128–35.

129. Bohl S, Schulz-Menger J. Cardiovascular magnetic resonance imaging of non-ischaemic

heart disease: established and emerging applications. Heart. Lung Circ. 2010;19:117–32. doi: 10.1016/j.hlc.2009.11.005.

130. Aljaroudi W a, Flamm SD, Saliba W, Wilkoff BL, Kwon D. Role of CMR imaging in risk stratification for sudden cardiac death. JACC. Cardiovasc. Imaging 2013;6:392–406. doi: 10.1016/j.jcmg.2012.11.011.

131. Hoey ETD, Elassaly M, Ganeshan A, Watkin RW, Simpson H. The role of magnetic resonance imaging in hypertrophic cardiomyopathy. Quant. Imaging Med. Surg. 2014;4:397–406. doi: 10.3978/j.issn.2223-4292.2014.09.04.

132. Moghari MH, Komarlu R, Annese D, Geva T, Powell AJ. Free-breathing steady-state free precession cine cardiac magnetic resonance with respiratory navigator gating. Magn. Reson. Med. 2015;73:1555–1561. doi: 10.1002/mrm.25275.

133. Usman M, Atkinson D, Kolbitsch C, Schaeffter T, Prieto C. Manifold learning based ECG-free free-breathing cardiac CINE MRI. J. Magn. Reson. Imaging 2014;0:1–7. doi: 10.1002/jmri.24731.

134. Zhang S, Joseph A a, Voit D, Schaetz S, Merboldt K-D, Unterberg-Buchwald C, Hennemuth A, Lotz J, Frahm J. Real-time magnetic resonance imaging of cardiac function and flow-recent progress. Quant. Imaging Med. Surg. 2014;4:313–29. doi: 10.3978/j.issn.2223-4292.2014.06.03.

135. Wiesinger F, Boesiger P, Pruessmann KP. Electrodynamics and ultimate SNR in parallel MR imaging. Magn. Reson. Med. 2004;52:376–90. doi: 10.1002/mrm.20183.

136. Tsao J, Kozerke S, Boesiger P, Pruessmann KP. Optimizing spatiotemporal sampling for k-t BLAST and k-t SENSE: application to high-resolution real-time cardiac steady-state free precession. Magn. Reson. Med. 2005;53:1372–82. doi: 10.1002/mrm.20483.

137. Kannengießer SAR, Brenner AR, Noll TG. Accelerated Image Reconstruction for Sensitivity Encoded Imaging with Arbitrary k-Space Trajectories. Proc. Intl. Soc. Mag. Reson. Med. 8 2000.

138. Seiberlich N, Breuer F, Heidemann R, Blaimer M, Griswold M, Jakob P. Reconstruction of

undersampled non-Cartesian data sets using pseudo-Cartesian GRAPPA in conjunction with GROG. Magn. Reson. Med. 2008;59:1127–37. doi: 10.1002/mrm.21602.

139. Griswold MA, Jakob PM, Nittka M, Goldfarb JW, Haase A. Partially Parallel Imaging With Localized Sensitivities (PILS). Magn. Reson. Med. 2000;44:602–609.

140. Yeh EN, McKenzie C a, Ohliger M a, Sodickson DK. Parallel magnetic resonance imaging with adaptive radius in k-space (PARS): constrained image reconstruction using k-space locality in radiofrequency coil encoded data. Magn. Reson. Med. 2005;53:1383–92. doi: 10.1002/mrm.20490.

141. Samsonov A a, Block WF, Arunachalam A, Field AS. Advances in locally constrained k-space-based parallel MRI. Magn. Reson. Med. 2006;55:431–8. doi: 10.1002/mrm.20757.

142. Liu C, Bammer R, Moseley ME. Parallel imaging reconstruction for arbitrary trajectories using k-space sparse matrices (kSPA). Magn. Reson. Med. 2007;58:1171–81. doi: 10.1002/mrm.21334.

143. Saybasili H, Herzka DA, Seiberlich N, Griswold M. Low-Latency Radial GRAPPA Reconstruction using Multi-Core CPUs and General Purpose GPU Programming. Proc. Intl. Soc. Mag. Reson. Med. 20 2012;20:2554.

144. Arunachalam A, Samsonov A, Block WF. Self-calibrated GRAPPA method for 2D and 3D radial data. Magn. Reson. Med. 2007;57:931–8. doi: 10.1002/mrm.21223.

145. Huang F, Vijayakumar S, Li Y, Hertel S, Reza S, Duensing GR. Self-calibration method for radial GRAPPA/k-t GRAPPA. Magn. Reson. Med. 2007;57:1075–85. doi: 10.1002/mrm.21233.

146. Codella NCF, Spincemaille P, Prince M, Wang Y. A radial self-calibrated (RASCAL) generalized autocalibrating partially parallel acquisition (GRAPPA) method using weight interpolation. NMR Biomed. 2011;24:844–54. doi: 10.1002/nbm.1630.

147. Hamilton JI, Wright KL, Griswold MA, Seiberlich N. Self-Calibrating Interleaved Reconstruction for Through-Time Non-Cartesian GRAPPA. Proc. Intl. Soc. Mag. Reson. Med. 21 2013:3836.

148. Fessler J. Image reconstruction toolbox. https://web.eecs.umich.edu/~fessler/code/

149. Wright KL, Chen Y, Saybasili H, Griswold MA, Seiberlich N, Gulani V. Quantitative High-Resolution Renal Perfusion Imaging Using. Invest. Radiol. 2014;49.

150. Lustig M, Alley M, Vasanawala S, Donoho DL, Pauly JM. L1 SPIR-iT : Autocalibrating Parallel Imaging Compressed Sensing. Proc. Intl. Soc. Mag. Reson. Med. 17 2009:334.

151. Feng L, Axel L, Chandarana H, Block KT, Sodickson DK OR. XD-GRASP: golden-angle radial MRI with reconstruction of extra motion-state dimensions using compressed sensing. Magn Reson Med 2016;75:775–788.

152. Segars WP TB. MCAT to XCAT: The evolution of 4-D computerized phantoms for imaging research. Proceed IEEE. 2009;97:1954–68.

153. Segars WP, Sturgeon G, Mendonca S, Grimes J TB. 4D XCAT phantom for multimodality imaging research. Med Phys. 2010;37:4902–15.

154. Hansen MS. ISMRM Sunrise Recon Course. 2013. https://github.com/hansenms/ismrm_sunrise_matlab

CURRICULUM VITAE

Ozan Sayin **November 2017**

Birth: Aug 31st 1986, Ankara, Turkey

Education History

Ph.D. Expected	2017	Biomedical Engineering	Johns Hopkins School of Medicine
B.Sc.	2008	Electrical and Electronics Engineering	Bilkent University

Professional Experiences

Senior Data Scientist	2015-present	ZestFinance Inc. (Los Angeles, CA)
Fellow	2015	Insight Data Science (New York, NY)

Journal Publications

O. Sayin, H. Saybasili, M. M. Zviman, M. Griswold, H. Halperin, N. Seiberlich, D. A. Herzka, "Real-time free-breathing cardiac imaging with self-calibrated through-time radial GRAPPA", Magnetic Resonance in Medicine, 2017; 77: 250–264.

Conference Proceedings

O. Sayin, H. Saybasili, M. M. Zviman, M. Griswold, N. Seiberlich, D. A. Herzka "A Self-Calibrated Through-time radial GRAPPA Method", Proceedings of the 23rd Meeting of the International Society for Magnetic Resonance in Medicine, 2015.

O. Sayin, H. Saybasili, H. Halperin, M. M. Zviman, M. Griswold, N. Seiberlich, D. A. Herzka, "Accelerated Delayed Enhancement Imaging with Through-Time Radial GRAPPA", Proceedings of the 22nd Meeting of the International Society for Magnetic Resonance in Medicine, 2014.

O. Sayin, H. Saybasili, M. Griswold, N. Seiberlich, D. A. Herzka, "Calibration Reduction for Through-time radial GRAPPA by Weights Compression", Proceedings of the 22nd Meeting of the International Society for Magnetic Resonance in Medicine, 2014.

O. Sayin, H. Saybasili, H. Halperin, M. M. Zviman, M. Griswold, N. Seiberlich, D. A. Herzka, "Accelerated Delayed Enhancement Imaging of Myocardial Infarction with Through-time Radial GRAPPA", Journal of Cardiovascular Magnetic Resonance 2012, **16**(Suppl 1):W6 (Oral Presentation).

O. Sayin, H. Saybasili, L. Guo, J. A. Carrino, F. T. Sheehan, M. Griswold, N. Seiberlich, D. A. Herzka**,** "Flexible real-time imaging of highly-dynamic knee joint motion", Proceedings of the 21st Meeting of the International Society for Magnetic Resonance in Medicine, 2013.

O. Sayin, J. A. Derbyshire, L. Guo and D. Herzka, “Eddy-current-induced Artifact Suppression for b-SSFP via Through-slice Dephasing”, Proceedings of the 20th Meeting of the International Society for Magnetic Resonance in Medicine, 2012.

O. Sayin, J. A. Derbyshire, E. McVeigh and D. Herzka, “Through-slice Dephasing for Eddy Current Artifact Reduction in bSSFP”, Journal of Cardiovascular Magnetic Resonance 2012, **14**(Suppl 1):P271.

D. Xu, C. R. Weiss, **O. Sayin,** W. D. Gilson, J. S. Lewin, E. R. McVeigh, D. A. Herzka, “T2-Weighted Fat Suppressed Balanced SSFP Imaging (Contrast-Prepared SSFP) for Interventional Guidance”, Proceedings of the 21st Meeting of the International Society for Magnetic Resonance in Medicine, 2013.

L. Guo, **O. Sayin**, J. A. Derbyshire, D. A. Herzka, “Navigator-Free Self-Gated Dynamic Cine Imaging Using 2D Cartesian Golden Step Phase Encoding”, Proceedings of the 20th Meeting of the International Society for Magnetic Resonance in Medicine, 2012.

D. Xu, P. DiCamillo, **O. Sayin**, A. J. Flammang, W. D. Gilson, E. R. McVeigh, J. S. Lewin, C. R. Weiss, D. A. Herzka, “MR-Guided Sclerotherapy: Intra-procedural Visualization Vascular Malformations using Contrast-Prepared SSFP”, Proceedings of the 9th Interventional MRI Symposium, 2012.

J. A. Derbyshire, H. Saybasili, L. Guo, **O. Sayin**, P. Kellman, R. J. Lederman, and D. A. Herzka, “Golden Step Phase Encoding: Simultaneous real-time and ECG gated-Cine Parallel MRI with Retrospective Selection of Temporal Resolution, Acceleration Rate and Acquisition Duration”, Proceedings of the 19th Meeting of the International Society for Magnetic Resonance in Medicine, 2011.

H. Saybasili, J. A. Derbyshire, L. Guo, **O. Sayin**, A. M. Stine, R. J. Lederman, and D. A. Herzka, “Fully Auto-Calibrated Golden-Step Cartesian MRI”, Proceedings of the 19th Meeting of the International Society for Magnetic Resonance in Medicine, 2011.

J. A. Derbyshire, H. Saybasili, L. Guo, **O. Sayin**, P. Kellman, R. J. Lederman, and D. A. Herzka, “Golden-Step Phase Encoding for Flexible Real-time Cardiac MRI”, Journal of Cardiovascular Magnetic Resonance 2011, 13(Suppl 1):P23.

Awards and Achievements

2015	ISMRM Magna Cum Laude Award
2012-2014	ISMRM Travel Award
2008	Graduated Summa Cum Laude (1/450) from Bilkent University

Extracurricular Activities

2013-2014	Performer in the JHU Graduate Student Dance Club
2009-2011	Captain of the JHU-BME Soccer Team *Homewood Lions*